Modelling of Long Period Gratings in PCFs Inscribed by an Electric Arc and Gratings in SMF Inscribed by Femtosecond Laser Pulses

JOVANA PETROVIĆ

Doctor of Philosophy

ASTON UNIVERSITY

July 2006

Abstract

It was shown recently that long period gratings (LPGs) inscribed in photonic crystal fibres (PCFs) by an electric arc can solve the common problems of the LPGs inscribed by UV in standard fibres: the cross-sensitivity and the deterioration with temperature. The LPGs in PCFs were reported to be insensitive to temperature while sensitive to strain, bending and the refractive index. Another series of promising LPGs are LPGs inscribed by femtosecond laser in standard single mode fibre (SMF). They can be inscribed through the fibre coating and, due to the well confined index change and the lack of a need for dopants, they can be positioned anywhere in the fibre. However, the further exploitation of either grating is not possible without understanding their operation and the mechanisms of fabrication which was not supplied by the previous experimental study.

The work presented here is a detailed study of LPGs in PCFs and the femtosecond inscription that should enable modelling of the index profile of the grating induced by this method.

The model of LPGs in PCFs presented is capable of a comprehensive characterisation of the LPG from the operation principle to the sensitivity. Based on this model a method for the nondestructive index profiling of the LPG that uses the grating growth is proposed which is general and can be applied to any LPG written in the bulk of a fibre.

Fibre gratings inscribed by femtosecond laser pulses in SMFs are modelled based on the previous experimental and theoretical study of the femtosecond inscription. The results of this study comprise the characterisation of the refractive index change versus pulse energy, determination of the inscription thresholds, proof of the durability of the index change, and the numerical calculation of the distribution of the electron plasma left in the material after the pulse. The theoretical results compare well to the experiments with fused silica and predict the possibility of the inscription of subwavelength index changes in the Kerr media. The experimental and theoretical results were used to propose an index profile for fibre gratings inscribed by a femtosecond laser that can explain their unusually high birefringence.

To
the band "Umetnost je vazna"
and my parents

Acknowledgements

I unhesitatingly dedicate this thesis to my parents Mirjana and Srdjan, and my brother Mihailo because they keep receiving the best and the worst parts of me as if there were no difference between them.

My gratitude and love for those who were supportive always and always at the right time are enormous: Liz Hore, Irina Nasieva, Selena Teeling and Marko Simonović.

My appreciation and respect belong to Ian Bennion.

Friendly and professional thanks to Ljupco Hadzievski and Sergei Turitsyn for enabling me to come to Aston and being supportive along the way. Starting the experimental work was a new and not an easy task. The help from Igor Khrushchev, Misha Dubov and Amós Martinez was precious, indeed. I appreciated the collaboration with Dave Webb, Helen Dobb and Thomas Allsop for both their efficiency and curiosity. I am glad I had the pleasure to contribute to and be inspired by the work and personality of Sasha Grigorenko.

Special acknowledgement for discussions on everything and anything is reserved for Tom, Supun, Amós, Sonia, Sonja, Rachel, Zahariah and Alleyn.

I would like to specially thank a great thinker and a perfectly sensible human being – my supervisor Vladimir Mezentsev for the all he did for me and how.

At the end, I would like to mention some great people who had left an immeasurable impact on me: Dusan Jovanović, Ivan Zornić and Vitomir Milanović who taught me to understand physics and my grandparents Vera and Zivojin Blagojević who taught me to understand life.

Contents

List of Figures

List of Tables

Chapter 1

Introduction

1.1 Structure of the Thesis

The main topic of this thesis is modelling of state-of-the-art fibre gratings but it also includes the physics of these devices, their fabrication and the applications. As it was experimentally demonstrated that the gratings fabricated in the novel fibres such as photonic crystal fibres and by novel techniques such as femtosecond inscription have advantageous properties uncommon for other gratings, the need for better understanding of these gratings and the mechanisms of the fabrication has emerged. We established the models that can describe the principles of the grating operation and their applications in sensing. These models can also be used as tools for the index profiling of the grating and thereby investigation of the fabrication mechanisms which is crucial for their design and future applications.

The thesis was written with the intention to offer the thorough explanation of the physical principles behind the behaviour and fabrication of these novel gratings and to describe the numerical models that quantify them. The presentation of the general knowledge of each subject has been minimised to the level sufficient for grasping the treated problem but referenced abundantly so that more information can be easily found, whereas the original approaches, results, and the ideas are described in detail. In order to enable reading at different levels, each topic is divided into three layers: experimental evidence and prospective applications, physical explanation and numerical modelling.

The thesis comprises four chapters. In order to offer some understanding to the re-

searchers from the related fields, the current chapter gives a rather general review of the field, poses the problems treated in the latter sessions and explains the known methods used throughout the thesis. Chapter 2 presents a comprehensive study of the long period gratings in the photonic crystal fibres inscribed by the electric-arc. Chapter 3 is the widest in scope for it swipes the emerging field of the femtosecond inscription from the basic experiments and physical understanding to the elaborate numerical modelling and the fabrication of the devices with strict requirements. The last chapter is more application oriented as it proposes a model of the fibre gratings fabricated by the femtosecond laser and its applications in the design of highly birefringent gratings and study of the induced refractive index change.

1.2 Long Period Gratings

Gratings in general are periodic devices used to control the propagation of light and matter. Gratings with periods ranging from hundreds of nanometers to several hundreds of microns are used for the manipulation of light by constructive and destructive interference. When fabricated in an optical fibre they control the properties of light guided or radiated through the fibre. Since they are embedded into the waveguide, the behaviour of the fibre gratings is not determined only by their period but also by the properties of the fibre itself and the environmental conditions that influence the guidance of light through it. The former is associated with their application as filters, dispersion compensators, reflectors, etc. and the later with the sensing applications.

Fibre gratings consist of periodic changes in the refractive index or the geometry of a fibre which are usually small and can be treated as a perturbation. The principle of the grating operation is coupling between the fibre modes. Based upon the period they are generally classified into two groups: fibre Bragg gratings (FBGs) and long period gratings (LPGs). The period of an FBG is of the order of submicron and the coupling they cause is contrapropagational. LPGs have periods of several tens or, more usually, hundreds of microns and couple the guided modes to the copropagational modes.

Fabrication of the first FBG formed by the standing-wave interference pattern set-up was reported by Hill et al. [1]. Since then they have been fabricated by different methods: holo-

graphic, phase mask, point-by-point, amplitude mask, and in fibres of different composition and geometry. Coupling of the core mode to the backward propagating core mode causes a narrow peak in the reflection spectrum or equivalently, an attenuation band in the transmission spectrum. Hence its usage as a narrow band reflector or a narrow-band channel-dropping filter. Other applications are in dispersion compensation, chirped pulse amplification and sensing [2]. FBGs were the precursors of LPGs and many ideas considering fabrication and applications had been already well known at the time the first LPGs appeared. However, the LPGs appeared exactly as a solution for the low-reflection band-rejection filters, not achievable by the FBGs.

In the pursuit of such filters, needed for gain-equalisation in erbium doped fibre amplifiers, Vengsarkar et al. fabricated the first long period fibre gratings using both UV [3] and CO_2 [4] lasers. They coupled the core mode to the guided and radiation cladding modes that attenuate in the coated part of the fibre, forming a series of attenuation bands in the transmission spectrum. Examples of the grating and the spectrum are shown in Fig. 1.1. As different attenuation bands exhibit different responses to the range of external parameters, LPGs were recognised as a promising tool for advanced applications in sensing, e.g. simultaneous sensing of different parameters, temperature compensation schemes, enhanced sensitivity due to the splitting of the attenuation bands. This has increased interest in LPGs and resulted in numerous successful attempts to fabricate them in special or new kinds of fibres, W-shaped, progressive three layered (PTL), D-shaped, dispersion compensation (DCF), silica and polymer photonic crystal fibres. The new laser technology enabled new techniques of fabrication, the most recent and popular of which is the femtosecond micromachining. As a result of these trends, the work presented here is about the LPGs fabricated in PCFs by the electric arc and the LPGs inscribed in the SMF by the femtosecond laser, whereby the attention is paid on the methods of fabrication, novel properties and the sensing applications of these gratings.

Here, the general review of the fabrication methods and applications of LPGs is presented in the context of which the motivation for and relevance of our work is defined. The accent is on femtosecond inscription and sensing applications as the topics most relevant for this thesis. Since most of the work done is based on the results from the grating modelling, the last section is dedicated to the numerical treatment of the gratings, PCFs and femtosec-

Figure 1.1: Long period gratings inscribed in: a) the core and b) the cladding of the step-index fibre, and c) PCF (holey fibre). d) Typical spectrum of LPG (http://www.cranfield.ac.uk/soe/cpoe/cpoebrag3.htm).

ond inscription.

1.3 Fabrication of LPGs

The majority of LPGs are formed by periodically changing the refractive index of the fibre core. This is achieved by irradiation by different lasers: ultraviolet (UV), femtosecond pulsed laser in near infra red (NIR) or CO_2 lasers or by other techniques such as the diffusion of dopants into the core, the relaxation of mechanical stress and the application of an electric arc. LPGs can also be made by changing the fibre cladding by tapering, chemical etching, or the application of mechanical stress.

The most frequently used method is the fabrication by UV laser by set-ups similar to those applied in the fabrication of FBGs. There are several drawbacks of this technique: the fibre core must be photosensitive, the index change is asymmetric and causes birefringence, the index change decays in time and with the increase in temperature. The last can be controlled by the hydrogenation of the fibre before inscription to enhance the photosensitivity or by postprocessing by etching. Both methods limit the possibilities of the design of the gratings with precise characteristics. Changes in refractive index introduced by the UV laser are classified in two types. Gratings that are thermally annealed belong to the type-I and those

that are not annealed even at temperatures as high as 900°C belong to the type-II. Colour centres are responsible for the type-I change and the permanent damage of material for the type-II change [5].

The requirement for the doped core can be overcome by the use of a CO_2 laser, femtosecond laser, or electric arc. However, none of these techniques has been known in so much detail as UV inscription and the physical processes responsible for the index change are yet to be fully understood. The deformation of the fibre cladding by chemical etching or corrugation is a universal technique for grating fabrication in almost any fibre.

Since the mechanism of light guidance in photonic crystal fibres does not require a doped core, the gratings in these fibres are usually inscribed by one of the techniques from the last paragraph, [6–8], with the exception of the LPGs in purposely doped PCFs [9]. The refractive index change in the photo-insensitive PCFs comes from the change in the refractive index of silica and the geometry of the fibre, i.e. reduction in the diameter of the holes or tapering of the outer cladding, therefore the index change being necessarily confined to the core. As these devices are relatively new, neither of the fabrication methods has been recognised as preferable.

The work presented in this thesis concentrates on LPGs produced by electric arc in endlessly single mode PCFs and is highly motivated by the experimental results of my colleagues H. Dobb, D.J. Webb and K. Kalli. They have reported that the gratings fabricated by this cheap and readily accessible technique are insensitive to temperature [10], which is in itself an excellent motive for further studies of these gratings as it solves the problem of the cross-sensitivity. It was also shown that a powerful electric arc can produce a grating with only two periods (unpublished results of H. Dobb). The major drawback of this technique is the asymmetry inherently induced by application of the electrodes onto two sides of the fibre. Another limitation is that the minimum grating period is around 100μm. Several studies of the impact of the electric arc on the fibre have been conducted in both step index fibres [11], [12], and PCFs [13], but the complete characterization does not exist yet. Here, we use the known properties of the grating: (*i*) the final spectrum and the spectra recorded during the grating growth, (*ii*) grating sensitivity to the refractive index and (*iii*) the properties of the PCF in which it is inscribed, to retrieve the changes in the index profile induced by the electric arc. We also propose a model that is capable of explaining and quantifying the sensitivity

of the grating to the external parameters.

In-bulk gratings can be fabricated in any kind of fibre by irradiation by NIR femtosecond pulses [14, 15]. Moreover, the point-by-point technique enables precise changes of the refractive index anywhere in the fibre. Since the femtosecond inscription relies on the tight focusing of the pulse, its application to the PCF is limited to the cladding because of the diffraction on the holes. On the other hand, in the 'continuous' fibres tightly focused femtosecond pulses can induce well confined index changes the composition of which can result in a variety of index profiles. An obvious disadvantage of the femtosecond inscription is the cost of the set-up. However, due to the advances in performance and robustness of solid state lasers over the last several years, it has been greatly reduced, bringing the femtosecond system to many optical tables around the world. In the course of our work both the femtosecond technique and the LPGs inscribed by it were studied in detail.

1.4 Applications of LPGs

The intrinsic characteristic of long period gratings is that they attenuate the part of the spectrum around the resonant wavelength. This property has been exploited in amplifier gain equalization. The advantage of this solution over other gain equalizers, e.g. side tapped gratings, is a very low back reflection. On the other hand, the sensitivity of the LPG to temperature and refractive index can deteriorate the performance of the equalizer. These problems are resolved by using special temperature-stabilized fibres and by polymer coating, respectively.

The sensitivity of the resonant wavelength to temperature, strain, bending and the external refractive index can be used in its own right for fabrication of stable sensors effectively independent of fluctuating light levels, source power and connector losses. The change in magnitude of the attenuation bands is deprived of these advantages, but was used to broaden the scope of applications of LPGs, e.g. sensing external refractive indices higher than the index of cladding or differential sensing configurations such as the liquid level sensor reported in [16].

The fact that the cladding modes resonant at different wavelengths have different mode

profiles and therefore different sensitivities to the same external parameter was used for the simultaneous sensing of different parameters, for instance strain and temperature [17], [18]. Another way to make a two-parameter sensor is based on the splitting of the attenuation band due to the asymmetry induced by the measurand. In [19] the sensitivity of the wavelength shift to temperature and the splitting of the same attenuation band due to bending were used to sense these parameters simultaneously. However, sensitivity of the attenuation band to several parameters simultaneously is not always accompanied by the additional information such as splitting of the attenuation bands and does not allow for distinguishing the effects of different parameters. This phenomenon is called cross-sensitivity and is undesirable in the applications that require sensing of one parameter only. The most frequently present unwanted effect is change in temperature. It has been solved in different ways: using short grating periods ($< 100\mu$m), packaging that reduces sensitivity to temperature [20, 21], cascaded LPGs [22]. The unique feature of LPGs fabricated in PCFs by an electric arc [10, 23] is that they are almost insensitive to temperature while sensitive to strain, bending and refractive index, thus eliminating the need for compensation schemes. The possibility of the straightforward use of these LPGs in sensors urged the need for further studies and motivated the comprehensive analysis of their operation, refractive index profile and applications in sensing presented in Chapter 2.

The sensitivity to external parameters, which directly influence the properties of the grating, has been used to sense other parameters indirectly. The possibilities offered by the sensitivity to the refractive index have been particularly versatile as it was used in sensing of the liquid-level [16], concentration of solutions [24], flow of resin [25], etc. The small size and light weight of the fibre sensors have made them attractive for biomedical applications. The general trend over the last few years has been into this direction and hence the range of chemically sensitive devices [26, 27] most of which describe LPGs with chemically active overlays.

For further reference the author heartily recommends an excellent review of the characteristics and applications of the optical fibre long period grating sensors by S. W. James and R. P. Tatam [28].

Due to their well defined spectral behaviour, gratings can be used to study other phenomena. This was the case in [29] where an LPG was temporarily induced in PCF to explore

the possibilities of acousto-optical coupling. Here, the idea is pushed further as the spectral properties of LPGs were used to study the physical processes involved in the fabrication of the gratings, in particular the interaction of the femtosecond pulse with silica. Index profiling of the LPGs inscribed under systematically changed conditions addresses the main problem in the exploitation of femtosecond micromachining which is the lack of knowledge of the processes that lead to the refractive index change. This study would not be possible without the collaborative environment in the Photonics Research Group in which theory meets applications.

1.5 Modelling of Fibre Gratings

The propagation of light through a waveguide is described by Maxwell's equations. In circularly symmetric fibres these equations have analytical solutions and the modes are described by the spherical Bessel functions. However, for fibres with more complicated geometries numerical solution is necessary. Once the modes of the fibre are known, fibre gratings can be modelled by different methods: coupled-mode theory, Rouard's methods, transfer matrix method (TMM), Bloch waves, variational and Hamiltonian methods, etc. The most commonly used methods are coupled mode theory, transfer matrix and Rouard's method. Coupled mode theory is essentially perturbation theory and it is an elegant solution for the uniform grating. If the index modulation in the grating is slow along the fibre, it can be divided into sections with a uniform index change. The coupled-mode theory gives the transfer matrix for each section and the product of all the matrices gives the transfer function of the grating. This is known as the transfer matrix method (TMM) and has become very popular due to the simplicity and the low computational cost. There are no intrinsic limitations other than those of the coupled-mode theory, but the optimal number and placement of sections must be chosen in order to get an accurate solution. Another method based on the division of the grating into sections is Rouard's method in which the reflection and the transmission of the layer are obtained from the equations for the Fresnel reflection and refraction. The grating must be divided into sections small enough that the index change can be considered constant, which often implies subdivision of the grating period. Unlike coupled-mode the-

ory and TMM, Rouard's method cannot be applied to the gratings with a nonuniform index change across the fibre unless substantial approximations are made. As the last is the case in the LPGs inscribed in the PCFs by an electric arc and the LPGs inscribed by a femtosecond laser both of which were also nearly uniform, the method of choice was coupled-mode theory. It is reviewed in the next section.

1.5.1 Coupled-mode theory

In electromagnetic waveguides homogeneous in the direction of propagation the electromagnetic wave propagating along the waveguide is nearly a plane wave with the characteristic transverse field distribution that depends on the index profile of the waveguide. In other words, the longitudinal field components are much smaller than the transverse [30]. As a consequence, the solution of the wave equation derived from Maxwell's equations [31] is separable and can be represented in the form

$$E(\vec{r}) = E(x,y)A(z)e^{-i\beta z} \tag{1.1}$$

for the electric field and analogously for the magnetic field. z is the direction of propagation, β is the propagation constant and $A(z)$ is the slowly varying field amplitude. Normalisation adopted here is such that each mode carries the power of $1W$. The envelope of the field amplitude $A(z)$ describes a modulation caused by perturbation in the index profile along the fibre. If the perturbation is periodic, the input mode can fall into resonance with the particular cladding mode. The transfer of energy between these two modes is known as mode coupling. The conservation of energy requires that the wavelengths of the coupled modes are equal. The conservation of momentum requires that the sum of the propagation vector of the input mode, $\vec{\beta}_1$, and the equivalent of the propagation vector of the grating, $\vec{k}_{pert}$, equals the propagation vector of the coupled mode $\vec{\beta}_2$. The latter is the well known phase matching condition given by the equation

$$\vec{\beta}_1 + \vec{k}_{pert} = \vec{\beta}_2$$

When the light comes upon the grating it experiences Bragg scattering. Hence, the vector $\vec{k}_{pert}$ has the direction opposite to $\vec{\beta}_1$ and magnitude $\frac{2\pi}{\Lambda}$ where Λ is the grating period.

Depending on the grating period two scenarios are possible: co- and contrapropagational coupling as is illustrated in Fig. 1.2. Since the difference between the propagation vectors of the contrapropagational modes is substantial, coupling can be caused only by the perturbation of the period small compared to the wavelength. Such a perturbation is called a fibre Bragg grating (FBG). On the other hand, coupling between the copropagational modes can occur only if the grating period is much larger than the wavelength (at least several tens of microns), hence the name of this perturbation - long period grating (LPG).

The classical approach to the modelling of fibre gratings is the z-dependent perturbation

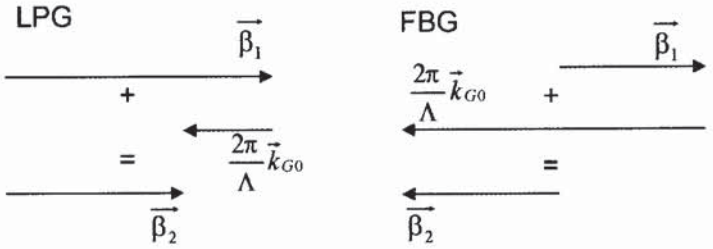

Figure 1.2: Phase matching.

theory known as the coupled-mode theory (CMT) [30, 32]. It is valid when the amplitude of the index change is small and particularly useful when the perturbation has a significant effect on the redistribution of modal power, as is the case in the fibre gratings [30].

According to the CMT any mode modified through coupling has a representation in the space the orthogonal basis vectors of which are the transverse eigenmodes $E(x,y)$ of the unperturbed fibre. Standard derivations of the coupled mode equation can be found in [5, 33] and is simply the application of the perturbation theory of the first order. As a result, copropagating coupling can be formally described by the following system of equations

$$\frac{dA_k(z)}{dz} = i\sum_j A_j(z)(K^t_{jk} + K^z_{jk})(z)e^{i(\beta_j - \beta_k)z} \tag{1.2}$$

where K^t_{jk} and K^z_{jk} are the transverse and the longitudinal coupling coefficients, respectively, and the summation goes over all modes that are coupled to the mode k. The transverse coupling coefficient is given by

$$K^t_{jk}(z) = \frac{\omega}{4}\iint \Delta\varepsilon(\vec{r})\vec{E}^t_j(\vec{r})\vec{E}^{t*}_k(\vec{r})d\vec{r} \tag{1.3}$$

and the longitudinal by an analogous expression. Since the longitudinal fields are much smaller than transverse, $K^z \sim |E^z|^2 \ll |E^t|^2 \sim K^t$ and K^z can be neglected. Assuming a simple grating with a sinusoidal index change along z

$$\Delta n(z) = \overline{\Delta n}(1 + s\cos(\frac{2\pi}{\Lambda}z)) \tag{1.4}$$

where $\overline{\Delta n}$ is the average (dc) index change, s the modulation depth, and Λ the grating period, then Eqn. (1.3) can be rewritten as

$$K^t_{jk}(z) = \kappa^t_{jk}(1 + s\cos(\frac{2\pi}{\Lambda}z)) \tag{1.5}$$

$$\kappa^t_{jk} = \frac{\omega\varepsilon_0 n}{4}\iint \overline{\Delta n(r)}\vec{E}^t_j(\vec{r})\vec{E}^t_k(\vec{r})d\vec{r} \tag{1.6}$$

In the case considered κ is independent of z, which does not hold for the gratings that cannot be approximated by a sine function. The name 'coupling constant' is, however, used as long as its variation along the fibre due to the variation in the average refractive index change $\overline{\Delta n(r,z)}$ is slow compared to the grating period. The solution of Eqn. (1.2) is not averaged out only if the spatial frequency of the grating is close or equal to the beat frequency between the coupled modes, i.e. the detuning parameter δ is close to or equals zero

$$\delta_{jk} = \frac{1}{2}(\beta_j - \beta_k - \frac{2\pi}{\Lambda}) \approx 0 \tag{1.7}$$

This equation is the scalar phase matching condition. A useful physical analogy can be a resonant system driven by an external force. As the core mode is the only mode guided by the unperturbed fibre, it plays the role of the driving force. In the grating it couples to the phase matched cladding modes that are attenuated in the unstripped part of the fibre behind the grating. If the thereby formed attenuation bands in the transmission spectrum are well separated and narrow, it can be assumed that the coupling was to a single cladding mode. Then the system of Eqns. (1.2) can be reduced to two coupled mode equations for each attenuation band

$$\frac{dA^{co}(z)}{dz} = i\kappa_{co}A^{co}(z) + i\frac{s}{2}\kappa A^{cl}(z)e^{-i2\delta z} \tag{1.8}$$

$$\frac{dA^{cl}(z)}{dz} = i\kappa_{cl}A^{cl}(z) + i\frac{s}{2}\kappa^* A^{co}(z)e^{i2\delta z} \tag{1.9}$$

where κ_{co}, κ_{cl}, κ are core to core, cladding to cladding and cladding to core coupling constants, respectively, $A^{co}(z)$ and $A^{cl}(z)$ slowly varying amplitudes of the core and cladding

modes, and the detuning parameter is given by $\delta = \frac{1}{2}(\beta_{co} - \beta_{cl} - \frac{2\pi}{\Lambda})$. The transmission spectrum is a spectrum of the core mode at the end of the grating and its power near the particular resonance is given by

$$T(z) = \frac{|A^{co}(z)|^2}{|A^{co}(0)|^2} = \cos^2(\sqrt{|\kappa|^2 + \zeta^2})z + \frac{\zeta^2}{\zeta^2 + |\kappa|^2}\sin^2(\sqrt{|\kappa|^2 + \zeta^2})z \tag{1.10}$$

where ζ is the general self-coupling coefficient defined as

$$\zeta = \delta + \frac{\kappa_{co-co} - \kappa_{cl-cl}}{2} \tag{1.11}$$

For LPGs inscribed in the core, as is most frequently the case in the step fibres, the index change in (1.6) equals zero in the cladding and the simplifications $\kappa_{cl} << \kappa_{co}$ and $\kappa << \kappa_{co}$ are justified. Due to the unknown impact of the electric arc on the PCFs, more complicated change in the index profile is considered here and the a priori assumptions are minimised.

1.5.2 Numerical Methods

A much greater challenge than the adaptation of the coupled mode theory, was to define the input to it, i.e. to find the modes of the fibres the transverse index profiles of which are either complicated (PCFs) or inherently asymmetric (LPGs inscribed by a femtosecond laser). As the availability of the analytic solutions of Maxwell's equations is limited to much simpler geometries, the eigenmodes were found numerically. Two commonly used methods for solving partial differential equations are the finite difference (FD) and the finite element (FE) method. The former is an approximation of the differential equation and the latter is an approximation of the solution. While the mayor advantage of FDM is easy implementation, FEM is superior in handling geometries and boundaries of any shape. As opposed to the FDM which is based on the rectangular mesh in its basic formulation, meshing in FEM is more flexible; for example, predominantly used in 2D problems is the triangular mesh which can adhere easily to almost any boundary. FEM is also suitable for a geometry that comprises features of different spatial scales such as the bulk cladding and the holes of PCF.

Numerical Modelling of the Grating Inscription

The index change induced by an electric arc in the PCF is not trivial as it is not localised to the core. It is assumed that the index change comprises the contributions from the change in the hole radius and the refractive index of silica over the whole cross section of the fibre and that it is symmetric in the first approximation. The mode profiles and hence the overlap integrals can be calculated based on the modes of the unperturbed PCF. The grating is then modelled by the CMT whereby the coupling coefficients were calculated based from the modelled index change and the overlap integrals.

On the contrary, one of the main advantages of the inscription by the femtosecond laser is very good confinement of the index change. This was used to fabricate birefringent gratings by displacing the index change from the centre of the core. Due to the asymmetry of the grating profile, the coupled-mode theory that uses the eigenmode basis of the unperturbed fibre is not the optimal choice. Indeed, representation of a mode of the perturbed fibre in this basis can be achieved only by superposition of more than one term in which case a single attenuation band would contain contributions of several eigenmodes which significantly complicates the grating analysis. A solution is to use a basis calculated for the fibre perturbed by the average index change along the grating. As the FEM enables calculation of this basis for the known index profile of the grating, the problem is redirected to the modelling of the changes in the refractive index of the fibre induced by the femtosecond laser. The physical and numerical model of the grating are described in detail in Sec. 4.2 and of the femtosecond inscription in Sec. 3.5.

Due to the high intensity of the applied femtosecond pulse, nonlinearity of the refractive index becomes significant. Refractive index increases proportionally to the pulse intensity, e.g. for the Gaussian pulses it grows most in the centre of the pulse. As the light concentrates in the media with higher refractive index, the corresponding growth in intensity induces further increase in the refractive index and the effect is self-amplified. Since more and more pulse energy concentrates in the centre of the pulse, the phenomenon is known as self-focusing. For pulse powers above the critical, self-focusing dominates diffraction and may result in the collapse of the pulse, which is halted by the optical breakdown of the material. During this process the diameter of the pulse changes from several millimeters to less then 1μm. Small focal spots can also be achieved by tight focusing of the pulse by

microscope objective. In order to obtain a satisfactory resolution in the radial dimension at different points along the propagation axis an extremely fine grid is needed. A solution to this problem is to apply the adaptive mesh refinement. The idea underlying this method is to reexamine the grid resolution after a certain number of steps and to refine it locally if it fails to satisfy the criterion appropriate for the used numerical scheme, the choice of which depends on the physical problem being solved. For the purpose of the simulations presented in Chap. 3 the adaptive mesh solver developed by R. Grauer [34] and J. Dreher was used.

x x x x x x

"That is the fact. And fact is the most obdurate thing in the world. But we are now interested in what follows, and not in this already accomplished fact."

The Master and Margarita, Mikhail Bulgakov

Chapter 2

Modelling of Long Period Gratings Fabricated in Photonic Crystal Fibres by an Electric Arc

2.1 Description of the Device

Since the idea of the photonic band gap structures was introduced [35] and it was realised that these materials would enable tremendous control over optical processes, many efforts have been made to fabricate three dimensional photonic crystals. However, this proved to be rather difficult and attention was redirected to two dimensional structures which resulted in a breakthrough in optical fibre technology – the fabrication of the photonic crystal fibre [36, 37].

According to the principle of operation, photonic crystal fibres are divided into the photonic band gap fibres and the 'holey' fibres. The former have the air core surrounded by the photonic crystal. A mode is guided by the core if its propagation vector falls into a band gap of the photonic crystal. The 'holey' fibres consist of the photonic crystal cladding and the core obtained by omitting the central hole. The photonic crystal acts as a material with the effective refractive index lower than the index of the core and the principle of guidance resembles the total internal reflection with the clear difference that the core-cladding interface does not exist, [36, 38]. We have studied the long period gratings inscribed in the holey fibres

and in this thesis the term 'PCF' refers to these fibres.

We begin with the description of the fibres used as hosts and continue with the description of the fabrication and the properties of LPGs inscribed in them by the electric arc.

2.1.1 PCFs With the Bulk Cladding

We have studied LPGs inscribed in endlessly single mode ESM-1550-01 PCF formerly supplied by Blaze Photonics and large mode area LMA-10 PCF supplied by Crystal Fibre [39]. We will refer to these fibres as the ESM PCF and the LMA PCF.

The ESM PCF was made from pure silica and had a core diameter of 12μm surrounded

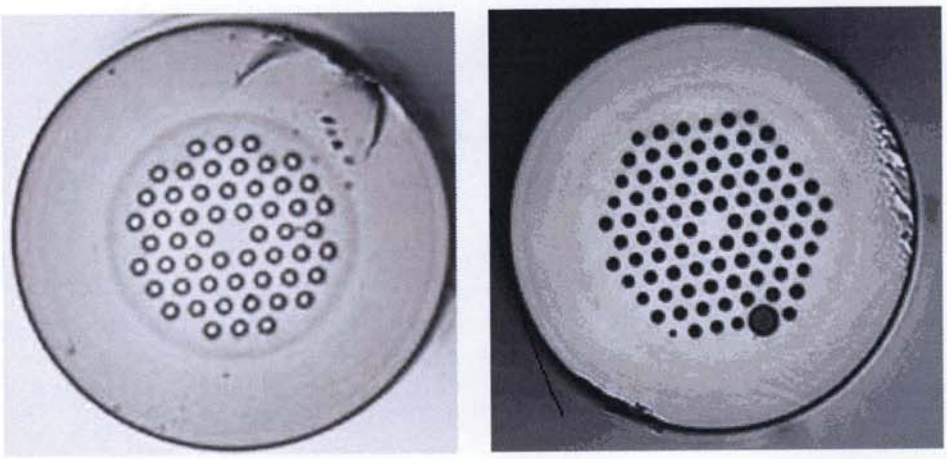

Figure 2.1: Cross section of a) ESM-1550-01 PCF and b) LMA-10 PCF.

by 54 hexagonally arranged air holes with the space between adjacent holes being 8μm. The filling factor was 0.46. A bulk silica cladding was separated from the core by the four rings of air holes, Fig. 2.1a.

The LMA PCF had a core diameter of 11μm and was surrounded by 89 hexagonally arranged air holes with a separation distance of 7.1μm and one outer hole missing. A silica cladding was separated from the core by the five rings of air holes. Using a microscope (Zeiss Axioskop), the hole radius was measured to be $2.0 \pm 0.1\mu$m. The regularity of the crystal was slightly ruined by two holes of radii 4.3μm and 0.9μm placed in the same outer row of the hexagon, Fig. 2.1b.

The geometry of these kind of fibres is generic and can be divided into three parts: pure

silica core, inner photonic crystal cladding and outer pure silica cladding. As the photonic crystal is made of a combination of air and silica, its effective refractive index is lower than the refractive index of the core and the light is confined to the core [36]. In theory, the geometry of the fibre can be designed so that the core mode is guided at any wavelength [40], but practically the absence of the core-cladding interface combined with the finite size of the photonic crystal prevents the total confinement of the guided light to the core.

2.1.2 LPGs Fabricated by an Electric Arc

Method

Electric arc is used for fabrication of LPGs in practically any kind of fibre, such as step-index fibre [41–43], or photonic crystal fibre [13], [12], [44]. It consists of the application of the arc between the electrodes of the fusion splicer [45] transverse to the fibre and the translation of the fibre for the grating period between each two discharges. The index change can be controlled by changing the duration and the power of the electric arc and can be positive [11] or negative [13, 42]. However, the direct measurements of the index change are scarce and are not helped by the fact that different kinds of fibre respond to the arc differently. In PCFs, the electric arc may cause a change in the refractive index, a reduction in hole size [13] and may taper the fibre. As the pictures of the cross section of the gratings analysed in this thesis were not available, those from the Ref. [13] are used for illustration in Fig. 2.2.

The change induced by the arc is asymmetric because of the position of the electrodes along one axis of the fibre cross section which is a major disadvantage of this method. Another is the uncertainty in the length of the fibre affected by the electric arc which makes the grating duty cycle difficult to control. However, the electric arc remains a technique of choice for many applications for the following reasons. As the only required equipment comprises a splicer and translation stage, the technique is neither costly nor complicated. The need for the photosensitive core is eliminated because the arc affects the pure silica as well as the geometry of the fibre. The gratings induced by the electric arc are stable at high temperatures [46].

The gratings studied here were imaged from the side by the phase microscope Zeiss

Figure 2.2: Cross section of the PCF a) before and b) after the application of the electric arc [13].

Figure 2.3: LPG in the ESM PCF viewed through the transmission phase microscope.

Axioskop. Figure 2.3 is representative of any point along the grating, i.e. no changes in the overall cross section such as tapering were observed. As the microscope used is a transmission microscope, the air holes prevented sharp focusing so that their size could not be measured. This would be possible only if the fibre were cleaved but, since the actual longitudinal profile of the grating is not known, the grating would have to be cleaved at many points in order to acquire enough information about the index change. As this is both time consuming and destructive, a method that enables index profiling from the readily available data would be a more efficient and elegant solution. Due to the complex change in the in-

dex profile induced by the arc, the restrictions imposed by the model must be kept minimal, making this method applicable to almost any long period grating inscribed in any fibre. As a part of the current work, the solution based on the experimentally recorded grating growth has been proposed [47] and will be presented in Sec. 2.3.

Spectral Properties of LPGs

The spectra of the LPGs with periods 500μm and 600μm in ESM PCF are shown in Fig. 2.4. An increase in the grating period causes a blue shift of the spectrum. The same was observed

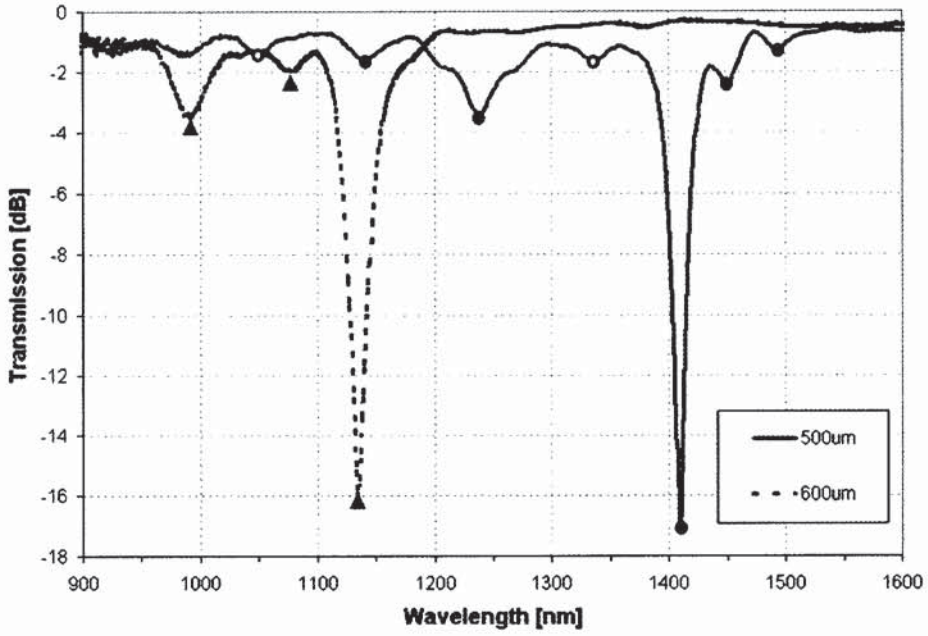

Figure 2.4: Spectra of the LPGs inscribed in the ESM PCF by the electric arc.

in LPGs in PCFs obtained by various methods: CO_2 laser [48], microdeformation [49], and acoustic waves [29]. In the wavelength range extending further into the near infra red both blue and red shift were observed in LPGs in step-index fibres [3, 28, 50], and the same was theoretically predicted for the LPGs in PCFs [51]. As the effective mode indices depend on the wavelength ($\delta n^{eff} = \delta n^{eff}(\lambda)$), The sign of the shift is determined by the waveguide dispersion of the fibre .

Sensitivity of LPGs Inscribed by Electric Arc

The LPGs studied here were sensitive to strain and bending and, unlike other LPGs in PCFs [9], also to the external refractive index. At the same time they were almost insensitive to temperature which is a great advantage in the systems where the cross-sensitivity is a problem. The actual values of the measured sensitivities are given in section 2.4 where they are compared with the results of simulations.

The asymmetry induced by the electric arc was not large enough to cause a directional sensitivity in the regular symmetric fibre such as ESM PCF. However, irregularities in the LMA PCF caused the birefringence of the cladding modes to be large enough to be exploited in a directional bending sensor, [23]. Since the irregularities in the LMA PCF used were a consequence of the fabrication method that has been largely improved and is now free of such shortcomings [52], this result should be understood as a demonstration of principle and an idea for the future design of directional sensors. We modelled both symmetric and asymmetric fibres and examined the impact of different irregularities on the sensing properties of LPGs.

2.2 Modal Analysis of PCFs

Due to the complex geometry of the PCF, Maxwell's equations must be solved numerically. Moreover, the sharp index contrast between the holes and the bulk of the fibre cannot be accurately modelled by a scalar approximation and the vectorial model is needed. A variety of numerical methods has been used: plane-wave expansion method [53], supercell lattice method [54], multipole method [55,56], Fourier decomposition method [57], beam propagation method (BPM), [58,59], finite difference method [60], finite element method [61,62]. For the purpose of the modelling presented here the full-vectorial Maxwell finite element solver bundled with the commercial package FEMLAB 3.0 [63] was used. It is based on the finite element method which offers fine and flexible meshing needed for the photonic crystal part of the fibre efficient enough to be performed on a personal computer (2.53GHz, 512MB RAM, the case here). The finite element method also offers the possibility to simulate any geometry without assumption of the infinite crystal as in [53]. This is crucial for

modelling of LPGs because it is not necessary to know only the core mode, as is the case in the majority of the applications, but the whole modal map of the fibre, in particular the cladding modes to which the core mode can couple. The sensitivity of the grating to the external refractive index has conditioned the choice of the solver in the same way.

The propagation constants and eigenmodes of the fibre were found as solutions of Maxwell's equations reduced to the wave equation for the magnetic field

$$\nabla \times (\frac{1}{\varepsilon} \nabla \times \vec{H}) - k_0^2 \vec{H} = 0 \tag{2.1}$$

where $\varepsilon(x,y)$ is the dielectric constant. In our model ε is constant on each subdomain and the subdomains are linked by the continuity boundary conditions $\vec{n} \times (\vec{H}_1 - \vec{H}_2) = 0$, $\vec{n} \times (\vec{E}_1 - \vec{E}_2) = 0$. The outer edge of the air layer is set to be a perfect magnetic conductor, although, as the air layer was set to be thick enough to obtain zero electric field at its edge ($R_{air} = 125\mu$m), either boundary condition would be suitable. On the other hand, this layer was thin enough not to impair the mesh quality. When the symmetry is used, the boundary conditions at the radial edges of the structure are chosen dependent on a mode class as is shown in Fig. 2.5 and explained below.

2.2.1 Symmetry of PCFs and its Implications for Modelling

The fibre symmetry has twofold impact on modeling of LPGs. Firstly, it is commonly exploited to reduce the simulated waveguide cross section, making a very fine meshing feasible [64]. Secondly, due to the constraints imposed on the field vectors, the symmetry assists the analysis of mode coupling.

From the cross sections of the fibres shown in Fig. 2.1 it can be seen that, apart from a few irregularities in the structure of LMA, the studied PCFs have six axes of reflection (mirror) symmetry and a rotational symmetry with the invariant angle of $\pi/3$, and therefore belong to the C_{6v} symmetry group. The modes of a waveguide with this symmetry can be divided into eight symmetry classes according to the irreducible zones and the boundary conditions, [64], [65]. There are four degenerate and four non-degenerate classes. Modes are considered degenerate if they have the same propagation constant and their fields can be derived from each other by the a composition of the operations of the symmetry group.

Degenerate modes of the C_{6v} group belong to the classes 3,4,5,6 and their irreducible zone is a part of the fibre cross section with the angle $\pi/2$. Non-degenerate modes belong to the classes 1,2,7,8 and their irreducible zone has the angle $\pi/6$. Four classes in each subgroup are the result of permutations of the two boundary conditions: perfect magnetic conductor $\vec{n} \times \vec{H} = 0$ (solid line in Fig. 2.5) and perfect electric conductor $\vec{n} \times \vec{E} = 0$ (dashed line in Fig. 2.5).

Since an irreducible zone contains the complete information on any mode of that class, it

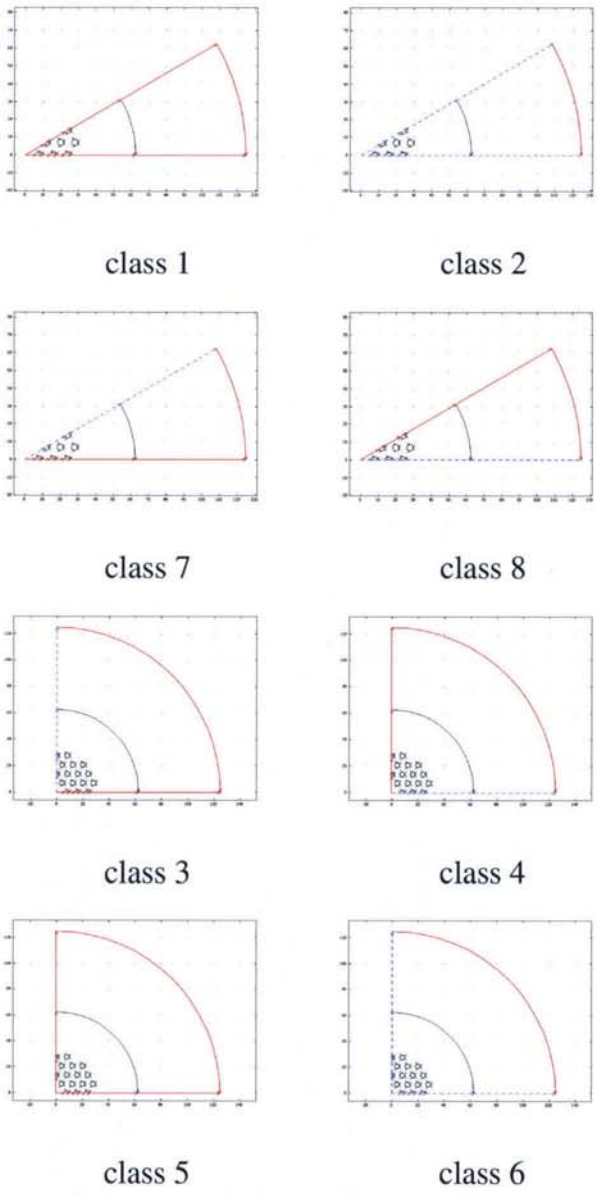

Figure 2.5: Symmetry classes of the ESM PCF. Boundary conditions are given by: solid red line - perfect magnetic conductor, dashed blue line - perfect electric conductor.

is sufficient for modelling of the fibre and enables the refinement of the mesh that is critical for the precise calculation of the propagation constants and the field profiles of the eigenmodes. This requirement does not present a problem in most applications since the only modes of interest are the core modes. The analysis of the cladding modes is specific for the resonant structures and in the particular case of the LPGs in PCFs it is complicated by the geometry of the fibre. Figure 2.6 shows the notable improvement in the mesh finesse when the simulated part of the cross section was reduced, rendering approximately 19 times more mesh elements in the cross section of the fibre.

The coupled mode theory is based on the assumption that the electric field of the input

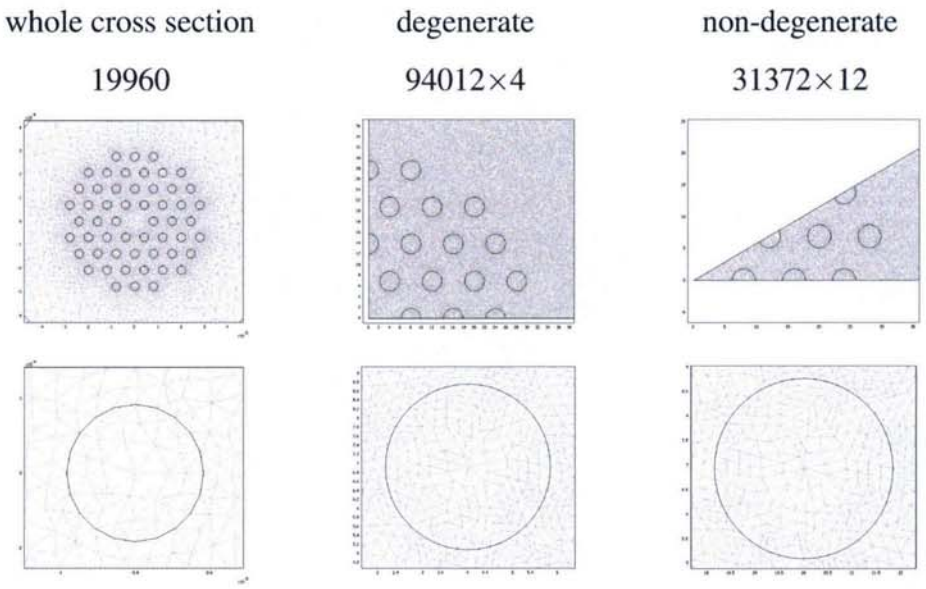

Figure 2.6: Mesh refinement by the use of the fibre symmetry. Numbers in the header represent the number of the mesh elements in the whole cross section of the fibre. Top row: optimal meshes for the whole cross section and for the irreducible zones. Bottom row: the mesh over one hole for each geometry.

mode can excite the field of the other mode via the linear polarisation. Only the parallel components of the electric fields can be in resonance. This is reflected in the expression for the coupling coefficient (1.3) comprising the dot product of the electric fields of the resonant modes and the index perturbation. If the fields are parallel and in phase the scalar product will reach maximum, whereas when the fields are perpendicular to each other, it will be zero and no coupling will occur. The latter is a reformulation of the fact that in the optically inactive material perpendicularly polarised modes do not interfere, i.e. they are independent. If

the grating is considered to be a symmetric perturbation, only slightly changing the transversal invariance of the fibre, the identification of the resonant mode is facilitated by limiting the choice to those cladding modes that have the same polarisation as the core mode, for instance the LP modes in the step index fibre.

An implementation of the previous considerations and examples of degenerate and non-degenerate modes are given in Sec. 2.2.3.

2.2.2 Numerical implementation

Numerical tests were performed to ensure the accuracy, precision and convergence of the method. Numerical precision and accuracy are defined as in physics. Numerical precision is the difference in the refractive indices of the degenerate core modes and it is also referred to as numerical birefringence. It is theoretically zero, [64], but due the nonperfect meshing and the errors in calculation, it appears in the model. Numerical accuracy is difference between the calculated value and that obtained by the reference numerical method.

First, the simple step-index waveguide was compared to the analytical and numerical values found in the literature [66]. The results in Table 2.1 show that the accuracy of the FEMLAB is superior to that of the other two methods.

Two models of the PCF were tested, with and without using symmetry. In the case of

number of grid elements	analytical	full-vectorial FD [66]	FD BPM [67]	current work
120	1.438604	1.438613	1.43614	1.438604

Table 2.1: Comparison of the finite difference (FD), finite element (FE) and analytical method, based on calculation of the effective refractive index of the fundamental mode of the step-index waveguide with parameters: $n_{co} = 1.45$, $n_{cl} = 1$, $r_{co} = 6\mu$m, $\lambda = 1.5\mu$m.

the full model the finest mesh for which it was possible to obtain the solution was chosen, where the limitation was the performance of the computer. These results were benchmarked to CUDOS [68] that uses the modal method and exploits the symmetry of the fibre. Results are compared in Table 2.2. The accuracy of the symmetric model was better than 3×10^{-7} whereas the accuracy of the full model was two orders of magnitudes worse. The numerical precision of both configurations was of the order of 10^{-7}. Such an outcome was

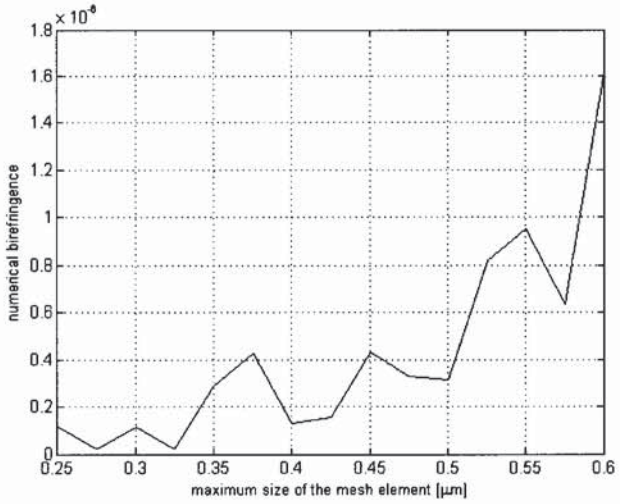

Figure 2.7: Numerical birefringence of the ESM PCF vs. the maximum size of a mesh element in silica.

expected as the mesh over the whole cross section could not be refined as much as the mesh over the quarter of the cross section. As the investigated shift in the grating spectrum was independent of the attenuation of the fibre, the imaginary part of the order 10^{-14} could be neglected. The only exception is the sensitivity to the refractive index where this simplification is supposed to be the main source of error. Finally, the optimal mesh was chosen based on the convergence of the numerical birefringence as shown in Fig. 2.7. The maximum size of the mesh element in silica was set to 0.4μm as a compromise between the precision and the time of the calculation. Thereby achieved precision was better than $2 \cdot 10^{-7}$ for the core modes and 10^{-6} for the inner cladding modes.

The numerical error of our model should be assessed in relation to the requirements that come from properties of the studied LPGs. For the main criterion we take the position of the resonant wavelength as the essential property of LPG. The error in the calculated effective

	$n_{co_x}^{eff}$	$n_{co_y}^{eff}$	birefringence
full	1.4438472	1.44384648	$7.2 \cdot 10{-}7$
class 3	1.44382470	-	$3 \cdot 10^{-7}$
class 4	-	1.4438250	
CUDOS	$1.4438244 + i5.3 \cdot 10^{-14}$	$1.4438244 + i5.3 \cdot 10^{-14}$	0

Table 2.2: Comparison of the results obtained by FEMLAB and CUDOS for the effective refractive index of the core mode of the PCF with four rings of holes.

refractive index of the mode is smaller than 10^{-6}. In the first approximation, the corresponding error in the calculated beat length for 500μm grating is given by $\Delta\Lambda = \frac{2\Delta n\Lambda}{\delta n} \approx 0.4\mu$m. This results in an approximate error of 1 nm in the position of the attenuation band which is satisfactory and is much better than the repeatability achieved in experiments (6.5 nm, see Sec.2.6.2).

To conclude, it has been shown that the chosen numerical method provides a very precise calculation of the propagation constants which satisfies the requirements of the model.

2.2.3 Results of the Modal Analysis of PCFs

Due to the finiteness of the photonic crystal and the presence of the bulk cladding, an endlessly single mode fibre can support many modes apart from the core mode. In relation to the geometry of the fibre, Fig. 2.1, these modes can be divided into modes propagating through the core, the photonic crystal and the outer cladding. Confinement of the core mode was explained by the effective index model, [40]. As the interface between the core and the photonic crystal does not exist, and therefore total internal reflection does not occur, some light will escape from the core and due to the finiteness of the photonic crystal part of this light will reach the outer cladding. Light that manages to escape to the cladding is lost by refraction at the holes or absorbed by the fibre coating. As a part of the preparation for the grating fabrication the coating is removed so that bulk silica cladding is in direct contact with air. *All the simulations and further discussions assume that the fibre coating has been removed.* Due to the total reflection at the air-silica interface there can be guided modes in the bulk outer cladding. From the inner side they are confined by the crystal in the same way as the core mode. The guided modes propagating mainly through the photonic crystal spread to both core and cladding. Examples of the mode profiles are shown in Fig. 2.8

The modes in figure 2.8 were chosen so that different symmetry classes could also be illustrated. It would be enough to simulate only the degenerate classes with a $\pi/2$ irreducible zone because they are parents of the non-degenerate classes just as the whole cross-section is the parent of the degenerate classes. For example, the mode in Fig. 2.8f) belongs to the class 8 and the mode in Fig. 2.8i) to the class 4 but they are the same up to the phase factor of π.

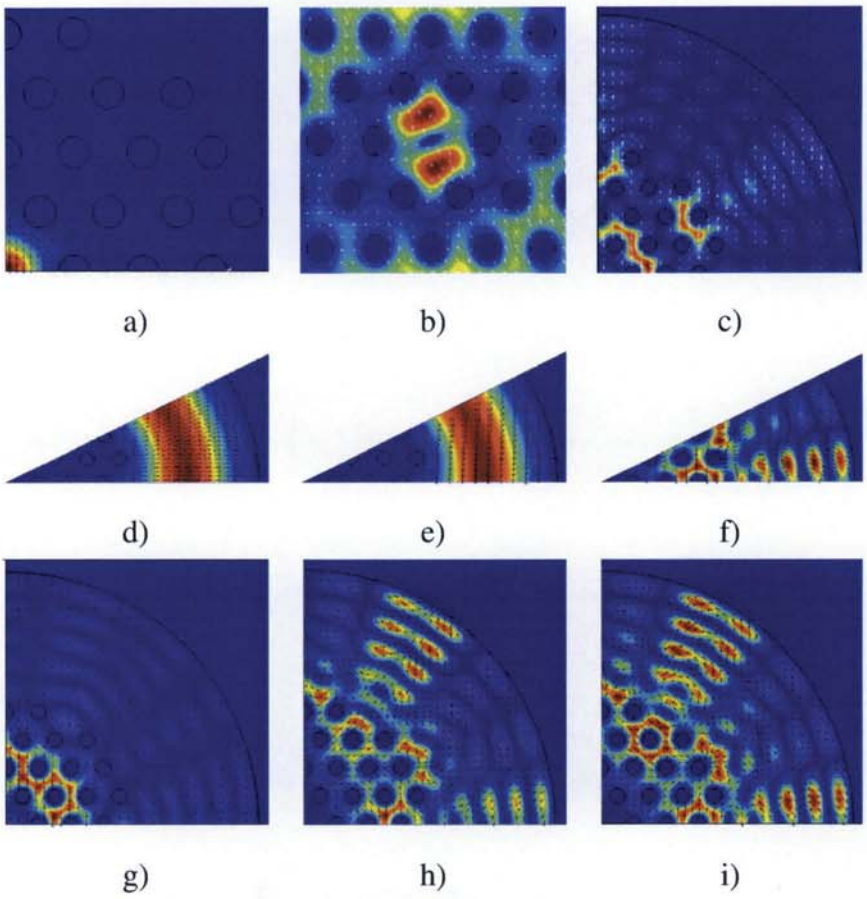

Figure 2.8: Examples of modes guided by the ESM PCF.

The mode order is determined by the requirement that the lower order mode has bigger propagation constant, i.e. higher effective refractive index. The physical reason for such ordering is the principle of minimal energy. Namely, the lower order mode is the mode which carries less energy or in the terms of mathematical physics, the mode that has smaller energy functional $E_f(\vec{H}) = \frac{<\vec{H},\nabla\times(\frac{1}{\varepsilon}\nabla\times\vec{H})>}{2<\vec{H},\vec{H}>}$, [69]. The mode that minimizes E_f is fundamental. For the plane wave E_f becomes the Laplacian operator $E_f \approx \triangle_t + (ik_0 n_{eff})^2$. From the last two equations it can be concluded that the energy of the mode is lower if it (*i*) propagates through the medium with the higher refractive index and (*ii*) has the minimal spatial variation across the cross section. In the undoped PCF both the central part and the bulk cladding have the same refractive index and the criterion (*i*) is not applicable. The other criterion is better met by the bulk cladding as it offers more space for the mode. Indeed, the eigenmode analysis of the PCF showed that the core mode of the stripped fibre is preceded by the whole gallery of the bulk cladding modes with higher refractive indices. In Fig. 2.9 the core mode is 76th.

Higher order modes are in the bulk cladding, photonic crystal or in the core. As the degenerate modes can be counted twice or not, the absolute mode numbers are subject to convention. In the coated fibre, only the core mode does not suffer significant losses and it does not have the cut-off over the large span of wavelengths, [40], so that it is the fundamental mode of PCF.

Since the photonic crystal fibres come in a variety of geometries, classification and de-

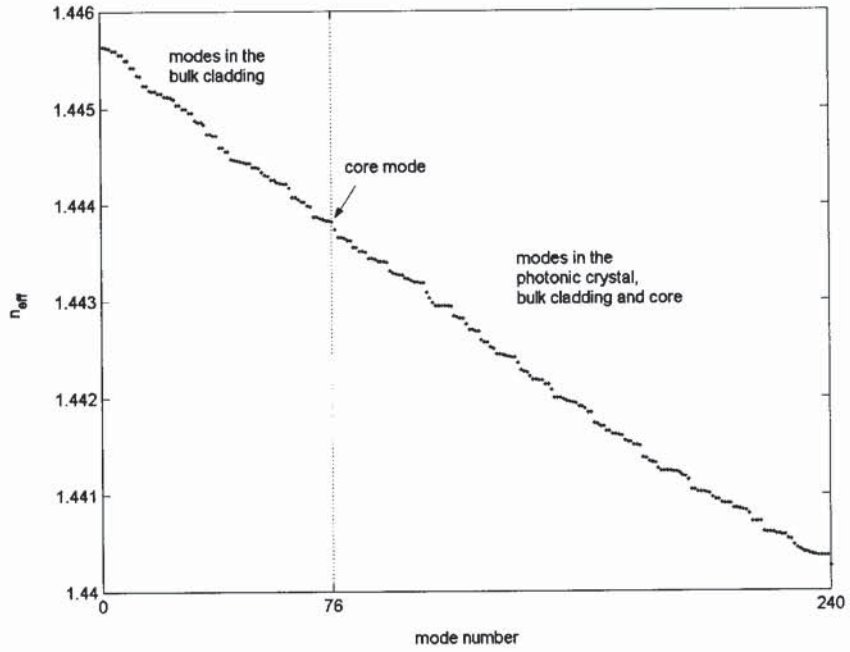

Figure 2.9: Effective refractive indices of the first 240 modes guided by the ESM PCF.

notation of the modes is usually done ad hoc, often in analogy with the HE and EH modes of the step-index fibre, [53, 70]. In this thesis we predominantly deal with modes similar to the LP_{0m} modes of the step-index fibres.

2.2.4 Analogy Between the PCF with the Bulk Cladding and W-shaped Fibre

The analogy can be drawn between the geometry of the analysed PCFs and W-shaped fibres with a depressed cladding, as is suggested by the inset in Fig. 2.10. The W-fibre correspond-

ing to the PCF is obtained by replacing the holey region with a homogeneous material of the refractive index equal to the refractive index of the photonic crystal, which is defined as a square root of the geometrical average of the dielectric permittivity over the photonic crystal. The core and inner cladding radii of the W-shaped fibre were found by fitting its core mode order to that of the PCF. For example, the best fit to the ESM PCF at $\lambda = 1.4\mu$m was obtained for the core radius 6.65μm. It is bigger than the geometrical core radius of the ESM given by $R_{co} = L - R_h = 6.16\mu$m because the core mode penetrates to the crystal and is well beyond the first ring of holes at this wavelength. The results of the fit are shown in Fig. 2.10. Effective refractive indices of the core and the bulk cladding modes are fitted well to the effective mode indices of actual PCF. However, the analogy does not extend to the modes in the photonic crystal part of the PCF as they cannot be modelled by the modes propagating through the depressed cladding. Namely, modes can propagate through the depressed cladding only if their effective indices are below the index of the cladding, e.g 1.38 at 1.4μm for the analog of the ESM PCF, whereas the modes in the photonic crystal propagate mostly thorough the pure silica their indices being much higher, around 1.44 at 1.4μm.

The other difference between the two fibres comes from the their different symmetries. With the 4-fold degeneracy of the cladding modes due to its circular symmetry, Fig. 2.10, the W-shaped fibre cannot account for the properties of the PCF and PCF-based devices that depend on the direction of the field vectors, e.g. polarisation effects.

Due to the serious shortcomings, the application of the W-fibre model to LPGs is limited to the qualitative analysis only, but the insight it gives can be a very useful tool, e.g. for describing the impact of the induced index change as in Sec. 2.4.4.

2.3 Modal Analysis and Index Profiling of LPGs in PCFs

Coupled mode theory was applied to the LPGs described in Sec.2.1.2 in order to identify resonant modes responsible for the attenuation bands in the grating spectra. Once the resonant modes are known, it is possible to retrieve the index profile of the grating using the calculated mode profiles and the appropriate model of the index change.

The change in the refractive index in the crystal is approximated by the and expressed as

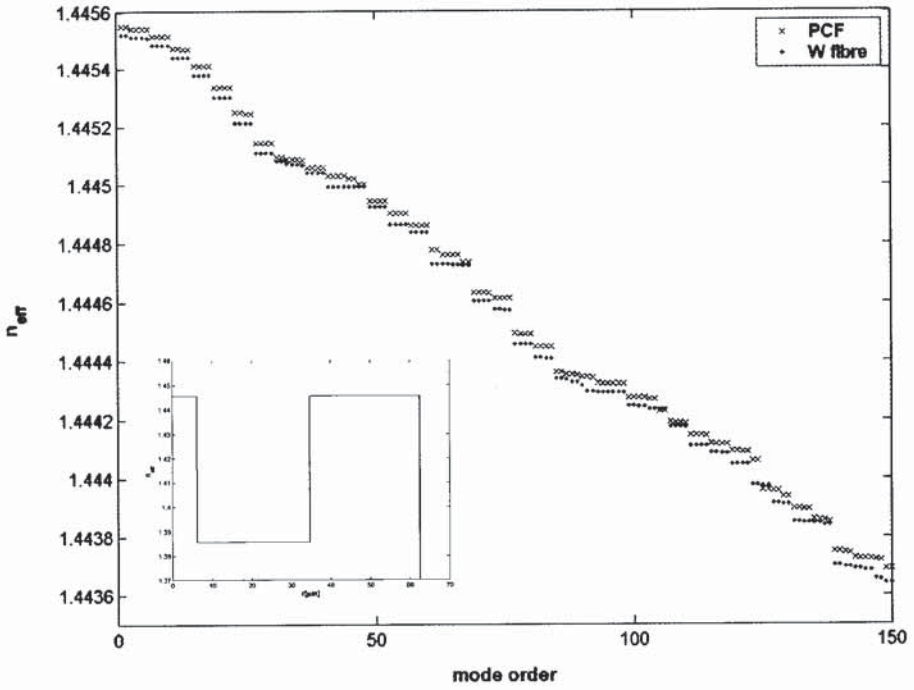

Figure 2.10: Effective refractive indices of the modes of the ESM PCF (x) and the analogous W-shaped fibre (•). Inset: refractive index profile of the W-shaped fibre.

the function of two parameters: change in the index of silica, Δn_{sil}, and the radius of holes, R_h. Resonant cladding modes were identified using the phase matching condition. As there were several candidates for the resonant mode, the correct solution was selected based on the overlap integrals and the symmetry. Once the resonant modes were known and the model for index change established, the remaining step was to obtain the parameters Δn_{sil} and R_h that give the best fit to the experimental data. For this purpose the growth of the attenuation peak during the fabrication of the grating was used. At the end of this section the limits and the refinements of the method are discussed.

2.3.1 Resonant Modes

The core mode couples to the cladding modes that satisfy the phase matching condition 1.7. The same grating can couple light to many different modes at different wavelengths, the higher the mode order, the shorter the resonant wavelength. Figure 2.11 is a graphic rep-

resentation of the phase matching condition showing the dependence of the beat length on the wavelength given by $\Lambda_B = \frac{\lambda}{\delta n^{eff}}$. It was obtained by calculating the effective refractive indices of the modes of the ESM PCF as in Fig. 2.9 over the range of wavelengths.

The resonant wavelength is found in the intersection of these curves and the line $\Lambda_B = \Lambda$

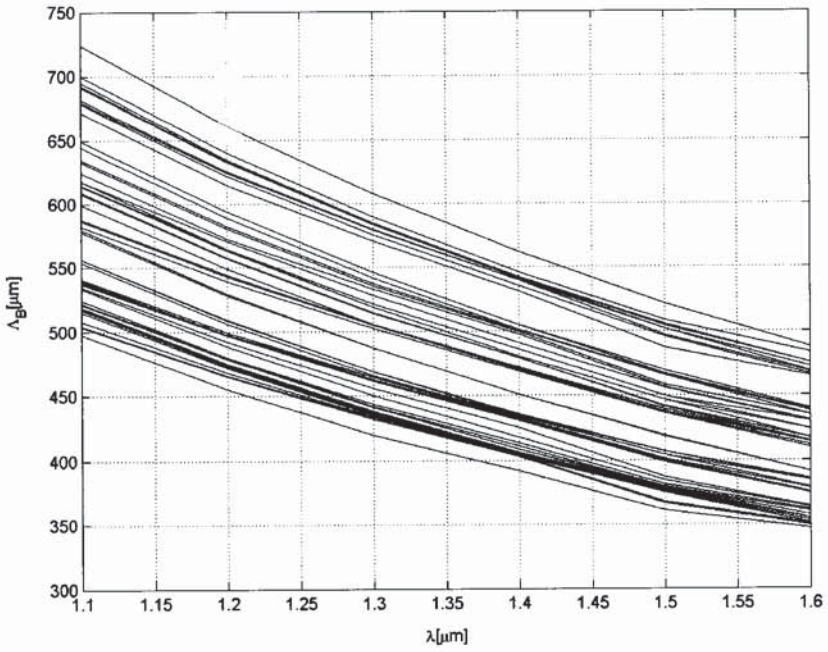

Figure 2.11: Beat length required for the core – cladding mode coupling as a function of wavelength. The higher is the mode order, the smaller beat length is required.

where Λ is the grating period. The negative slope of the curves confirms experimental observation that the increase in the period of LPG causes the blue shift of the spectrum, which is a consequence of the dispersion of the PCF, in particular the waveguide dispersion. Influence of the material dispersion is negligible because the light propagating through the PCF propagates mostly through silica and its effects on the core mode and cladding modes cancel each other. Material dispersion gains importance at wavelengths larger than the hole diameter because the light penetrates into the air holes more and the dispersion coefficients of the air and silica are different. The waveguide dispersion is subject to the same effect which can be explained by the effective index model. As the wavelength increases and the light penetrates into the air holes more, the effective refractive indices of the modes propagating through the photonic crystal decrease and the core-cladding mode index difference increases. If the increase in the index difference with λ is faster than linear, the beat length decreases and the

slope of the curves is negative, as is the case in Fig. 2.11. For completeness, it should be mentioned that for longer wavelengths or smaller holes the opposite sign of the slope and the existence of the turning point have been predicted, [51].

The detection of the resonant mode has been carried out in two steps: (*i*) detecting the modes the effective refractive indices of which best satisfy the phase-matching condition and (*ii*) choosing the right mode by comparing the coupling coefficients, whereby in many cases the step (*ii*) can be bypassed by exploiting the mode symmetry. Each of these steps is explained on the example of 500μm in the ESM PCF.

Possible resonant wavelengths can be determined numerically by the interpolation of functions $\lambda(\Lambda_B)$ for each mode at the point $\Lambda_B = \Lambda$. As the difference in refractive indices of the successive cladding modes can be very small, the procedure may not give the unique solution and the additional constraints must be imposed. This is achieved by the analysis of the mode profiles because only the modes that overlap with the core mode in the region in which the refractive index change occurred can be excited by the grating. The overlap between modes is quantified by the overlap integral: $I = \iint \vec{E}_1(x,y)\vec{E}_2^*(x,y)dxdy$. As the modes are orthogonal, the integral over the whole cross section should be zero, but due to the numerical errors that appear in the calculation of the mode profiles and the integration, the calculated overlap integral is usually close to zero and its value can be used as an estimate of the numerical accuracy. Coupling coefficients were evaluated over each part of the fibre in which the index change can be considered constant: core, photonic crystal and cladding. As the core mode is heavily attenuated before it reaches the bulk cladding, the coupling is restricted to the core and the photonic crystal. The mode with the biggest overlap with the core mode is the resonant mode.

Being linearly polarised, the core mode is likely to be coupled to the cladding mode linearly polarised in the same direction. As the orientation of the electric field is conditioned by the class the mode belongs to and as the core mode is degenerate, the resonant cladding mode must be found among the modes of the same class.

The grating spectrum in Fig. 2.4 has the main resonance at 1402 nm and the next at 1239 nm. From Fig. 2.11 it can be seen that there are three modes around the point $\lambda =$ 1402 nm, $\Lambda = 500\mu$m. Having analysed the fibre without taking into account any changes induced by arc, we must allow for the small error in the grating characteristics, which has

for the consequence that none of these curves passes exactly through the resonant point. The profiles of these modes and the core mode are shown in Figs. 2.8 g), h), i), a). All of them can be derived from the class 4. As the fields of the nearly circular cladding mode and the core mode are linearly polarised and parallel, the coupling between them is expected to be much bigger than between the core mode and the other two cladding modes. The calculated overlap integrals for all three cladding modes and the core mode in the core, photonic crystal and cladding are given in Table 2.3. Please note that the overlap integrals are normalised so that the power carried by a mode is 1W as in Sec.1.5.1[1]

The overlap integrals of the core mode and the mode M1 are approximately 10 times bigger

mode	core	photonic crystal	bulk cladding	Σ
M1	-21.37	21.65	5.7×10^{-4}	0.282
M2	1.51	-1.52	1.3×10^{-4}	-0.010
M3	0.20	-0.23	-1.7×10^{-5}	-0.024

Table 2.3: Overlap integrals between the core and the cladding modes suspected to be resonant at 1400nm. Core mode is shown in Fig. 2.8 a) and the modes M1,M2,M3 correspond to the modes in Figs. 2.8 g), h), i), respectively. Normalisation is explained in the footnote 2.

than those for M2 and 100 times than those for M3. The assumptions based on the symmetry of PCF are thereby confirmed numerically and the mode M1 is identified as resonant. Its profile is shown in Fig. 2.12.

The deviation of the values in the last column of Table 2.3 from 1 indicates the error of the calculation of overlap integrals, which can was used to estimate the accuracy of the coupling coefficients. Fig. 2.13 shows the function $\vec{E}_{co}\vec{E}^*_{cl}$ which is the integrand in the overlap integral.

It is apparent that a significant coupling may only occur in the core and the photonic crystal.

2.3.2 Vectorial Representation of the Coupling Coefficients

The key adaptation of the classic coupled mode theory to the studied LPGs is the vectorial representation of the coupling coefficients. Under the assumption that the grating is sinusoidal coupling coefficients given by equation (1.5) enter the coupled mode equations (1.8)

[1]More general normalisation of the field amplitude $|\vec{E}| = 1$ would generate overlap integrals from the table divided by $2\omega\mu/\beta \approx 520$

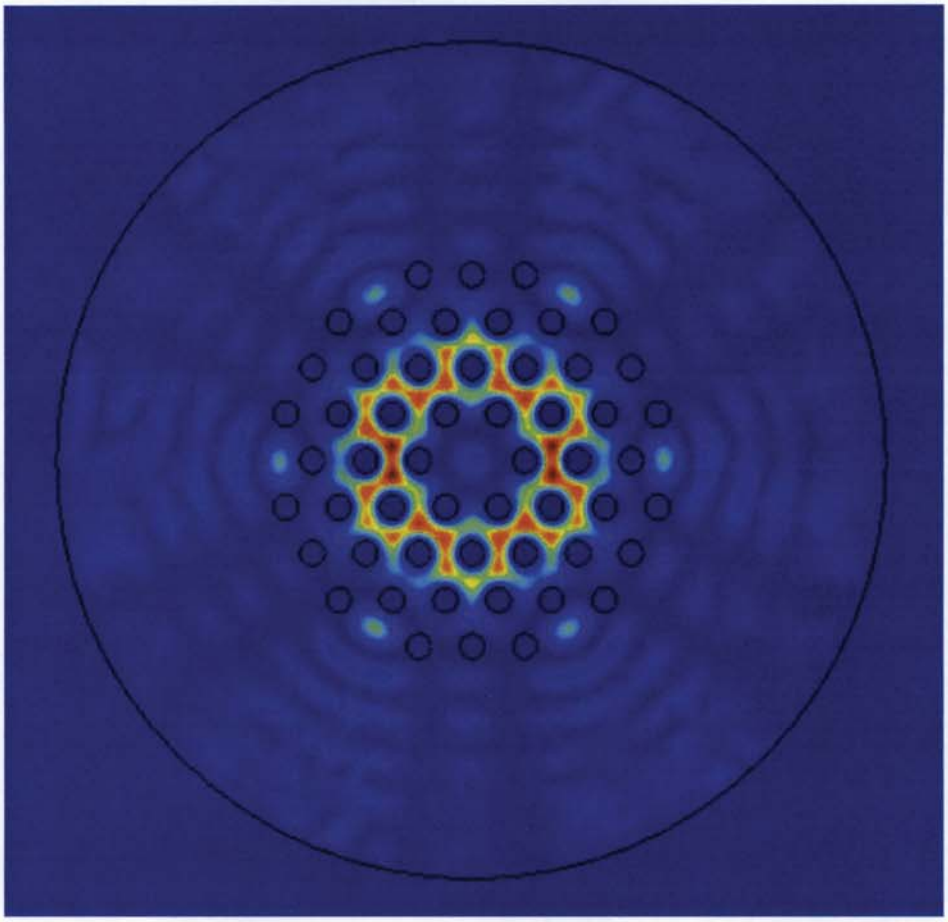

Figure 2.12: Mode of the 500μm LPG in the ESM PCF resonant at 1400nm.

and (1.9) through the coupling constants given by (1.6). As opposed to the UV grating inscribed in the core, in the case of the grating fabricated by the electric arc the integration in (1.6) goes over the whole cross section of the fibre. Based on the earlier considerations, the index change in the photonic crystal is approximated by

$$\Delta n_{pc} = \sqrt{<\varepsilon(x,y)>} = \sqrt{\frac{(R_{pc}^2 - N_h R_h^2 - R_{co}^2)\varepsilon_{silica} + N_h R_h^2}{R_{pc}^2 - R_{co}^2}} \tag{2.2}$$

where ε_{silica} is the average dielectric constant of silica, N_h the number of holes, and R_{co}, R_{pc}, R_{cl} radii of the core, the photonic crystal and the outer cladding. Under the simplifying assumption that the index change is constant across each part of the PCF and equals Δn_{co} in the core, Δn_{pc} in the photonic crystal, Δn_{cl} in the cladding, self-coupling coefficients κ_{co} and

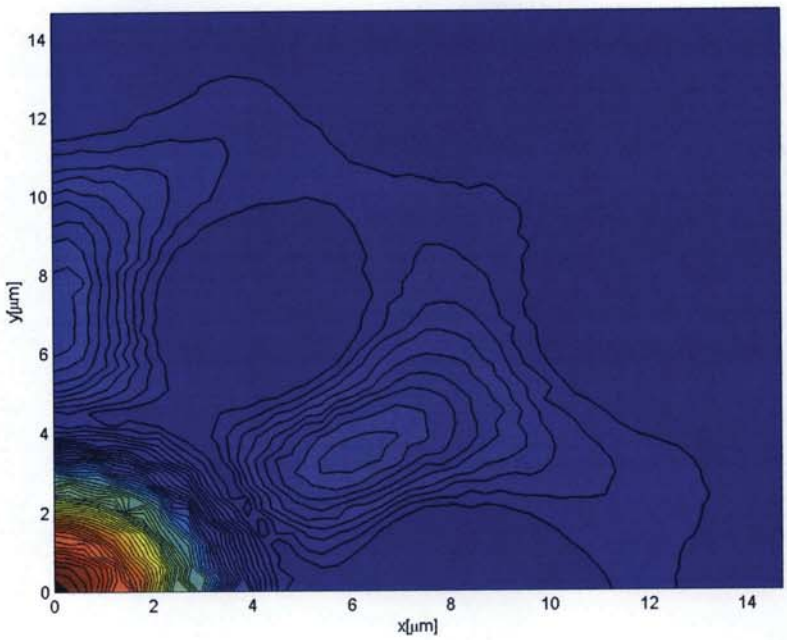

Figure 2.13: The dot product of the electric field vectors of the core and the resonant cladding modes.

κ_{cl} and cross-coupling coefficient κ can be approximated by the matrix equation:

$$\begin{pmatrix} \kappa_{co} \\ \kappa \\ \kappa_{cl} \end{pmatrix} = \frac{\omega\varepsilon_0 n}{4} \begin{pmatrix} I_{co}^{co-co} & I_{pc}^{co-co} & I_{cl}^{co-co} \\ I_{co}^{co-cl} & I_{pc}^{co-cl} & I_{cl}^{co-cl} \\ I_{co}^{cl-cl} & I_{pc}^{cl-cl} & I_{cl}^{cl-cl} \end{pmatrix} \begin{pmatrix} \Delta n_{co} \\ \Delta n_{pc} \\ \Delta n_{cl} \end{pmatrix} \tag{2.3}$$

where ω is the resonant frequency, n is the refractive index of silica and I^{co-co}, I^{co-cl}, I^{cl-cl} are overlap integrals in the region given by subscript. The overlap integral is defined by the expression $I = \iint \vec{E}_1(x,y)\vec{E}_2(x,y)^* dxdy$. Since in the PCF there are no precise boundaries between the core and the photonic crystal and the photonic crystal and the outer cladding, an ad hoc definition of the subdomains must be adopted. In the calculations of integrals and the refractive index of photonic crystal performed here the edges of the subdomains were based purely on the geometry of the fibre, hence the core radius was defined as $R_{co} = L - R_h$ and the outer radius of the photonic crystal $R_{pc} = \sqrt{(N_r L + R_h)^2 + L^2}$, where L is the separation between holes, R_h the hole radius and N_r the number of rings. This definition was more suitable than the definition based on the effective mode radius because it is both straightforward and independent of wavelength. Since the numerical error in the integration algorithm comes partly from the interpolation of the filed amplitudes and partly from the inadequateness of

the rectangular grid at the edges of the subdomains, some level of uncertainty is unavoidable. However, it is relatively small because the integral over the bulk of the subdomain where the most of the field is concentrated is much bigger than the integral over the narrow region around the edge. Any other similar definition of subdomains would also give the acceptable results.

2.3.3 Influence of Changes in the Index Profile on the Coupling Coefficients

The overlap integrals from the matrix 2.3 for the core and the first resonant mode of the 500μm LPG in the ESM PCF are given in Table 2.4.

They depend on the fibre geometry and the refractive index. In order to estimate the contribution of each of these changes, the overlap integrals were calculated for different refractive indices and for different radii of holes. The index of silica was varied for 10^{-3} around the index at 1400 nm and it was found that the maximal change in the overlap integrals was 0.3%. Therefore, the noneligible effect of the induced index change on the coupling coefficients is only through the term Δn. On the other hand, the effect of the reduction in the hole diameter on the overlap integrals is significant. The dependence of the overlap integrals I^{co-cl} on the hole radius R_h is calculated numerically for $0.9R_h$, $0.8R_h$ and $0.6R_h$, where $R_h = 1.84\mu$m is the hole radius in the unperturbed the ESM PCF, and extrapolated for other values, Fig. 2.14. It is assumed that the holes are changed uniformly, which is valid only if the asymmetry induced by the arc is negligible. This approximation is supported by the very small polarisation induced splitting of the resonant wavelengths of the LPG inscribed in SMF which was measured to be 0.3 nm, [71].

Mode	core	photonic crystal	bulk cladding	Σ
co-co	503.6	16.33	1.65×10^{-6}	519.94
co-cl	-21.37	21.654	5.7×10^{-4}	0.282
cl-cl	2.03	420.56	98.79	521.38

Table 2.4: Overlap integrals of the core and the cladding mode excited by the 500μm LPG in the ESM PCF at 1400 nm.

The conclusions of the last two sections were used to model the transmission of LPG as

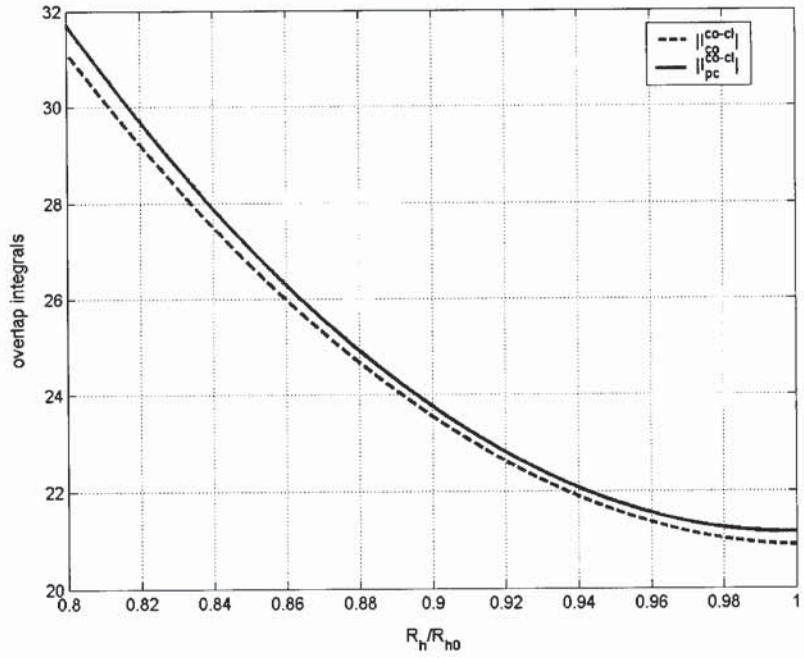

Figure 2.14: Dependence of the absolute values of the overlap integrals of the core and the resonant cladding mode on the hole radius.

a function of changes in the refractive index and the hole radius with the aim to determine these parameters by fitting the obtained transmission function to the spectral characteristic recorded during the grating growth.

2.3.4 Nondestructive Index Profiling of LPG Using the Grating Growth

The idea behind the method is to enable index profiling without the need to disturb the grating. It consists of three stages: developing a model that describes measurable properties of the grating and contains the unknown parameters of the index profile, measuring of these properties, and finding the values of the parameters that give the best fit to the measured data. All prerequisites for accomplishing the first step have been prepared in the previous section. Finalising the model and comparing it to the experimental results are the subjects of this section.

The general expression for the grating transmission spectrum is given by Eqn. (1.10). As the number of the unknown parameters is two (the change in the refractive index of silica,

Δn_{silica}, and the hole radius, R_h), the values of T measured at different wavelengths should give enough information for the fit. However, due to the error in determining the resonant wavelength introduced in both fabrication and modelling and the fact that the equation (1.10) is valid only in the small range of wavelengths around the resonance, this model is not very reliable. Another way to obtain the sufficient number of the experimental data is to measure the spectra of the grating at different stages during its fabrication, i.e. to record the grating growth. Minima of the grating transmission at different grating lengths represent a set of easily available data with adaptable resolution.

The transmission T is minimised for $\zeta = 0$ and is a simple function of the cross-coupling

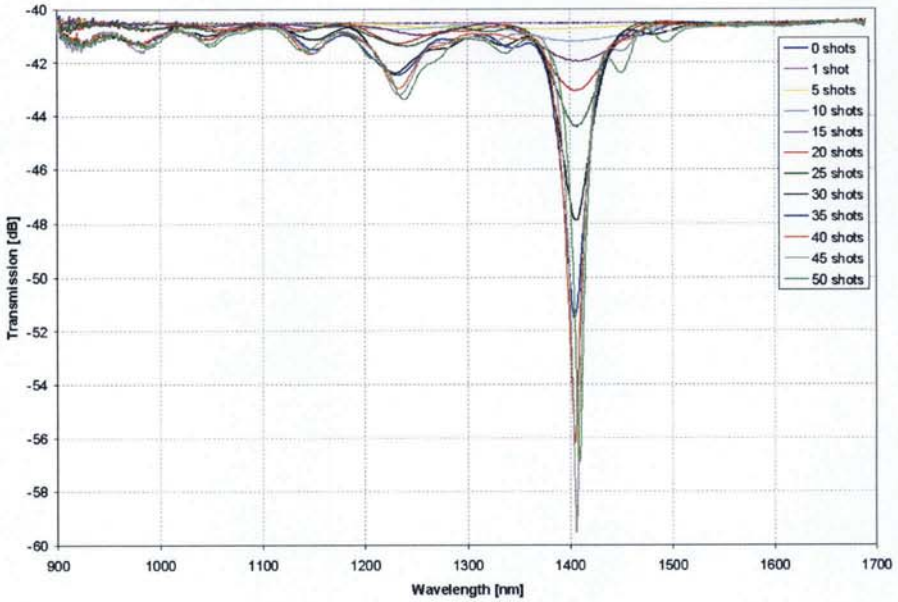

Figure 2.15: Growth of the $\Lambda = 500\mu$m LPG in the ESM PCF recorded during the fabrication by the electric arc.

constant κ and z

$$T(z) = \cos^2 \kappa z \tag{2.4}$$

According to the definition of ζ (1.11) the generalised self-coupling constant becomes zero if the detuning and the difference of the self-coupling constants cancel each other or if they are both zero. An elegant way to find out which of the two is the case is to observe the wavelength shift of the attenuation band during fabrication. It appears due to the accumulation of the index change along the fibre which causes the increase in the self-coupling grating

coefficients κ_{co-co} and κ_{cl-cl}. The design wavelength at which the detuning is zero, λ_{res}, and the wavelength at which the transmission reaches its minimum, λ_{min}, are related by the following equation, [72],

$$\lambda_{min} = \frac{1}{1 - (\kappa_{co-co} - \kappa_{cl-cl})\frac{\Lambda}{2\pi}} \lambda_{res} \tag{2.5}$$

The growth of the 500μm LPG in the ESM PCF is shown in Fig. 2.15. As the LPG did not experience a wavelength shift during the fabrication, it was concluded that for all the lengths of the grating λ_{res} coincided with λ_{min}. Thereby the dispersion of the coupling coefficients was neglected which is justified for the small range of wavelengths in which the shift would be expected. This means that $\kappa_{co-co} - \kappa_{cl-cl} = 0$ and subsequently $\delta = 0$.

The transmission was calculated as a function of Δn_{silica} and R_h using the expression for κ from Eqn. 2.3, interpolated functions for overlap integrals shown in Fig. 2.14 and the expression for $\Delta n_{pc} = \Delta n_{pc}(\Delta n_{silica}, R_h)$, (2.2). From the numerical point of view, fitting of the theoretical to the experimental data was easy because only two parameters were unknown. However, the scarcity of the experimental points, in particular the sharp minimum in Fig. 2.16, caused a considerable error. The estimated index change and the relative change in hole radius were -3×10^{-4} and 0.0007 respectively. This is in accordance with the examination of the grating by the phase microscope in which no change in the hole diameter was detected ($\Delta R_h \approx 1.3nm$ was much smaller than the resolution of the microscope which is limited by the wavelength of the illuminating light). The average index model from Sec. 2.3.5 offers the physical explanation of the above result.

To conclude, we have developed a generic method for the nondestructive index profiling of the LPGs that assume minor restrictions of the index profile. It is applicable to any LPG that can be considered a perturbation in the bulk of the fibre. To avoid errors the number of spectra recorded during the grating growth should be adjusted to the number of the unknown parameters. The accuracy can be further increased by iterating the solution, i.e. by repeating the procedure for the fibre with the index profile obtained in the previous step.

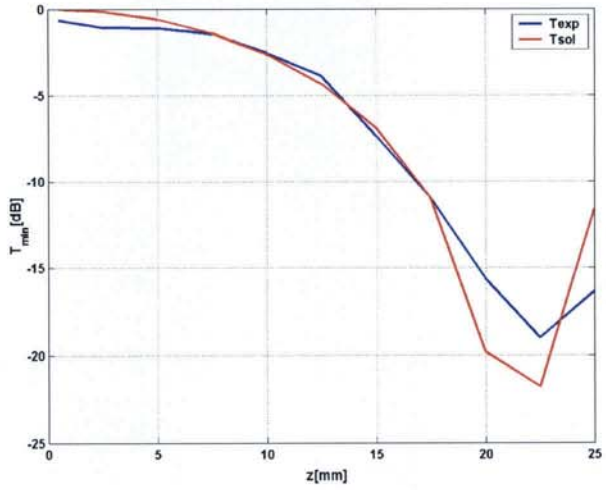

Figure 2.16: Fit of the theoretically obtained data (red line) to the experimentally recorded grating growth (blue line).

2.3.5 Physical Insight Based on the W-shaped Fibre Model

In Section 2.2.4 the W-shaped fibre was suggested as a limited model of PCF and we use it to explain the changes in the index profile.

It was shown that the coupling achieved between the core and the resonant cladding mode in the unperturbed PCF was not big enough to obtain LPGs as strong as in the reported experiments. The index step between the core and the photonic crystal must be reduced to allow for smaller confinement and bigger overlap between the resonant modes. This can happen in two ways: (i) the refractive index of silica is reduced and the holes stay unchanged or (ii) the refractive index of silica is increased and the radius of the holes reduced. It is instructive to examine the dependency of the refractive index of the crystal on these two parameters. Fig. 2.17 shows that it is almost linearly proportional to the refractive index of silica and that it increases quickly with the increase in the hole radius, due to the decrease in the ratio air/silica. Hence when the refractive index of the silica decreases the change in the refractive index of the crystal (Eqn. 2.2) is smaller than the change in the index of the core, and the index step decreases as shown by the dotted line in Fig. 2.18. When the refractive index of silica increases and the hole radius decreases, the index of the crystal increases more than the index of the core as a consequence of the increase of the ratio silica/air in the crystal. Again, the index step decreases. This is illustrated by the dashed line in Fig. 2.18. Due to

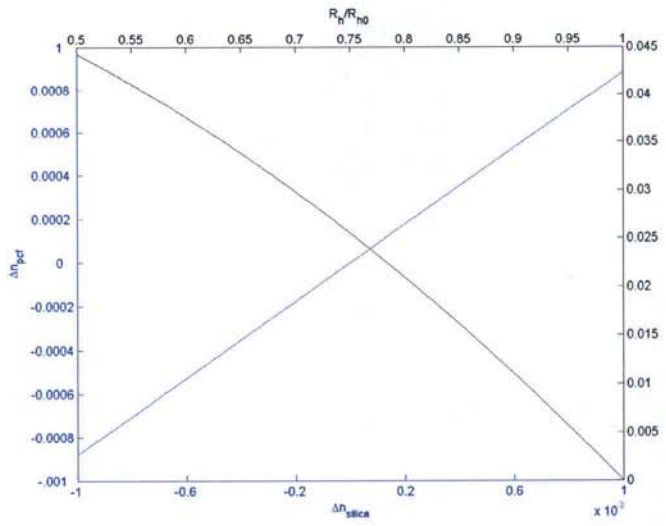

Figure 2.17: Dependence of the change in the refractive index of the photonic crystal on the hole radius (right and upper axes, black line) and the change in the refractive index of silica (left and lower axes, blue line).

the reduction in the hole radius the silica around holes is rarefied which contributes to the reduction in the refractive index, as given be the Lorenz-Lorentz formula, see Eqn. 4.2 in Chapter 4.

2.3.6 Limitations of the Method

Since both the refractive index and the geometry of the PCF may be altered during the fabrication of the grating, assumptions on the perturbative nature of the change in the index profile must be made with care. It has been reported in [11,42] that the index change caused by an arc is of the order of 10^{-4} which is sufficiently small. Another study of the LPGs fabricated in PCFs by the same method, [13], shows that the holes collapse only after extremely long exposure to the arc. However, the effective refractive index of the photonic crystal is very sensitive to the slightest changes in the size of the holes, as shown in Fig. 2.17. For example, the reduction in the hole diameter for 1%, which is 18.4 nm for the ESM PCF, causes the effective index change of 10^{-3}. At the same time the difference between the effective index of the crystal and the refractive index of the pure silica is big, e.g. at $\lambda = 1.4\mu$m, $n_{eff} = 1.38567$ and $n_{silica} = 1.44578$ give $\Delta n = 0.06$. Such a large step allows even the considerable change in n_{eff} to stay within the limits of the perturbation theory.

It is a common practice to assume some average index change and perform the mode

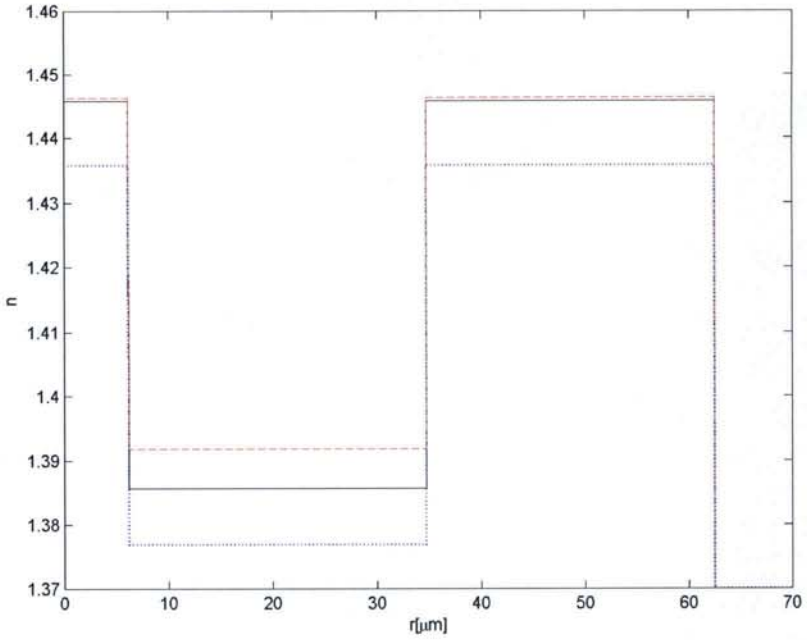

Figure 2.18: Index profile of W-fibre analogous to: an unperturbed ESM PCF (solid line), an ESM PCF with the refractive index of silica reduced and the holes unchanged (dotted line), an ESM PCF with the refractive index of silica increased and the hole radius reduced (dashed line).

analysis of the fibre with this change incorporated. While this is usually not the problem for extensively studied gratings in the core of the step fibre, LPGs in PCFs fabricated by the electric arc are more complicated and such assumptions would be somewhat arbitrary. The approach suggested here favours the iterative solution if necessary instead of making initial assumptions on the changes in the index profile.

The asymmetry of the fibre caused by the electric arc can be included as the second order correction at the expense of introducing a new parameter into the model.

2.4 Sensitivity of LPGs to External Parameters

One of the major applications of LPGs is in sensing of various external parameters as reviewed in the Introduction to the thesis. The investigated LPGs were almost insensitive to temperature while being sensitive to strain, bending and surrounding refractive index, offer-

ing thereby a compact solution to the problem of cross-sensitivity. In the following sections semi-analytical and numerical models of the grating sensitivity are described. The sensitivity is discussed in relation to the waveguide dispersion of PCFs and the conclusions are applied to numerically obtain the temperature, strain and external index sensitivities.

2.4.1 Model of the sensitivity of LPGs

Wavelength shift due to the external effect can be evaluated both numerically and analytically, the latter being the widely used approach for its simplicity and sufficient accuracy. Here we employ both methods and compare the results.

The sensitivity of the resonant wavelength to the external parameter X is obtained by differentiation of the phase matching condition $\lambda = \delta n^{eff} \Lambda$ in respect to X at the point (λ_{res}, Λ):

$$\frac{\partial \lambda}{\partial X} = (\frac{d\delta n_{eff}}{d\lambda}\frac{\partial \lambda}{\partial X} + \frac{\partial \delta n_{eff}}{\partial n}\frac{\partial n}{\partial X})\Lambda + \frac{\partial \Lambda}{\partial X}\delta n_{eff}, \tag{2.6}$$

whereby the total derivative $\frac{d\delta n_{eff}}{d\lambda} = \frac{\partial \delta n_{eff}}{\partial \lambda} + \frac{\partial \delta n_{eff}}{\partial n}\frac{\partial n}{\partial \lambda}$ comprises the waveguide and material dispersion, respectively. After introducing γ as the general sensitivity parameter that describes the feedback of the grating due to the dispersion of the fibre:

$$\gamma = \frac{1}{1 - \Lambda \frac{d\delta n_{eff}}{d\lambda}}, \tag{2.7}$$

the expression for the grating sensitivity to parameter X becomes

$$\frac{\partial \lambda}{\partial X} = \gamma(\frac{\partial \Lambda}{\partial X}\delta n_{eff} + \frac{\partial \delta n_{eff}}{\partial n}\frac{\partial n}{\partial X}\Lambda). \tag{2.8}$$

Grating response to the external parameter contains contributions of the change in grating period and the change in difference in the effective mode indices which depends on the index profile, the geometry of the fibre and the resonant wavelength. Contributions of the material and the waveguide dispersion to γ represent the readjustment of the waveguiding properties of the fibre to the wavelength shift. Whereas the influence of the material dispersion included into the model via Sellmeier's equation had a negligible influence, the complex geometry of the PCF caused the waveguide dispersion different from the dispersion in other fibres.

The physical meaning of γ is better appreciated if it is expressed as $\gamma = \frac{1}{\delta n_{eff}}\frac{d\lambda}{d\Lambda}$, which is easily derived from the partial derivative of the phase matching condition in respect to Λ:

$\frac{\partial\lambda}{\partial\Lambda} = \frac{d\delta n_{eff}}{d\lambda}\frac{\partial\lambda}{\partial\Lambda}\Lambda + \delta n_{eff}$. It is now obvious that γ can be obtained directly from the slope of the LPG characteristic in Fig. 2.11. The negative sign of γ is consistent with the reported blue shift in resonant wavelength when the grating period was increased [10, 13, 29]. As both the sign and the magnitude of γ depend on the fibre geometry, resonant wavelength and mode order, different regimes analogous to the systems with feedback are possible. In our case $\gamma < 0$ and $|\gamma| < 1$, hence the feedback is negative and the sensor output stable. It was proven numerically that the turning points, i.e. the points on the grating characteristic at which $\gamma \to \infty$, may exist in LPGs in PCFs [51], so the enhanced sensing characteristic similar to those reported for standard fibres [73] can be expected. For example, Xuewen *et al.* in [73] describe the LPG that has two resonant wavelengths, one on each side of the turning point. Due to the opposite signs of the grating characteristic at these points, the sensor has the functionality of the differential sensor. In theory, at the turning point the LPG is unstable and its sensitivity goes to infinity. An intriguing concept is the suggestion of the possibility of the grating sensors with the positive feedback based upon the smart selection of the resonant modes and wavelengths and even the particular design of the fibre.

The analytic approximation is practically linearisation of the grating characteristic around the resonant wavelength, therefore it is accurate to the first order and valid for the small wavelength shifts, which is usually sufficient for practical purposes. Precisely, this is a semi-analytical approach because the partial derivative $\frac{\partial\delta n_{eff}}{\partial n}$ and the derivatives in γ can be calculated only numerically.

A numerical method does not suffer from these limitations. It is based on the evaluation of the characteristic of the grating in the fibre the index profile of which is changed under the influence of the external parameter. The new resonant wavelength is found as the point on the grating characteristic corresponding to the new grating period. The grating period changes with the temperature and strain due to the thermal expansion and elasticity of the fibre, but it does not change when only the external refractive index is changed.

Since our model of the grating sensitivity is based on the grating characteristic, it cannot be used when the grating essentially changes its behaviour. Such is the case when it is immersed into the liquid with the refractive index higher or very close to the refractive index of silica. When the external refractive index is very close or equal to that of silica, cladding and the surrounding material form an unbound continuum that does not support discrete cladding

modes and broadband losses are observed. When the index is greater than the index of silica, Fresnel reflection occurs and the portion of the light that is refracted to the surrounding material is lost from the fibre. There may still be a slight shift in the attenuation bands, but a more apparent effect is the increase in their magnitudes [23, 74, 75].

2.4.2 Sensitivity of LPGs to Strain

All the gratings studied had a linear response to strain. The example in Fig. 2.19 shows the response of the 500μm LPG in the ESM PCF which had sensitivity -2.08 ± 0.05 nm/mε.

The analytical expression for the sensitivity to strain was obtained from Eqn. (2.8) by

Figure 2.19: Shift in the main attenuation band of the 500μm LPG in ESM PCF caused by the applied strain. Inset: shift in the resonant wavelength vs. strain [10].

substituting dX by the definition expression for small strain $\varepsilon \triangleq \delta\varepsilon = \frac{d\Lambda}{\Lambda}$ (dimensionless):

$$\frac{\partial\lambda}{\partial\varepsilon} = \gamma\lambda\left(1 + \frac{\partial\delta n_{eff}}{\partial n}\frac{\eta_\varepsilon}{\delta n_{eff}}\right) \tag{2.9}$$

The strain-optic coefficient η_ε was derived from the change in the optical indicatrix, [76], for the field polarised perpendicularly to the direction of the applied strain, $\eta_\varepsilon = -0.5n^3(p_{12} - \mu(p_{12} + p_{11})) = -0.3$ where $p_{11} = 0.121$ and $p_{12} = 0.27$ are the elements of the strain-optic tensor, [76], and $\mu = 0.17$ is the Poisson's coefficient for the pure fused silica, [77]. The derivative $\frac{\partial\delta n^{eff}}{\partial n} = -1.17 \times 10^{-3}$ was obtained numerically by linearisation around

$n = n_{silica}(\lambda_{res})$ and the refractive index range of $\pm 5 \times 10^{-4}$ at the wavelength fixed, corresponding to the variation in strain of $1.6m\varepsilon$. For the case in Fig. 2.19 the calculated strain sensitivity was -1.57 nm/mε.

Another solution was found purely numerically. First, the change in the refractive index

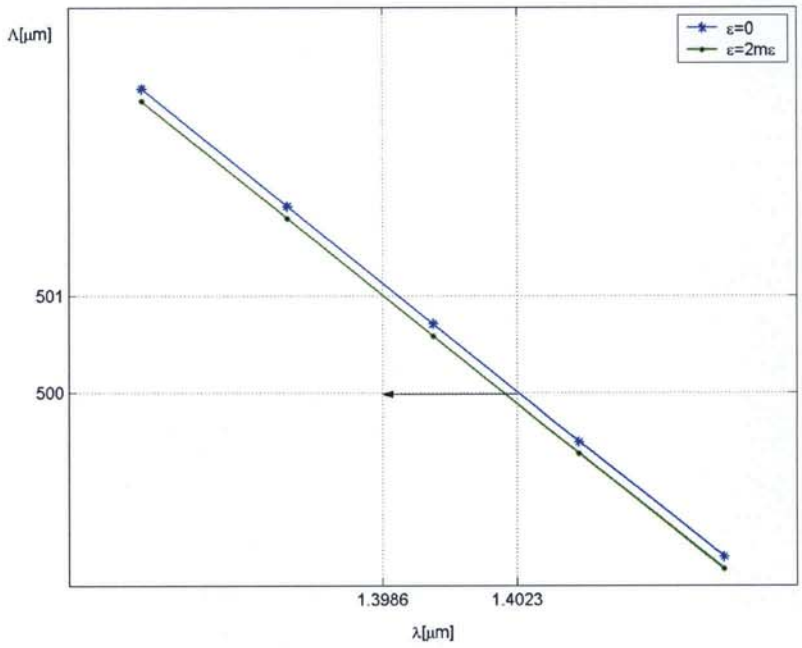

Figure 2.20: Graphic representation of the numerical method for the calculation of the strain sensitivity of the LPG shown in Fig. 2.19. Blue line (*) - beat length of the unstrained grating with the period of $500\mu m$, green line(•) - beat length of the grating under the strain $2m\varepsilon$ with the new period of $501\mu m$. Arrow corresponds to the total wavelength shift.

of the PCF under the maximal strain applied in the experiment, 2 mε, was estimated to be $\Delta n = \eta_\varepsilon \varepsilon = -6 \times 10^{-4}$. Other changes in the fibre such as a reduction in the radius due to the elongation were negligible. The beat length of the strained fibre was calculated in the range of ± 8 nm around the resonant wavelength of the first resonant mode (line with circles in Fig. 2.20) and the increase in the grating period as $\Delta L = \varepsilon L$. The new resonant wavelength was found by interpolation of the Λ curve at the point $L' = L(1+\varepsilon)$, Fig. 2.20. Both contributions to the shift: the change in the index profile of the fibre and in the grating period are present, with the contribution of the change in the grating period prevailing. In the considered case both of them acted in the same direction, causing the blue shift in the resonant wavelength. The final result for sensitivity -1.85 nm/mε differs from the measured

value by 11%. We discuss the possible sources of error below.

The difference in refractive indices had the maximal numerical error of 10^{-7} much smaller than the change in the refractive index induced by strain $\sim 10^{-4}$. The contribution of the numerical error accumulated in the whole process of modelling of the LPG adds up to no more than a few percent. The other suspected contributions to the difference between the results of modelling and the experiment come from neglecting the index change in the eigenmode analysis of the PCF, inhomogeneous distribution of strain due to the presence of the air holes, neglecting the dispersion of the strain-optic coefficients and the experimental error of 2.4%. Fig. 2.21 shows the distribution of axial strain in the cross section of the ESM PCF simulated by a commercial software [78]. The fibre is strained more around the holes than in the bulk cladding region. Comparison with the profile of the resonant mode in Fig. 2.12 shows that the maximal variation in strain in the region occupied by it is around 4% of the applied strain. Taking into account that the contribution of the change in the refractive index is smaller than that of the change in the grating period we may conclude that this is not the main source of error. As the maximal wavelength shift is only a few nanometers, the dispersion of the strain-optic coefficients is negligible. Therefore, the changes in the index profile induced by the electric arc neglected in the initial calculation are suspected to give the major contribution to the error. One way to deal with this problem is to iterate solution so that the index change is refined in every step. Another is to incorporate the assumed index change at the beginning of calculations. Another important issue was the reproducibility of the resonant wavelength. Namely, it was of the order of a few nanometers, larger than the shift under the maximal strain endurable by the grating. The consequence is that each strain sensor would have to be calibrated to find the exact resonant wavelength. In view of these results, the calculated value of the sensitivity can be considered a good estimate.

At the end, the numerical and the semi-analytical methods were compared. As expected, the numerical method was more accurate. The difference in calculated sensitivities of 0.28 nm/mε, corresponding to the wavelength shift of 0.56 nm, was much bigger than the second order refinement of the semi-analytical method $\Delta^2\lambda \approx \Lambda\frac{\partial\delta n^{eff}}{\partial n}\eta_\varepsilon\varepsilon^2 = 0.7$ pm. Therefore, the validity of the semi-analytical model is limited to the small changes in external parameters that cause wavelength shifts of up to a few nanometres. In the case studied, the maximal strain that the grating could survive was small (a few $m\varepsilon$), hence both numerical

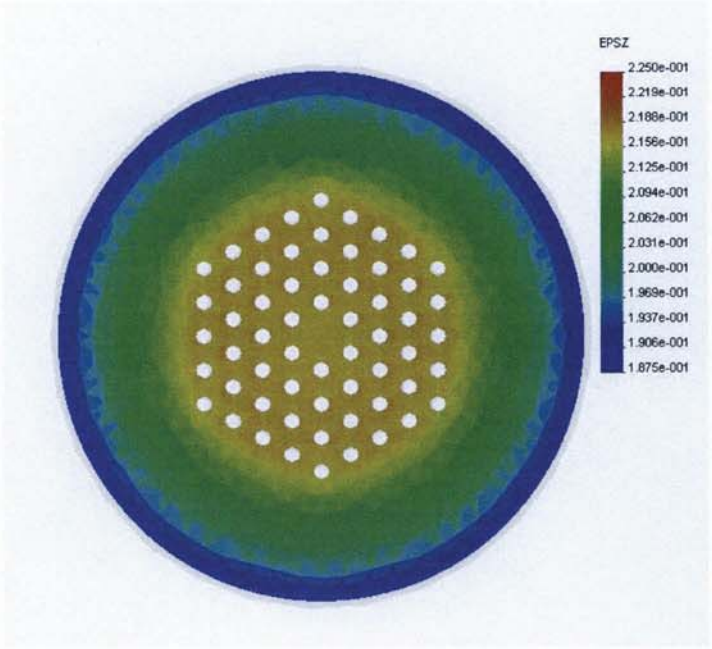

Figure 2.21: Inhomogeneous distribution of the axial strain over the cross section of the ESM PCF. The simulation was done by Dr Tim Earthrowl-Gould, Aston University (2004).

and semi-analytical results were in reasonably good agreement with the experimental results .

2.4.3 Sensitivity of LPGs to Temperature

The sensitivity to temperature of all reported gratings was of the order of a few $pm/^oC$ in the temperature range 20^oC - 90^oC. Although LPGs usually have a linear response to temperature, the results of the measurements performed for the studied LPGs were scattered in the T-$\Delta\lambda$ plane so that the linear regression gave a 50% error in sensitivity, for instance the sensitivity of the 500μm LPG in the ESM PCF was $2 \pm 1 pm/^oC$, Ref. [23]. The sensitivity to temperature was obtained semi-analytically and numerically in a way similar to the sensitivity to strain.

The analytical expression for the LPG's sensitivity to temperature is obtained from the expression (2.8) by introducing the thermal expansion coefficient $\alpha = \frac{\partial \Lambda}{\Lambda \partial T}$ and the temperature-optic coefficient $\eta_T = \frac{\partial n}{\partial T}$:

$$\frac{\partial \lambda}{\partial T} = \gamma\lambda(\alpha + \frac{\partial \delta n_{eff}}{\partial n}\frac{\eta_T}{\delta n_{eff}}) \tag{2.10}$$

For silica, $\alpha = 5 \cdot 10^{-7}/^{\circ}\text{C}$ and $\eta_T = 7.8 \cdot 10^{-6}/^{\circ}\text{C}$, [77]. The derivative $\frac{\partial \delta n_{eff}}{\partial dn}$ was obtained numerically. For the given range of temperatures, the maximal change in the refractive index was 5×10^{-4} so that under the assumption of the linear grating response the derivatives already calculated in Sec. 2.4.2 could be used. The calculated sensitivity to temperature was 3.84 pm/°C.

For the numerical solution the curves presented in Fig. 2.20 were reused. The change in the refractive index of 6×10^{-4} based upon which they were calculated corresponds to the change in temperature of -76.92°C which is just above the range used in experiments. The change in the grating period that occurs as a result of the linear thermal expansion and for -76.92°C is estimated to be $\Delta\Lambda = \alpha\Lambda\Delta T = -19.23$ nm. Interpolation gives the wavelength shift of -0.31 nm and the sensitivity of 4.0 pm/°C.

According to Fig. 2.22 almost the whole wavelength shift is due to the thermo-optic effect.

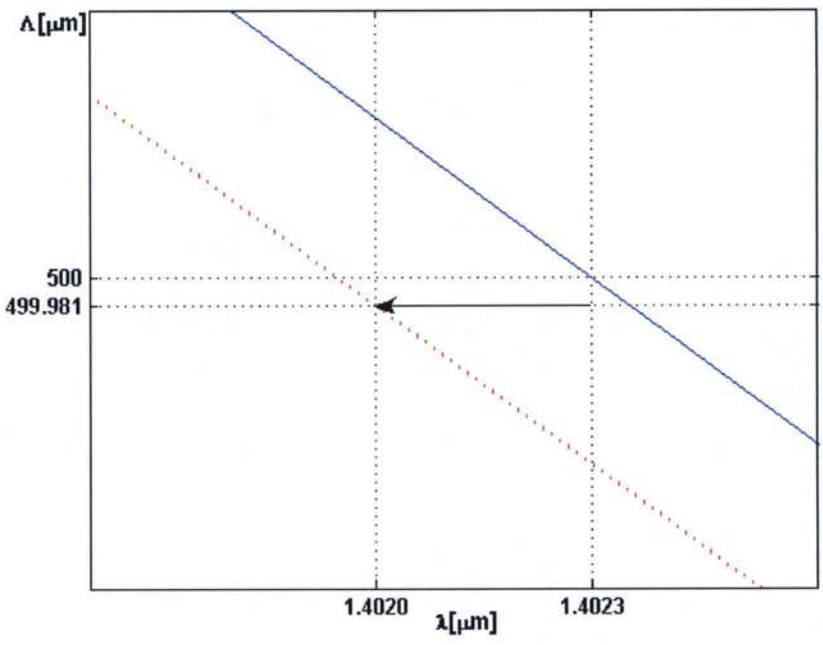

Figure 2.22: Graphic representation of the numerical method for the calculation of the temperature sensitivity of the LPG shown in Fig. 2.19. Solid line - beat length of the grating at the initial (room) temperature with the period $500\mu m$, dashed line - beat length of the grating exposed to the temperature change of -76.92°C with the period changed to $499.981\mu m$.

The thermal expansion of the fibre counteracts it but is too small to make a significant impact. This justifies the simplifications used in the model such as neglecting the volume expansion

of the grating and the stresses caused by the thermal expansion. Comparison with the experimental data shows that the model gives correct order of magnitude and the sign of the wavelength shift, but the calculated sensitivity overestimates the measured value. There may be two reasons for this. First, the temperature span over which the sensitivity was calculated is large and the linearisation may not be justified. The big temperature change was used due to the availability of the numerical data from Sec. 2.4.2 and it is straightforward to repeat the procedure for the smaller range. The more probable reason is large scattering of the experimental data which made it difficult to linearize the experimental points and estimate the sensitivity.

In conclusion, the results of our model of the grating sensitivity to temperature show that the grating response was the wavelength shift of a few pm/°C which can be considered negligible in many applications. This property is an important advantage in the situations in which the cross-sensitivity is undesirable as explained in the Introduction.

2.4.4 Sensitivity of LPGs to the External Refractive Index

The LPGs inscribed in ESM and in particular those in the LMA PCFs were sensitive to the external refractive index. Such behaviour is possible only if a part of the guided light comes into the contact with the surrounding material. Having in mind the geometry of the studied PCFs this is equivalent to the requirement that the part of the resonant mode propagates through the bulk silica cladding. In Sec. 2.3.1 the resonant modes were identified and their profiles shown. For clarity, Fig. 2.23 shows the line plot through the profile of the main resonant mode of the 500μm LPG in the ESM PCF. It can be seen that the resonant mode tails off outside the fibre, but the question remains if this is enough to exhibit the sensitivity to the external refractive index.

Since the change in the external refractive index does not influence the grating period, $\frac{\partial \Lambda}{\partial n_{ext}} = 0$, the analytical expression for the index sensitivity of LPG is straightforwardly obtained by substitution $X = n_{ext}$ into (2.8):

$$\frac{\partial \lambda}{\partial n_{ext}} = \gamma \lambda \frac{1}{\delta n} \frac{\partial \delta n}{\partial n_{ext}} \tag{2.11}$$

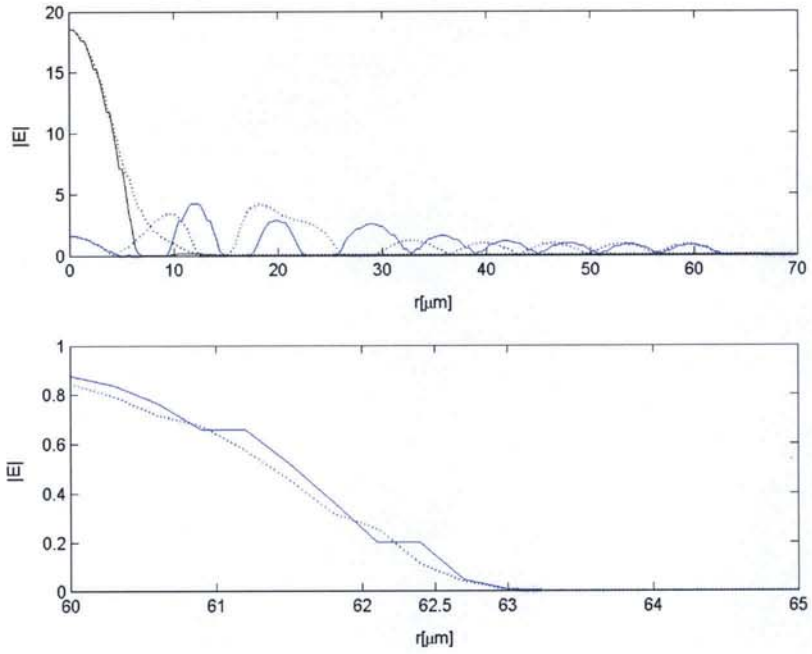

Figure 2.23: X (solid lines) and y (dashed lines) profiles of the core mode (black) and the main resonant mode (blue) of the 500μm LPG in the ESM PCF when it is in the air. Figure below shows mode profiles zoomed in around the outer cladding - air interface.

However, it is valid only for the external indices close to 1 where the wavelength shift is very small. Numerical modelling of the sensitivity to the external refractive index is straightforward as it is sufficient to set the refractive index of the ring simulating the surrounding material to the appropriate value. Change in the external index does not cause a change in the grating period and the wavelength shift is simply obtained from the shift of the grating characteristic along $\Lambda_B = \Lambda$.

Fig. 2.24 shows the dependence of the beat length required by the phase matching condition on the external refractive index and Fig. 2.25 the wavelength shift found from the intersection of these curves and the line $\Lambda = 500\mu$m.

Simulation gave the correct sign of the wavelength shift but the values were many times larger than those obtained in the experiment in which the maximal wavelength shift of the attenuation band at 1402 nm of the 1000μm LPG in the ESM PCF was only 0.8 ± 0.1 nm [23], which means that the light propagating through the silica cladding in the simulated fibre 'feels' the surrounding index much more than the light in the real fibre. The reason may lie in neglecting both the material losses in silica and the losses on the holes that would cause

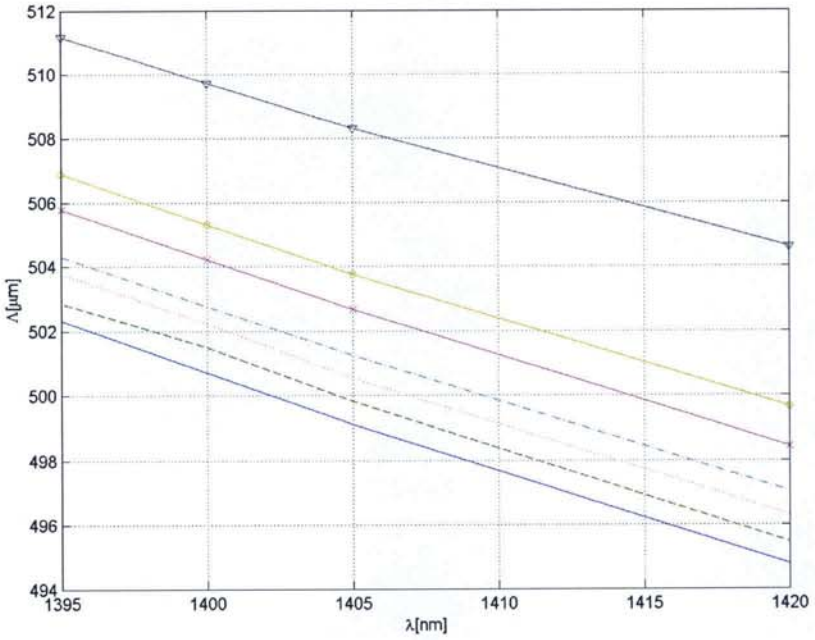

Figure 2.24: Beat length of the main resonant mode of the 500μm LPG in the ESM PCF for different values of the external refractive index: 1.0 (solid line), 1.2 (dashed), 1.3 (dotted), 1.35 (dash-dot), 1.4 ($\times$), 1.42 ($\circ$), 1.44(∇).

attenuation of the light reaching the outer cladding, as well as the change in the mode profile that affects the mode effective index and therefore the total internal reflection condition at the outer cladding - air interface. Indeed, the transmission spectrum of the 500μm LPG in ESM PCF coincidentally overlapped with the attenuation spectrum of this fibre, [39], the maxima of which are mainly caused by the OH^--absorption in silica, [79]. This was not the case with the LPG in LMA which exhibited much higher sensitivity to the external refractive index with the maximal wavelength shift of 30.8 nm. However, as the sensitivity is mode dependent, it is difficult to extract the reason of the biggest loss as can be seen on the example of the 1239 nm attenuation band of the LPG in the ESM PCF. The maximal wavelength shift of this attenuation band was considerably bigger than that of the band at 1402 nm which may come from the smaller loss in the bulk silica cladding at this wavelength but also from the mode profile according to which this mode interacts with the surrounding material more than the mode resonant at 1402 nm, Figs. 2.8 c), g).

In conclusion, the studied LPGs were sensitive to the external refractive index so that they exhibited the red wavelength shift when the external index was increased. Our model

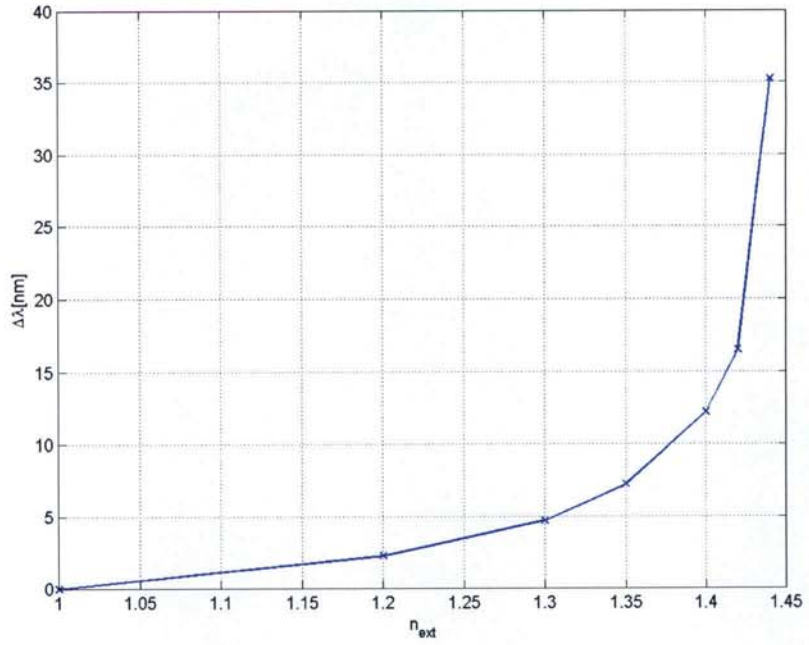

Figure 2.25: Calculated shift in the resonant wavelength of the 500μm LPG in ESM PCF due to the change in the external refractive index.

provides a qualitative explanation of this trend. The disagreement in the measured and numerically calculated values is attributed to neglecting the losses in the fibre.

This concludes the section on the grating sensitivity in which we have used the previously described model to explain and evaluate responses of the LPGs in PCFs to strain, temperature and the external refractive index. The model supports the experimental result that the LPGs were insensitive to temperature while sensitive to other parameters. The calculated sensitivity to strain is in good agreement to the measured value, while the calculated sensitivity to the external refractive index exceeds the value obtained in experiments. Several improvements of the model are possible such as taking into account the inhomogeneous distribution of strain in PCF, dispersion of the coefficients used in calculations, material losses in silica and the losses due to the refraction at the air holes, as well as iterating the solution if necessary.

2.5 Impact of Variations in the Geometry of PCF on the Properties of the LPG

2.5.1 Modal Properties of PCFs with Different Geometries

The finiteness of the crystal limits the performance of the PCF. However, the smaller is the number of holes, the bigger is the coupling between the core and the bulk cladding modes. If the geometry of the fibre allows such coupling, it may be possible to produce LPGs that are insensitive to temperature and very sensitive to the external refractive index.

2.5.2 Impact of the Imperfections of PCFs on the LPGs Fabricated in Them

The symmetry, regardless of how boring or beautiful it is, may be useful even if it is broken. Asymmetry of the fibre causes splitting of the attenuation bands into two that correspond to different polarisations of the input light. Asymmetry is usually the consequence of the irregularities in the fibre structure, but it may also be induced on purpose as in [80] for the fabrication of directional bending sensors. Two types of imperfection most commonly found in PCFs are small random variations in the diameters of the holes and larger defects preserved along the fibre. The former have been studied extensively [81–83], because they are more difficult to eliminate from the fabrication process. The latter proved useful in the fabrication of directional bending sensors [23].

In order to estimate the birefringence induced by random imperfections, we randomised the diameters of the holes by inserting a random variation with the normal (gaussian) distribution and varied the standard deviation by setting it to 1%, 2.5%, 5% and 10%. The effective refractive indices were calculated ten times for each deviation for the linearly polarised core modes from the classes 3 and 4. The results are shown in Fig. 2.26.

The numerical birefringence was of the order of 10^{-7}. Changes in the radii of holes of up to 10% caused the birefringence with the average of approximately 5×10^{-6} and the deviation of the same order of magnitude in accordance with the results reported in [84]. Very similar results were obtained when the separation between holes was randomly varied.

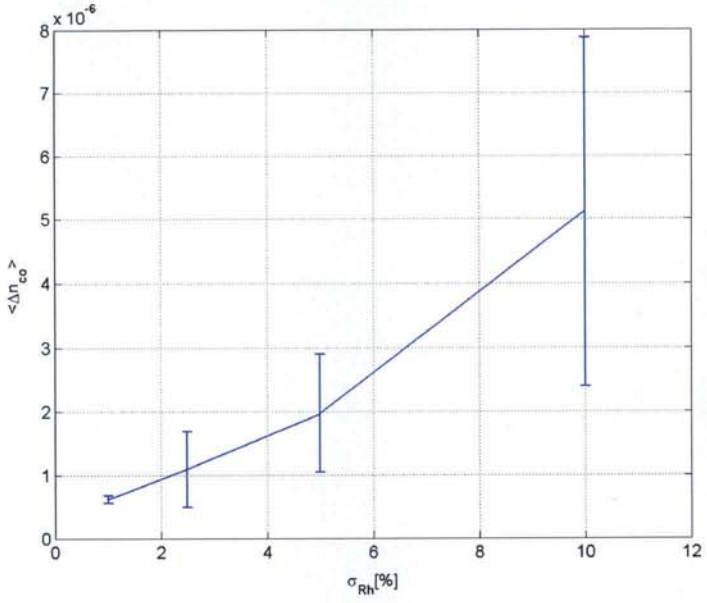

Figure 2.26: Average birefringence induced in the ESM PCF due to variations in the radii of holes. Error bars represent the standard deviation of the birefringence.

In order to study the impact of irregularities on LPGs, it is necessary to consider changes in both the core and the cladding modes. Substantial changes in the cladding mode propagating through the photonic crystal could be expected due to its close contact with the disturbed region. The analysis was repeated for the cladding modes for the same kind and range of irregularity and found that the resonant cladding mode underwent much bigger changes than the core mode. While the birefringence of the core mode for the standard deviation of the hole radii $\sigma_{R_h} = 1\%$ was 10^{-6}, birefringence of the cladding mode was an order of magnitude bigger. Already for $\sigma_{R_h} = 2.5\%$ the resonant cladding mode could not always be identified because of the significant distortion of the linear polarisation and for the bigger deviations of the hole radius it was unrecognizable. Modes that are not linearly polarised undergo smaller changes in the field profile and the modes in the outer cladding barely feel the irregularities. Examples of the distorted modes are shown in Fig. 2.27.

Due to the described changes in the mode profiles and the propagation constants, irregularities can cause changes in the position and magnitude of the attenuation bands of the LPG compared to those of the LPG in the regular fibre. The effective refractive index difference that enters the phase-matching condition is mostly due to the change in the index of the resonant cladding mode. For $\sigma_{R_h} \leq 2.5\%$ the mean birefringence of the dif-

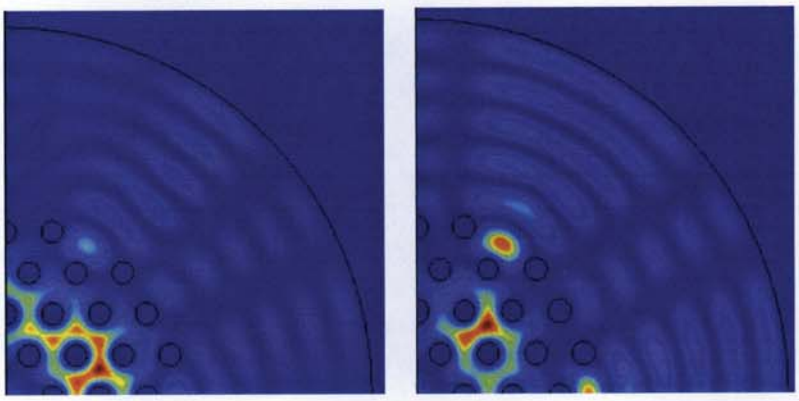

Figure 2.27: Impact of random variations in the radii of the holes on the profile of the resonant mode. The distribution is gaussian with the standard deviation of: a)1% and b)10%.

ference between the effective indices of the core and the resonant cladding mode was less then $< \delta n_x - \delta n_y >= 4 \cdot 10^{-6}$ causing the maximal shift in resonant wavelength of 2 nm. This change is small and tolerable. Bigger deviations induce changes in the profiles of the resonant modes along the fibre which significantly affect the coupling. This manifests in the spectrum as reduction in magnitude and broadening of the attenuation bands.

In conclusion, small random variations in the radii of the holes of PCF cause birefringence of both core and cladding modes. The effect of the variations with the standard deviations of a few percent is small and does not significantly affect the grating, whereas the bigger deviations introduce big changes in the resonant cladding modes and severely deteriorate the grating performance.

2.6 Multiple-Period Resonances

2.6.1 Experimental Evidence and Terminology

The negative slope of the grating characteristic is not the unique property of the LPGs in PCFs. Over the longer wavelength range the characteristic of LPG in either step-index fibre or PCF can change the monotonicity, exhibiting theoretically infinite sensitivity at the stationary point, [50, 51]. Hence, the following discussion is of significance for LPGs in any kind of fibre.

When the index profile of the grating along z cannot be described by the simple sinusoid

the higher order harmonics must be taken into account. A resonant wavelength of the N^{th} order grating satisfies the phase matching condition $\lambda = \delta n \Lambda / N$. When the grating characteristic has positive slope higher order gratings have shorter resonant wavelengths. It was predicted and experimentally proven that the N^{th} order grating with the fundamental period $N\Lambda$ will have the same resonant wavelength as the 1^{st} order grating with the period Λ, [50]. The situation changes when the slope of the characteristic is negative so that higher order gratings have longer resonant wavelengths due to their shorter effective periods. Both cases are shown in Fig. 2.28. In other words, the waveguide dispersion of the fibre is such that the higher the spatial frequency of the grating, the lower its resonant frequency.

The consequences are best seen by examining the gratings with the multiple periods.

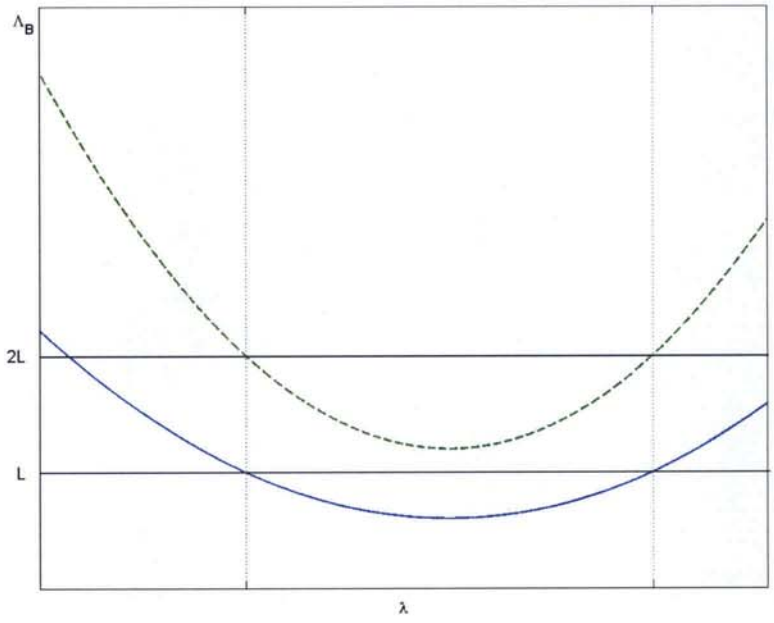

Figure 2.28: Beat length versus wavelength for the first order (solid line) and the second order (dashed line) resonances of LPG in PCF.

Therefore a grating of 1000μm period was fabricated subsequently and compared to the 500μm grating, Fig. 2.29.

Overlap of both resonant peaks is apparent, the small shift being most probably caused by the application of another splicer (with the same specifications as the previous). The difference between the resonant wavelengths of 6.5 nm can be used as an estimate of the repeatability of the method, and therefore as a rule of thumb for the estimation of the accuracy

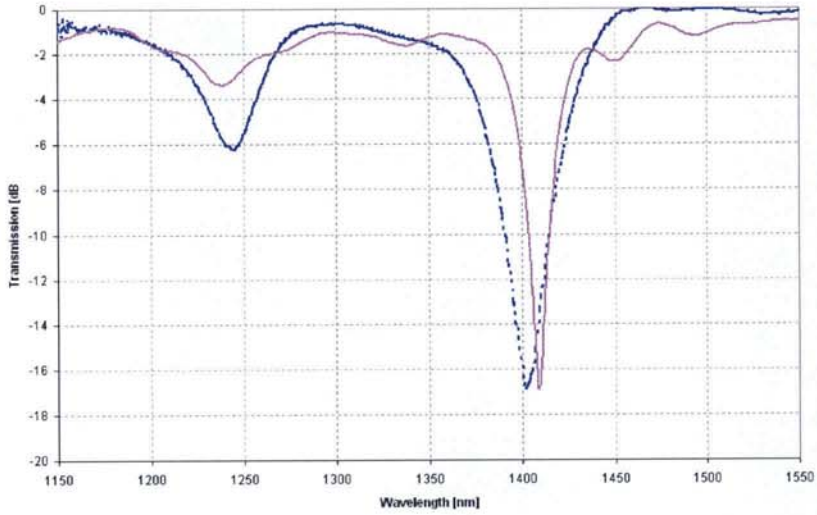

Figure 2.29: Spectra of the 500μm and the 1000μm LPGs in the ESM PCF. The rest of the recorded spectrum is not shown as it does not contain any resonances.

required in the numerical simulations.

Due to the spectral range of OSA only the part of the spectrum 800 nm - 1700 nm could be checked. According to Fig. 2.28 the resonance of the 1000μm grating is of the second order and the first order resonance can be expected at the wavelengths below 800 nm. The mentioned experimental limitation can be overcome by fabricating gratings of the different periods, so that a few resonances would fit into the measurable range.

Experimental results on this topic are rare. It was reported in [49] that the grating of the period 620 nm had resonances at $\lambda = \delta n \Lambda$ and $\lambda = \delta n 2\Lambda$. The previous considerations and this result put forward a "disputable question": What happens if the resonant modes at some wavelength cannot accumulate enough phase difference over a single grating period but require multiple grating periods? For example, let the two modes be resonant at some wavelength with the beat length equal to the single grating period. At some shorter wavelength the difference between their effective refractive indices may be increased so much that the required beat length equals multiple grating periods, which may be the case reported in [49]. Descriptively, two modes would interact as if they 'see' the multiple period grating.

The generalised phase matching condition that allows for this to happen is

$$\beta_{co} - \beta_{cl} = \frac{2\pi N}{LM} \tag{2.12}$$

where N and M are integers. In the next section the mathematical model is developed which can explain this phenomenon.

2.6.2 Theory of the Multiple-Period Resonances

Standard coupled mode theory applied to fibre gratings and as described in Section 1.5.1 does not provide an explanation of multiple-period resonances. This is due to its inherent assumption that the fundamental frequency of the system equals one grating period. However, when the beat period between the resonant modes is significantly smaller than the grating period the beat frequency becomes fundamental and a resonance occurs only if the generalised phase-matching condition (2.12) is satisfied.

The idea behind the generalisation of the coupled mode theory lies in the harmonic expansion of the slowly varying amplitudes of the resonant modes with the fundamental frequency $\Delta\beta$. The expansions of the core and cladding mode amplitudes are given by the expressions (2.13) and (2.14). Notation follows that from Sec. 1.5.1 and A_m^{co} and A_m^{cl} are the amplitudes of the m^{th} harmonics of the core and cladding mode amplitudes.

$$A^{co}(z) = \sum A_m^{co}(z) e^{im\Delta\beta z} \tag{2.13}$$

$$A^{cl}(z) = \sum A_m^{cl}(z) e^{im\Delta\beta z} \tag{2.14}$$

Substitution of these expansions into the basic coupled mode equations for the copropagational coupling (1.8) and (1.9) followed by the shift in indices results in the infinite set of equations for each mode component as given by Eqns. 2.15 and 2.16 for the m^{th} core and cladding mode component respectively.

$$\frac{dA_m^{co}}{dz} = i(\kappa_{co} - m\Delta\beta)A_m^{co} + i\frac{\kappa_{co}\sigma}{2}(A_{m+M}^{co} + A_{m-M}^{co}) + i\kappa A_{m-1}^{cl} + i\frac{\kappa\sigma}{2}(A_{m+M-1}^{cl} + A_{m-M-1}^{cl}) \tag{2.15}$$

$$\frac{dA_m^{cl}}{dz} = i(\kappa_{cl} - m\Delta\beta)A_m^{cl} + i\frac{\kappa_{cl}\sigma}{2}(A_{m+M}^{cl} + A_{m-M}^{cl}) + i\kappa A_{m-1}^{co} + i\frac{\kappa\sigma}{2}(A_{m+M+1}^{co} + A_{m-M+1}^{co}) \tag{2.16}$$

Here $\kappa_{co}, \kappa_{cl}, \kappa$ are core to core, cladding to cladding, and core to cladding coupling constants given by

$$\kappa_{co,cl} = \frac{\omega n \varepsilon_0}{2} \iint \overline{\Delta n}(\vec{r}) \vec{E}_{co,cl}(\vec{r}) \vec{E}^*_{co,cl}(\vec{r}) d\vec{r} \tag{2.17}$$

$$\kappa = \frac{\omega n \varepsilon_0}{2} \iint \overline{\Delta n}(\vec{r}) \vec{E}_{co}(\vec{r}) \vec{E}^*_{cl}(\vec{r}) d\vec{r} \tag{2.18}$$

where the integration domain is the part of the fibre cross section with the average refractive index change $\overline{\Delta n}$. The practical initial condition that only the dc component of the core mode is present at the input of the grating is given by $A^{co}_0(z) = 1, A^{co}_{m\neq 1}(0) = 0, A^{cl}_m(0) = 0$. From equations (2.15) and (2.16) it can be seen that A^{co}_0 couples to only five mode components: $A^{co}_{\pm M}, A^{cl}_{-1}, A^{cl}_{\pm M-1}$. These mode components are also coupled back to A^{co}_0. Since the system of equations (2.15) and (2.16) is cascaded, all mode components will be excited. However, each stage introduces attenuation and in the first approximation only the directly coupled mode components are significant. Under the given initial conditions the whole system reduces to the system of six equations:

$$\frac{dA^{co}_0}{dz} = i\kappa_{co} A^{co}_0 + i\frac{\kappa_{co}\sigma}{2}(A^{co}_M + A^{co}_{-M}) + i\kappa A^{cl}_{-1} + i\frac{\kappa\sigma}{2}(A^{cl}_{M-1} + A^{cl}_{-M-1}) \tag{2.19}$$

$$\frac{dA^{co}_{\pm M}}{dz} = i(\kappa_{co} \mp M\Delta\beta)A^{co}_{\pm M} + i\frac{\kappa_{co}\sigma}{2}A^{co}_0 + i\kappa A^{cl}_{\pm M-1} + i\frac{\kappa\sigma}{2}A^{cl}_{-1} \tag{2.20}$$

$$\frac{dA^{cl}_{-1}}{dz} = i(\kappa_{cl} + \Delta\beta)A^{cl}_{-1} + i\frac{\kappa_{cl}\sigma}{2}(A^{cl}_{M-1} + A^{cl}_{-M-1}) + i\kappa A^{co}_0 + i\frac{\kappa\sigma}{2}(A^{co}_M + A^{co}_{-M}) \tag{2.21}$$

$$\frac{dA^{cl}_{\pm M-1}}{dz} = i(\kappa_{cl} \pm -(\pm M - 1)\Delta\beta)A^{cl}_{\pm M-1} + i\kappa A^{co}_{\pm M} + i\frac{\kappa\sigma}{2}A^{co}_0 \tag{2.22}$$

For LPG inscribed in the core of the SMF the generalised system must reduce to the Erdogan's equations (1.8) and (1.9). Indeed, in this case the coupling coefficients are related by inequality $\kappa_{co} >> \kappa >> \kappa cl$ and for a single period resonance, $M = 1$, all terms apart from A^{co}_0 and A^{cl}_{-1} are averaged out. The remaining terms represent the mode amplitudes and the system is reduced to the pair of the standard coupled mode equations.

Double period resonances from [49] can be described by equations (2.19-2.22) with $M = 2$.

The convergence of the solutions was tested by increasing the number of harmonics in the mode expansion which was not trivial because adding of one higher harmonic means increasing the number of equations by two.

In conclusion, the mathematical model has been proposed that can explain multiple-period resonances experimentally observed in LPGs in PCFs [49] and defined here. It is reducible to the standard coupled mode equations. Since the basis of the model is the harmonic expansion of the slowly varying mode amplitudes, the accuracy can be adjusted by varying the number of the terms included. The general phase-matching condition that can be applied to any LPG in any fibre independently of the grating characteristic has been suggested.

2.7 Conclusions

The long period gratings fabricated in the photonic crystal fibres with bulk cladding by the electric arc were studied in the frame of the coupled mode theory. For that purpose, the comprehensive analysis of the eigenmodes of the PCF was performed and the whole gallery of the core and cladding modes found, the latter being either in the photonic crystal or in the bulk cladding. Precise calculation of the propagation constants and mode field profiles was achieved by the reduction of the simulated part of PCF to the irreducible zones defined by the symmetry of the fibre. This was crucial for the detection of the resonant modes of the LPG which turned out to be quasi LP modes. Both numerical and semi-analytical models were used to calculate the LPG sensitivity to strain, temperature and the external refractive index. It was confirmed that the grating is almost insensitive to temperature, whereas it is sensitive to other parameters which is the unique property extremely useful for the elimination of the cross-sensitivity. The method for the nondestructive index profiling of the LPGs was suggested which should lead to a better understanding of the changes induced in the PCF by the electric arc. As these changes are both in geometry and the refractive index of silica, the model is generic for LPGs fabricated by any method apart from those that reshape the outer cladding of the fibre. The shortcomings of the presented models are correctable as have been suggested in each particular case. Many of them are due to the lack of the systematic experimental data which is understandable considering the novelty of the studied gratings. The impact that the imperfections introduced in a PCF during the fabrication have on an LPG in that fibre was examined and it was shown that LPGs can be fabricated in the

ESM-like fibres if the standard deviation of the normal variation in the diameters of holes is smaller than 3%.

To summarise, we have established a general model of the LPGs in PCFs capable of explaining their spectral properties and sensitivity to the external parameters and which can be used for the index profiling of the LPGs based on the spectra recorded during their growth.

Chapter 3

Interaction of the Femtosecond Laser With Materials: Experiments, Physics, Modelling

3.1 Introduction

The development of the solid state ultrashort pulse lasers and the chirp amplification technique [85, 86] enabled the commercialisation of the robust high-power femtosecond table top laser systems, thereby removing the major practical objections to the femtosecond micromachining: accessibility and the cost of the fabrication system. By making use of the tight focusing and the self-focusing of the pulse, well localised and long lasting refractive index change have been produced. The field has developed rapidly over the last several years from the basic testing of the impact the femtosecond laser pulses had on material to the manufacturing of various optoelectronic devices, e.g. wavelength multiplexers [87], optical memory [88], waveguides [89], fibre gratings [15, 90]. Although there is still a lot of space for research on the device side, the essential improvement can be made only after the processes involved in femtosecond laser – material interaction have been understood. This chapter is the result of experimental and theoretical efforts made with the aim to understand and quantify the processes leading to the refractive index change. It describes investigation of the interaction of different materials with single femtosecond pulses of different powers

and under different focusing conditions.

There are two typical set-ups related to the focusing geometry. If the goal is to produce the longest possible filament then loose focusing and small spot size are required [91, 92]. However in the microfabrication context the opposite goal is usually desirable. The focused spot is required to be as small as possible in all three dimensions and the absorbed energy is needed to be within the narrow window between the thresholds of inscription and damage. In regard to modelling, this is a difficult numerical task because of the huge difference in spatial and temporal scales of the incident laser beam and fine features of light and plasma patterns in the vicinity of the focal point. The adaptive mesh refinement allows for accurate treatment of the multiscale evolution which results in stationary distribution of plasma. The mechanisms of eventual plasma recombination and subsequent relaxation of the medium are extremely complex. For example, the latter can be described as a sophisticated 3D thermo-elasto-plastic processes [93]. The purpose of the present work is to find an accurate spatial distribution of plasma needed for such or similar subsequent analysis.

The well confined changes in the material induced by a single femtosecond pulse are practically achieved either by the tight linear focusing by a microscope objective or by a loose linear focusing by a lens but in the self focusing regime. We examine the following situations: (1) focusing by a microscope objective into the pure silica, (2) focusing into the medium with the high Kerr nonlinearity by a) the lens with the long focal distance and b) the microscope objective. The case 1) corresponds to the usual experimental set-up, hence we simulate the focusing by the commonly used dry objectives that are corrected to abberations by the cover slip. The other two cases are more of a theoretical value and they demonstrate a complex pulse propagation and interaction with plasma in a theoretical medium. The nonlinear medium was chosen because it enhances self-focusing and indeed, the results of simulations suggests a possibility of creating subwavelength plasma clouds and therefore the subwavelength refractive index changes in such a medium. We also assume the index matched focusing which can be realised in practise by using the oil immersion between the lens/objective and the sample.

The experimental study of the inscription by single laser pulses is presented first and the results are qualitatively explained by the physical model. The numerical model that was used to simulate the above mentioned situations is described and the possible applications

of different scenarios discussed. In the final part of the chapter near the surface inscription as well as the inscription in different materials are demonstrated and our results compared to those of the other groups. The last section features the results of the 2-year study of the refractive index change induced by the single femtosecond laser pulses.

3.2 Experimental Method

The general set-up for the femtosecond inscription is shown in Fig. 3.1. The source of femtosecond pulses was a Kerr mode locked Tsunami Ti:sapphire laser with the output at the wavelength 800nm. The pulse duration was 150fs and the peak power 10GW. The system had two modes of operation: the single pulse and the pulse train with the slow repetition rate of 1kHz.

At the output of the amplifier a part of the beam was sent to an autocorrelator to measure

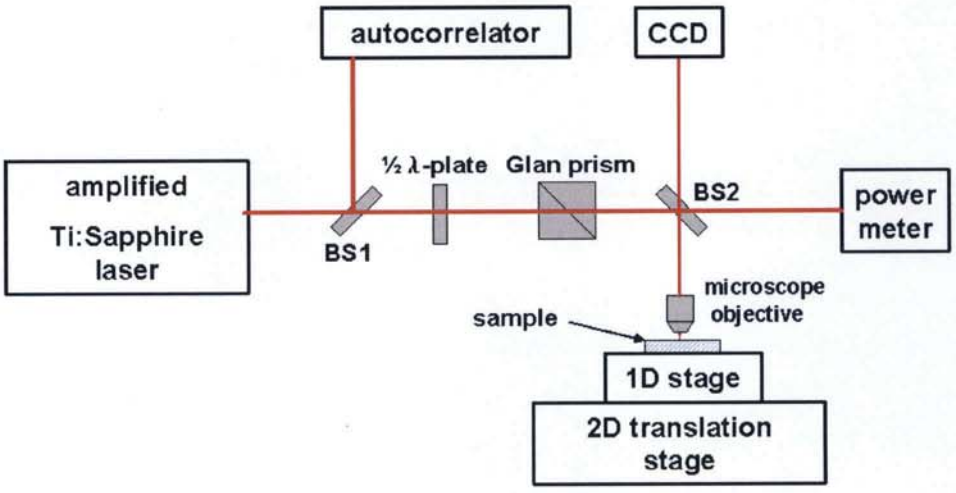

Figure 3.1: Set-up for the femtosecond inscription.

the pulse duration. The half wavelength plate and the Glan prism served as the polarisers to control the pulse power which was measured by the thermal powermeter. The response time of the thermometer was long and the accuracy not better than 0.1mW. Microscope objectives with magnifications x20 and x40 and respective numerical apertures 0.45 and 0.65 were used to focus the pulse tightly on the sample. The sample was mounted on a computer controlled

Aerotech 2D translation stage extended to 3D by a mechanical translation stage. The alignment of the system was achieved by aligning the low power beam of the argon laser with its reflection from the mirror placed instead of the sample. Then the sample was mounted and the spot size of the unamplified Ti:Sapphire beam on its surface measured by a CCD camera to be used as a reference for the alignment of the sample. The depth of focus was controlled by the manual 1D translation stage and by monitoring the change in respect to the reference spot size. Another CCD camera positioned perpendicularly to the plane of Fig. 3.1 was used to monitor the inscription.

Due to the small size and accessibility of the in-bulk modifications induced by individual laser pulses their examination required elaborate microscopic techniques. The resolution of the standard optical microscopic techniques such as bright or dark field are limited by the wavelength of the light and is not sufficient for the tiny structures inscribed by low powers. Differential interference contrast (DIC) and the phase contrast imaging improve the image greatly and they were used in our experiments. Advanced techniques such as the atomic force microscopy and the surface electron microscopy can give information on the morphology of the material modification, but require the preprocessing of the modified sample such as coating by metallic film, the precise cutting or the chemical etching, respectively. Structural modifications are best examined by the Raman spectroscopy. As the idea behind the work presented here was modelling of the optical devices fabricated by the femtosecond laser, we were mainly interested in the profile of the index change which we were able to measure by the quantitative phase microscopy.

The samples were analysed by the phase microscope Axioscope (Inc. Carl Zeiss) and the commercial software for the quantitative phase microscopy QPm (IATIA). QPm is a general method for visualising and quantifying the phase profile of the sample. The image taken with the sample in the focus gives information on both phase and amplitude, the latter needed as a reference when the illumination of the sample is not uniform. Another two images are taken by slightly defocusing the sample in each direction. They are be related by the transport of intensity equation which expresses the gradient of intensity as a function of the change in phase [94]. By substraction of the obtained intensity images and integration using this equation the phase profile of the sample can be retrieved [95], [94] and subsequently its index profile. The major drawback of the technique was that the spatial resolution did not allow

for the study of the subwavelength structures.

In order to avoid the modification of the material at the postfabrication stage, e.g. by chemical etching, the samples were prepared by cutting and polishing to the roughness of 0.1μm. Glass cutting is an ancient technique that utilises crystalline structure of the glass. The slide is first gently scratched by the cutting wheel and the water is applied to the scratch to assist breaking. Simple break gives a cut with the roughness of several microns so that the polishing to the submicrometre roughness was necessary in order to prevent scattering in the image field. It was done manually by applying the polishing paper of smaller roughness in each step. The finest resolution was 100 nm but any below 500 nm gave acceptable result.

3.3 Characteristic Inscription Regimes

Traces of the individual laser pulses in glass were studied systematically in order to determine how their optical properties depend on the pulse energy. There were four major experimental challenges:

1. measuring the dimensions of the structures
2. measuring the magnitude of the refractive index change
3. determining the onset of the index change in the propagation direction
4. devising the inscription geometry that allows all measurements from 1-3 to be done for the same structure

The first pair of tasks must be done in the given order because the dimensions are input to the calculation of the refractive index change. The combination of the two gives the index profile of the structure.

In order to meet the last requirement, the rows of equally spaced structures were inscribed with the same power each, Fig. 3.2. This was done by exposing the fused silica sample to the train of single laser pulses with the frequency 1kHz while translating it in the direction perpendicular to the beam with the speed 20mm/s. This speed ensured that the structures do

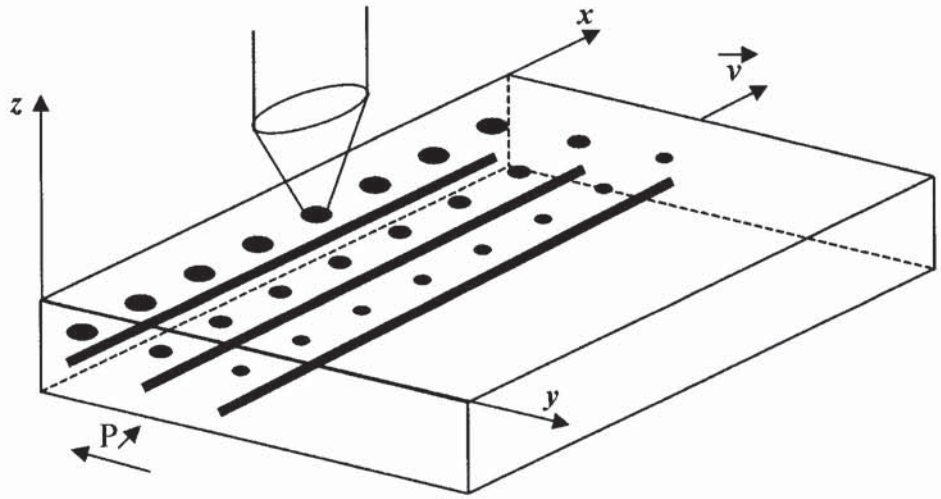

Figure 3.2: Geometry of the set-up used to investigate inscription by single femtosecond pulses.

not overlap and that the distance between them is small enough to make the cross section of the structures written by all the powers visible by a single cut. The reference lines needed by 3) were written with the smaller speed and the power high enough to make them observable by the microscope. They served as markers for the cuts and as zero lines for the measurement of the onset of the index change. The diameter of the written feature D was extracted from the images recorded by microscope and the dimension in the propagation direction of the beam L was measured after the sample had been cut along y-axis and polished. The results are presented in Fig. 3.3

Figure 3.4 shows the three typical geometries of the structure written by the pulses of different energies. As we kept the pulsewidth constant, the terms pulse energy and power are used interchangeably. At the moderate power below the critical power of self-focusing the structure was nearly spherical and became ellipsoidal at slightly higher powers. In both cases it was very well confined to the focal region. At the powers above P_{cr} the pulse focused by the objective with the magnification x20 (NA-0.45) produced the structure with a distinctive ellipsoidal index change near the focus and a small index change that resembles an imprint of the beam before the focus, Fig. 3.4b). When the focusing is tighter (x40, NA-0.65) the structure is suspected to be a result of the microexplosion in the glass and has therefore ellipsoidal or spherical shape, Fig. 3.4c). When the pulse energy exceeds the material damage threshold, the pulse causes fracture of the material that results in irregular cracks expanding

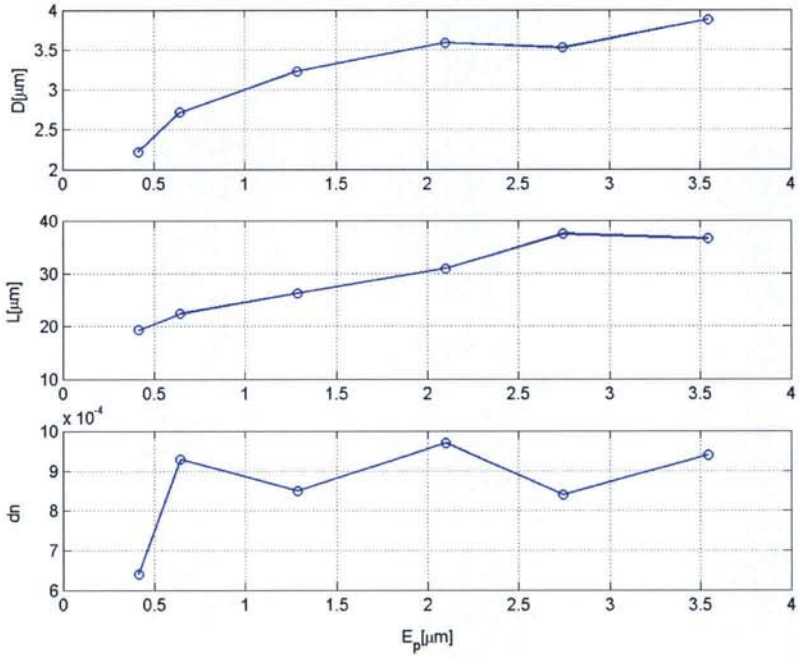

Figure 3.3: Diameter, length and magnitude of the refractive index change induced by a single femtosecond laser pulse versus pulse energy.

from the focal region. In order to avoid the damage of the optical elements in the set-up, the energies close and above the damage threshold of glass have not been applied. For the illustration purposes we show the damage in polymer which has lower damage threshold than glass (polymer was supplied by K. Kalli).

The phase profiles $\Delta\Phi(r)$ were determined by QPm. Assuming the uniform average index change Δn, which is justified for the displacements from the focus by 1μm, a good estimate can be obtained using the equation for the linear phase shift $\Delta n = \Delta\Phi/L$. The refractive index profiles for two typical cases are shown in Fig. 3.5. A low energy pulse creates a smooth and positive index change, see examples in Figs. 3.5a) and 3.4a), while a higher energy pulse creates a rarefied region with the reduced refractive index that is surrounded with a densified region with the increased index, Figs. 3.5b), 3.4c). Dependence of the refractive index on density is explained in Sec. 3.4.1 and used in the from of Lorenz-Lorentz relation in Sec. 4.2. If the pulse is focused by a high NA objective the central region can be totally depleted of material and turned into void of up to several hundreds of nanometers in diameter, [96, 97].

With an increase in the pulse energy the onset of the index change is shifted towards the

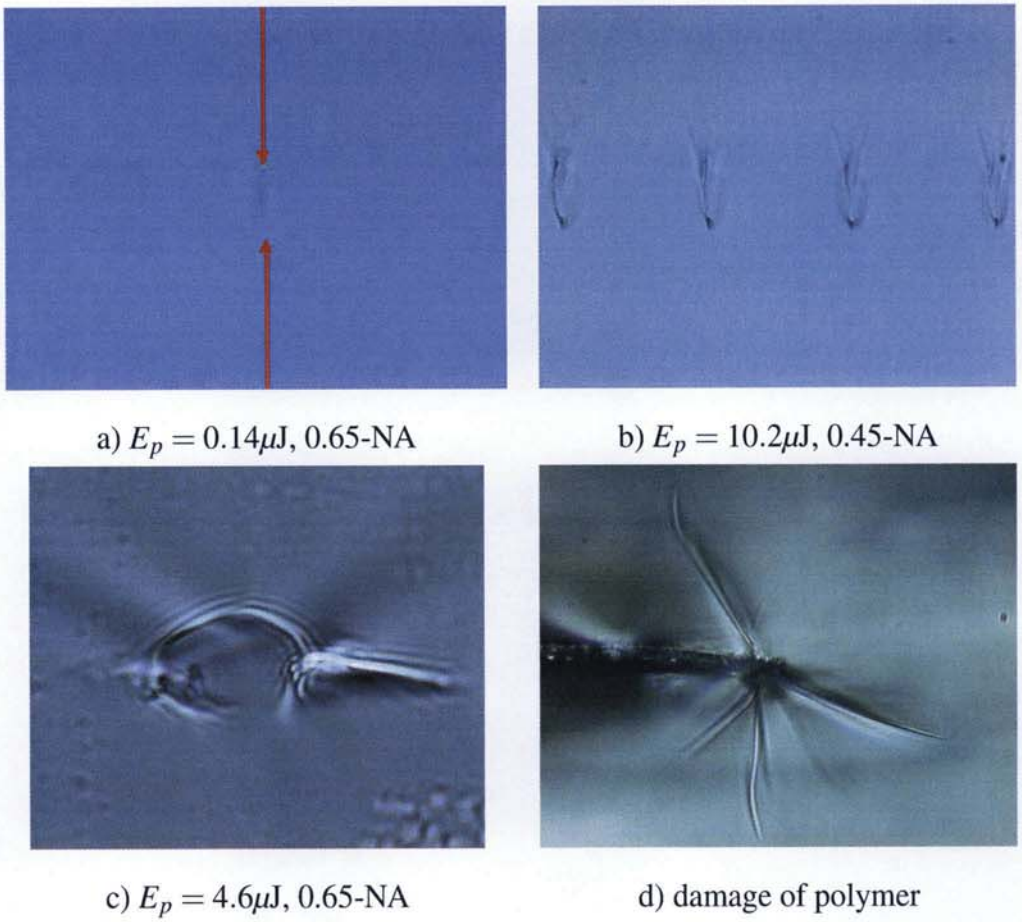

a) $E_p = 0.14\mu$J, 0.65-NA

b) $E_p = 10.2\mu$J, 0.45-NA

c) $E_p = 4.6\mu$J, 0.65-NA

d) damage of polymer

Figure 3.4: Typical shapes of the index change induced by the irradiation by the single femtosecond pulse.

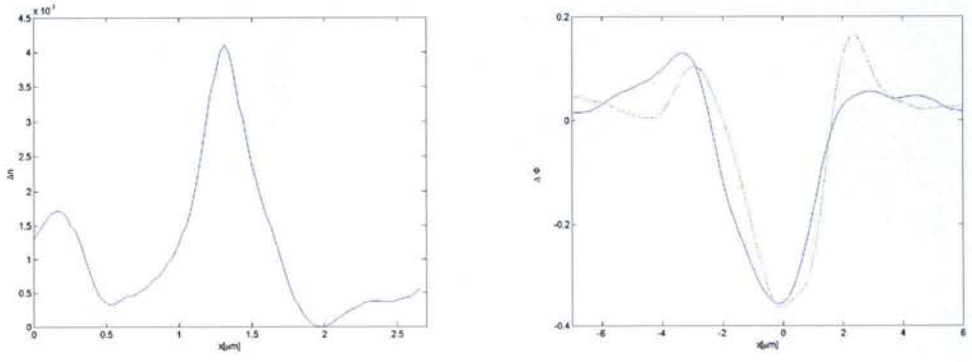

a)

b)

Figure 3.5: a) Characteristic refractive index profile obtained by the single femtosecond pulse with $E_p \approx 0.46\mu$J. b) Phase profile of the structure written by the single pulse with $E_p \approx 2\mu$J.

laser. The maximal shift for the pulse energy range of 0.7μJ was 3μm. This is a consequence of two effects: (*i*) the more powerful pulse reaches the threshold intensity further from the

focus and (*ii*) experiences stronger self-focusing which brings focus closer to the source. The similar result was obtained for the multiple-pulse inscription by Sudrie et al. [98] who measured the shift of the focal point due to the self-focusing.

In conclusion, the major regimes of the interaction of the single femtosecond pulse with glass have been observed and characterised: the low energy regime that results in a smooth index change suitable for fabrication of waveguides, couplers, multiplexers, and the high energy regime that results in the voids suitable for the fabrication of gratings, photonic crystals, optical memories. As the operating principles and spectral properties of these devices are based upon their index profiles, understanding the mechanisms of index change is necessary for their full characterization and exploitation. For example, thermal annealing of the grating relies on knowing the distribution of stresses, the erasure of data from the optical memory can be achieved only if the mechanism of writing is understood, the wavelengths selected by the multiplexer depend on the refractive indices of the inscribed waveguides, etc. Our present and future theoretical and experimental work aim in that direction.

3.4 Model of the Ultrashort Laser Pulse Propagation and Interaction with Material

Nonlinear propagation of the nano- and picosecond laser pulses and their interaction with material have been studied extensively since the invention of these lasers, [99–102]. The studies of the interaction of the femtosecond pulses gained on importance only after the mentioned advancements in the laser sources were made. On one hand, this led to the fundamental applications such as supercontinuum generation and optical clocks [103] and on the other, to applications in micromachining. It was first reported and explained by Du et al. [104] that the breakdown threshold fluence in the femtosecond regime decreases with the pulse duration $F_{th} \sim \tau_p^{-1}$, whereas for the pulses longer than a few picoseconds the threshold fluence grows with the pulse duration $F_{th} \sim \tau_p^{1/2}$. Namely, as the multiphoton absorption (MPA) is a dominant mechanism of ionisation in the fs regime, the threshold is determined by intensity $I = \frac{dF}{d\tau_p}$ as opposed to fluence, thus the shorter the pulse, the greater the fluence needed to initiate the breakdown. Smaller duration of the interaction, better spatial

confinement and higher intensity of the femtosecond pulse cause longer phenomena, such as the thermal diffusion and recombination of electrons, to become negligible during the pulse propagation through the material and bring about the multiphoton ionisation as the predominant mechanism of the generation of plasma. In this section we first describe a physical model of the interaction of the single femtosecond pulse with dielectric and analyse the time scales of the processes involved. Then we introduce an existing mathematical model and describe its application to the study of the femtosecond micromachining. Due to the self focusing and tight focusing the spatial scale in the radial direction varies over a few orders of magnitude. The last part of the section explains how this problem was solved using the adaptive mesh refinement. Results of the simulations are described in Sections 3.6.1 and 3.6.2.

3.4.1 Physical model

Propagation of the intense femtosecond pulse through a dielectric causes the modification of the dielectric which in turn affects the propagation of the pulse. Therefore, the laser pulse and the material form a coupled system.

The electromagnetic wave propagating through a lossless homogeneous medium that is translationally invariant in the direction of propagation can be described as a plain wave in that direction. The only change that happens to the beam is a change in phase due to the diffraction. Another simplification is to consider the wave monochromatic. This simplified picture does not hold for the intense ultrashort pulses unless the medium is an absolute vacuum. As a consequence of the interaction with the medium, spatial and temporal profiles of the pulse can dramatically change.

The interaction can be resonant and non-resonant. The resonant interaction is a result of the polarisation induced by the redistribution of the electrons in the outer valence bands due to the external electric field or by the polarisability of the whole molecule. As the collective response of the electrons is too slow to follow the oscillations of the alternating electric field at the optical frequencies $10^{15}s^{-1}$, it is the dc component of the intensity of light $I \sim |E|^2$ that affects the electron cloud instantaneously, which is described by the Drude equation [105]. All processes involved in the resonant coupling occur at a single frequency. When the photons not only polarise molecules, but also excite their resonant modes there is a shift in the

resonant frequency and the coupling becomes non-resonant. Most common examples are Raman and Brillouin scattering in which the vibrational modes of the molecules and the acoustic phonons are excited respectively. Due to the inertia of the lattice these processes are non-instantaneous. However, the delay is usually several fs and in many applications can be neglected.

The response of the material to an external field depends on its strength and the structure of the material. At moderate field intensities, materials with inversion symmetry have a linear response, while the response of other materials is nonlinear. In a simple model in [33] the restoring force caused by the asymmetry of the crystal, causes the nonlinear displacement of the electrons, and therefore the nonlinear polarisation. This is quantified by the electric susceptibility of the first order in the case of linear materials and the susceptibility of the second or higher order in the case of nonlinear materials. As the main interest of our work is the inscription in silica which is centrosymmetric, we will limit the discussion to the dielectrics with the a linear response to moderate fields.

When such a material is exposed to a strong electric field the increase in the refractive index with the intensity of the field cannot be neglected (Kerr effect). As the light tends to propagate through the region with the higher refractive index, the pulse reshapes so that it propagates through the region in which the pulse intensity is higher rendering a self-amplified process that ends up in the collapse of the pulse. The described behaviour is known as self-focusing and plays crucial role in the propagation of the intense femtosecond pulses. It can be seen as a correction to the linear approximation that includes the third order susceptibility. However, there is the power threshold of self-focusing and if it is not exceeded the pulse does not collapse. The pulse power above which the diffraction of the pulse is completely cancelled by the self-focusing is called the critical power of self-focusing [99].

Electrons in the material respond differently to the fields of different frequencies, i.e. material is dispersive. If the field is in resonance with the natural frequency of the material, the response is instant and theoretically infinite. When the frequency of the field is far from the resonance, the response is delayed and the delay depends on the frequency. In this regime, the propagation constant can be expanded into a Taylor series around the working wavelength, the first derivative of which equals the inverse of the group velocity and the second is the dispersion coefficient $\beta_2 = \frac{\partial^2 \beta}{\partial \omega^2}$. As the spectral width of the applied gaussian

100fs pulse is about 10THz, the dispersion is significant.

When a pulse collapses into a point in space its energy becomes infinite which is physically impossible. Therefore, some other processes must halt the collapse. Diffraction and the normal dispersion counteract self-focusing and are dominant up to the equilibrium at which the pulse becomes trapped and propagates in the form of the Townes soliton, [106, 107]. However, at very high pulse powers self focusing is the dominant effect. The energy from the pulse is transferred to the material and as the energy is concentrated in both space and time this transfer is fast. Due to the slow response of the material compared to the duration of the pulse, it is still undergoing changes such as densification, stress, cooling, after the pulse has gone, resulting in the permanent modifications and therefore the refractive index change. However, the self-focusing is not the necessary condition for the index change. High intensity of the pulse can be achieved by using the lens to tightly focus the pulse. Most of the set-ups used for femtosecond micromachining make use of the external focusing to enhance the pulse intensity and enable inscription by the pulse powers below the critical power of the self-focusing, to reduce the necessary propagation distance thorough the sample and improve the controllability of the position of the index change.

Intense femtosecond pulse ionises material by the multiphoton absorption (MPA) and the freed electrons continue to absorb the pulse energy which is spent on freeing other electrons by the impact ionization and on the kinetic energy of the electron cloud. As the electron concentration grows, the electron cloud becomes a plasma and rapidly absorbs the energy from the pulse. Due to its lower refractive index, plasma defocuses the pulse and when the concentration is such that the critical frequency of plasma overcomes the frequency of the light, it becomes reflective. Recombination of electrons, transfer of energy to the lattice and thermal diffusion are slower processes that cause permanent changes in the lattice and subsequently in the refractive index. The precise mechanism of this change is not fully understood yet, but there has been a recent advance in that direction [93]. This model relates the refractive index change to the densification of material which is the consequence of the strain field around the region heated by the laser. The relation between the densification and the index change is simple and the problem is in finding the distribution of the stresses that lead to the densification. As these stresses are the consequence of the pressure exerted by the heated plasma it is important to know the distribution of plasma and the part of the pulse energy

deposited in it as the kinetic energy of electrons. We use the model described below to fill in the gap and calculate the required parameters of plasma.Our model is a slightly simplified version of the model proposed by Feit and Fleck [108] where the simplification is based on the study of the impact and the time scale of the processes involved.

3.4.2 Time Scales of the Processes Involved

Figure 3.6 reviews the time scales of the processes involved in the propagation of the laser pulse through the dielectric.

Pulses of the several tens of femtoseconds up to the several hundreds of femtoseconds fit

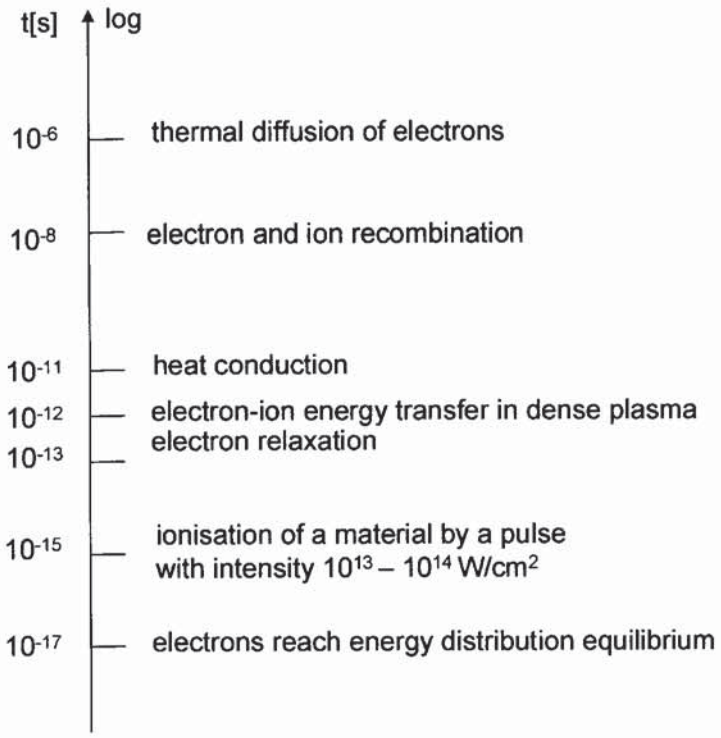

Figure 3.6: Time scales of the processes involved in the 'femtosecond' inscription.

into the narrow region where both models of the pulse propagation and its interaction with the material can be simplified without making significant errors. The pulse is long enough that the model which neglects Raman effects and the non-instantaneous response of the material still gives a good approximation of the pulse propagation. On the other hand, it is short

enough to pass through or scatter from the plasma before the excited electrons recombine and their energy has been transferred to the lattice (1ps) and long before the diffusion of the electrons becomes significant (1μs). Therefore, the only processes that affect pulse propagation are plasma generation, defocusing and absorption of the pulse by it. The absorption of the pulse happens over several femtoseconds during the resonance and results in the multiphoton ionisation that seeds the avalanche ionisation. These mechanisms have different time scales understanding of which is crucial in exploiting the advantages of the femtosecond micromachining as detailed in the next paragraph. At the end, it should be mentioned that there is the third type of ionisation called tunneling ionisation. In the strong electric field the potential barrier that keeps electrons bound to the atoms can be lowered enough that the probability of the electron tunneling becomes considerable. Since both multiphoton and tunneling ionisation require high field intensities, the distinction is usually made mathematically by the use of the Keldysh parameter $\gamma = \frac{\omega}{e}(\frac{mcn\varepsilon_0 E_g}{I})^{1/2}$. If $\gamma > 1.5$ multiphoton ionisation occurs, otherwise tunneling. The laser parameters used here give $\gamma = 1.8$, hence the multiphoton ionisation is dominant.

The impact ionisation owes its name to the collisional mechanism of the energy transfer from the free electrons to the bound electrons. When a free electron exposed to the external electric field acquires kinetic energy higher than the energy gap of the material, it is capable of freeing the bound electron by the collision. As the number of the free electrons grows, the probability of the collision increases and the process resembles avalanche. If the field is strong enough overheating and the breakdown of the material occur. The whole process usually lasts about 10ns. Multiphoton ionisation happens when a bound electron is simultaneously hit by several photons each of which transfers all its energy to the electron. The number of the photons needed for the K-photon ionisation can be estimated by the simple equation $K = [\frac{E_g}{\hbar\omega}]$ where E_g is the energy gap of the material, $\hbar\omega$ energy of a photon and the square brackets represent truncation to the whole number. As opposed to the avalanche ionisation, there is no build up of the process but the absorption of the pulse energy by the electrons finishes in a few femtoseconds and the free electrons reach the equilibrium one hundred times faster. Several important conclusions can be made. First, multiphoton ionization is much shorter than the pulse duration and can be treated as an instantaneous process. Second, the intensity threshold of the MPA is clearly defined which is also helped by the fact

that this process does not depend on the initial concentration of the free electrons and therefore depends on the impurities only as much as they modify the energy gap of the material. Third, the multiphoton ionization is much faster and dominant. It creates seed free electrons for the avalanche ionisation.

3.4.3 Mathematical Model

After the physics of all the relevant processes has been understood it is not a difficult task to put it into equations. It may at least seem so nowadays, after some brilliant books have been written about the nonlinear optics and the plasma physics, [79, 109–111], ...

For the purpose of this work we used the following model originally suggested by Feit and Fleck [108] and later developed into a fairly complex model, see e.g. [112–116]

$$i\mathcal{E}_z + \frac{1}{2k}\Delta_\perp \mathcal{E} - \frac{k''}{2}\frac{\partial^2 \mathcal{E}}{\partial t^2} + k_0 n_2 |\mathcal{E}|^2 \mathcal{E} = -\frac{i\sigma}{2}(1 + i\omega\tau)\rho\mathcal{E} - i\frac{\beta^{(K)}}{2}|\mathcal{E}|^{2(K-1)}\mathcal{E} \tag{3.1}$$

$$\frac{\partial \rho}{\partial t} = \frac{1}{n^2}\frac{\sigma_{bs}}{E_g}\rho|\mathcal{E}|^2 + \frac{\beta^{(K)}}{K\hbar\omega}|\mathcal{E}|^{2K} \tag{3.2}$$

The terms on the left-hand side of Eqn. (3.1) describe the effects of beam diffraction, group velocity dispersion (GVD), and Kerr nonlinearity, respectively. The latter is responsible for a catastrophic self-focusing which is limited by the effects described by the terms on the right-hand side of Eqn. (3.1) namely, plasma absorption ($\sigma\rho\mathcal{E}/2$) and multi-photon absorption ($i\frac{\beta^{(K)}}{2}|\mathcal{E}|^{2(K-1)}\mathcal{E}$). As its refractive index is lower than that of the surrounding material, the plasma defocuses the pulse which is described by the term $\sigma\omega\tau\rho\mathcal{E}/2$. In Eqn. (3.1) the laser beam propagation along the z axis is assumed and this equation is essentially a reduced paraxial approximation of the wave equation for the complex electric field envelope $\mathcal{E}$ with a carrier frequency ω in the moving frame of coordinates. Here $k = nk_0 = n\omega/c$ is the propagation vector, $k'' = \partial^2 k(\omega)/\partial\omega^2$ is the GVD parameter, $n(\omega)$ is a linear refractive index of the bulk medium, n_2 is the nonlinear coefficient describing nonlinear self-modulation (Kerr effect) such that $n_2|\mathcal{E}|^2$ is a nonlinear contribution to the refractive index, σ_{bs} is the cross section for inverse Bremsstrahlung, τ is the electron relaxation time, E_g is the ionization energy, and the quantity $\beta^{(K)}$ controls the K–photon absorption. Equation (3.2) implements the Drude model for electron-hole plasma in the bulk of silica and describes the evolution of

the electron density ρ. The first term on the right-hand side is responsible for the avalanche impact ionization and the second term for the ionization resulting from MPA. Equation (3.2) is suitable for description of the sub–picosecond laser pulses when plasma diffusion is negligible. Group velocity dispersion included in Eqn.(3.1) has been shown to lead to pulse splitting and the arrest of the collapse [117–120].

Initial conditions

Initial conditions depend on the focusing geometry. In accordance with the discussion in Sec. 3.4.1, we introduce ad hoc definitions of loose and tight focusing. Loose focusing is the focusing in which the numerical aperture of the beam does not exceed $NA = 0.1$ and it is practically realised by a simple lens with the focal length of a few centimetres. Tight focusing is defined by $NA > 0.1$ and it is achieved by the microscope objective. In both cases the input beam is considered gaussian and the effect of focusing is a change in the phase of the beam as given by equation:

$$\mathcal{E}(z=0,r,t) = \mathcal{E}_0 \exp\left(-\frac{r^2}{w_0^2} - \frac{ikr^2}{2f} - \frac{t^2}{t_p^2}\right) \tag{3.3}$$

where w_0 is the waist of the incident beam, t_p defines the pulsewidth $t_{FWHM} = \sqrt{2\ln 2}t_p \approx 1.177t_p$, and f is a focal length of the lens. This condition assumes a geometry in which there is no air space between the sample and the lens. The regime of loose focusing is used for the investigation of the prospects of inscription in the Kerr media.

The tight focusing is studied both theoretically and experimentally as it is commonly used in the set-ups for the in-bulk inscription. Microscope objectives are usually corrected for aberrations so that the optimal focusing is through the coverslip a few hundreds of micrometres thick. In the set-ups for the femtosecond inscription this element is omitted and the model must take into account the difference. The relevant parameters of objective supplied by manufacturers are numerical aperture, NA, working distance, WD, the thickness d_c, and the refractive index n_c of the coverslip. The usual values for the cover slip: $n_c = 1.51$ and $d_c = 170\mu$m were used. If the beam at the output of the objective is gaussian with the NA equal to the NA of the objective, the initial condition at some point z_{init} in the sample is:

$$\mathcal{E}(z_{init},r,t) = \mathcal{E}\mathcal{E}_r(z_{init},r)\mathcal{E}_t(z_{init},t) \tag{3.4}$$

$$\mathcal{E}_r(z_{init},r) = \frac{1}{1+i\frac{z_{init}-y}{z_0}}\exp(-\frac{r^2}{w_0^2(1+(\frac{z_{init}-y}{z_0})^2)}+\frac{ikr^2}{2z_{init}(1+(\frac{z_0}{z_{init}})^2)}) \tag{3.5}$$

$$\mathcal{E}_t(z_{init},t) = \sqrt{\frac{1}{1-i2k''\frac{z_{init}-y}{t_p^2}}}\exp-\frac{t^2}{t_p^2-i2k''(z_{init}-y)} \tag{3.6}$$

where the correction for the absence of the coverslip is included through the dependence of the beam focus on the parameters of the objective, distance of the sample from the objective d_s and the refractive index of the sample n_s.

$$y = d_s(1-n_s)+d_c\frac{n_s}{n_c}+\mathrm{WD}n_s. \tag{3.7}$$

The time dependent part of the field $\mathcal{E}_t$ accounts for the dispersion in the sample. The constant $\mathcal{E}$ is the initial condition on the propagation axis at the point $z_{init} = y$.

Normalisation

The applied normalisation reflects the nature of the physical problem. The electric field is normalised to the intensity threshold of the mutiphoton ionisation I_{MPA}: $\mathcal{E}(\vec{r},t) \rightarrow \sqrt{I_{MPA}}u(\vec{r},t)$, which is defined as the intensity at which the plasma ionization rate becomes very steep $I_{MPA} = \sqrt[K]{\frac{\rho_{BD}K\hbar\omega}{\beta^{(K)}\tau_p}}$. Plasma density ρ is in units of the breakdown plasma density ρ_{BD}. The radius r is in μm and the propagation distance z in mm. The coordinate system is moving with the group velocity of the pulse and the retarded time is normalised to the pulse duration τ_p. Hence we obtain the normalised system of equations

$$iu_z+\kappa\triangle_\perp u-\delta\frac{\partial^2 u}{\partial t^2}+\sigma|u|^2u = \gamma(\omega\tau-i)\rho u-i\mu|u|^{2(K-1)}u \tag{3.8}$$

$$\frac{\partial\rho}{\partial t} = \nu|u|^2\rho+|u|^{2K} \tag{3.9}$$

where the parameters are $\kappa = 0.510^{-9}k^{-1}$, $\delta = \frac{k''10^{-3}}{2\tau_p^2}$, $\sigma = 10^{-3}k_0n_2I_{MPA}$, $\gamma = 0.5\sigma_p\rho_{BD}10^{-3}$, $\mu = 0.5\beta^{(K)}I_{MPA}^{K-1}10^{-3}$, $\nu = \frac{\sigma_{bs}\tau_pI_{MPA}}{n^2E_g}$ with all the quantities in SI units.

3.4.4 Numerical Integration

Equation (3.8) is solved by an operator–splitting method which is second–order accurate in z. Radial diffraction term in the Laplacian operator of Eqn.(3.1) is integrated by means of

Crank–Nicholson scheme with zero boundary condition at the maximum radius. As both the angular term of the transverse diffraction operator and the dispersion operator are diagonal in Fourier space the Fast Fourier Transform was utilized to integrate them numerically. It should be noted that neither periodic nor zero global boundary conditions both in transverse space and time impose a significant restriction on the problem considered because the localized wave-packets vanish at the boundaries during the entire process of focusing and defocusing. The nonlinear part and the equation (3.9) were solved by integrating intensity and phase separately, the intensity by the second order Runge Kutta and the phase by the trapezoidal rule.

The described non-adaptive solver was used for handling the master grid in the adaptive solver and for benchmarking and back-to-back accuracy testing. It was implemented in C++.

3.4.5 Adaptive Mesh Refinement

The principle of adaptive mesh refinement is rather simple. Starting with one grid of a given resolution (in most of our 3D configurations $512\times64\times64$ mesh points are currently chosen) called master grid, the partial differential equations (3.8) and (3.9) are solved as usual. After a certain number of steps along the propagation axis z, it is checked whether the local numerical resolution is still sufficient on the entire grid and if it is detected that a finer grid is locally needed, a refinement is carried out so that a child grid is created using the interface with a parent grid as a new boundary, Fig. 3.7. In order to prepare for generation of the child grid, the points where the error of discretisation exceeds a given value and their adjacent are marked and are covered with rectangular grids of finer resolution as efficiently as possible. The algorithm used here is based on the classic one used by Berger and Colella [121]. On the child grids, the spatial discretisation length and the time step are reduced by a certain refinement factor. The new grids are filled with data obtained by interpolation from the preceding parent level. The integration advances on both the parent and the child levels until the local resolution becomes insufficient again. Regridding is repeated whenever the threshold for the error is locally exceeded, in this particular case if the domains of high intensity have left the finer grids or if local gradients have developed such that the prescribed accuracy is not guaranteed. The points of insufficient numerical resolution are collected on all grids of each level. If data existed on grids of the same level before the regridding, these are substituted to

the interpolated data from the parent grids.

The efficiency of the solution depends on the selected integration scheme. Due to the

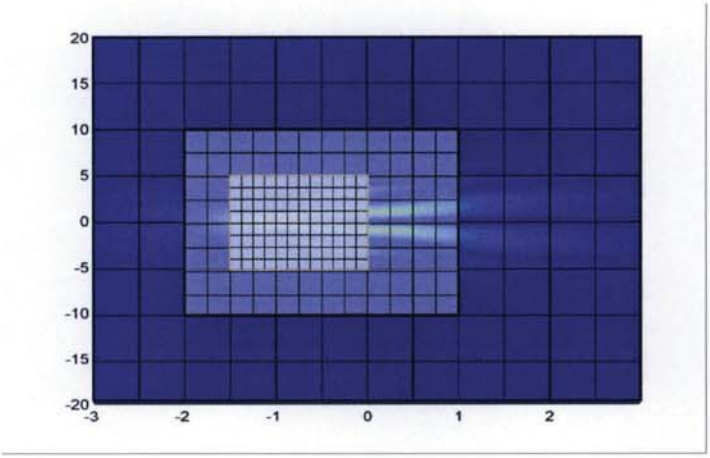

Figure 3.7: Adaptive mesh refinement: a hierarchy of meshes for resolving the finest details.

arbitrary mesh sizes on the refined levels, the optimal performance was achieved by using different schemes on the refined and the base level. On the base level, the integrator described in the previous section was used. On the refined meshes the semi–implicit Crank-Nicholson scheme from [122] and [123] was applied. The proposed discretisation reads

$$\left[1-\frac{i\Delta z}{2}\left(L^p_{qlm}+\frac{i\Delta z}{2}\partial_z(p_{nl})^p_{qlm}\right)\right]^{-1}u^{p+1}_{qlm}=\left[1+\frac{i\Delta z}{2}\left(L^p_{qlm}+\frac{i\Delta z}{2}\partial_z(p_{nl})^p_{qlm}\right)\right]^{-1}u^p_{qlm} \tag{3.10}$$

with $L=\kappa\Delta_\perp+\delta\partial_t^2+p_{nl}$ and

$$p_{nl}=\sigma|u|^2-i\frac{\gamma}{2}(1+i\omega\tau)\rho-i\mu|u|^{2K} \tag{3.11}$$

where κ, δ, σ, ν, and μ are dimensionless parameters described previously. To invert the operator on the left-hand side of Eqn. (3.10), a Helmholtz–type equation must be solved. As this linear operator is close to the identity for small steps Δz, a standard Gauss–Seidel relaxation method was employed with red/black ordering on each grid. In order to solve the problem globally, an additive Schwarz iteration was performed on top of the per–grid solvers. It is important to comment on the refinement criterion. We calculated the right–hand side of Eqn. (3.10) based on the actual grid spacing and twice the grid spacing. The criterion for the refinement was determined such that sufficient resolution was guaranteed during the evolution along the propagation axis z. The length of the integration step Δz was dynamically

adapted to ensure that at all times the (*i*) Courant–Friedrich–Levy condition was met to enforce the numerical stability and that the iterative method converged at a prescribed minimal rate and (*ii*) the maximal relative increment of both the amplitude and the nonlinear phase resulting from Eqn. (3.11) was always kept less than a prescribed limit, usually 1%. The implementation of the adaptive mesh refinement strategy described above was done in C++. As the structures needed for the adaptive mesh refinement and the integrator are independent of each other, it is relatively easy to use the code for other types of problems including various generalizations of the system Eqns. (3.1-3.2).

3.5 Simulation of the Inscription by the Realistic Experimental Set-up

Tight focusing by a microscope objective is a commonly applied set-up for the inscription in the bulk of material. It emerged as a solution to the problem of changing the index inside the material, while avoiding the catastrophic collapse and the modifications of the surface, proposed by Yablonovich. It is based on the facts that the self-focusing threshold is the pulse power and the inscription threshold is the pulse intensity. When the pulse with the power below the critical is tightly focused its radius in the focus can be small enough that the intensity reaches the inscription threshold, but the radius of the pulse at the surface is big enough that the intensity stays below the ablation threshold which is lower than the threshold of the in-bulk inscription. Other advantages of the tight focusing are the small volume and the large magnitude of the index change. Tightly focused pulses in both sub- and supercritical regimes can cause the microexplosions in material which result in the index change composed of the rarified material or void with the negative index change surrounded by the densified material with the positive index change (Figs. 3.4c), 4.1).

In the simulations the fixed value $\tau_p = 75$ fs was used. This pulsewidth corresponds to the critical energy of 0.2μJ for a critical power $P_{cr} = \lambda_0^2/(2\pi n n_2) \approx 2.2$ MW in fused silica with $n = 1.4533$ at the wavelength of Ti:sapphire laser $\lambda = 800$ nm and the nonlinear refraction index $n_2 = 3.2 \times 10^{-16}$ cm^2/W. The critical power is proven to be a crucial parameter that determines the evolution of the collapsing beam. The other parameters for the fused

silica are taken from [115]: GVD coefficient $k'' = 361$ fs^2/cm, inverse Bremsstrahlung cross section $\sigma_{bs} = 2.78 \times 10^{-18}$ cm^2, MPA coefficient $\beta^{(K)} = \hbar\omega\sigma_K\rho_{at}$, where the atom density $\rho_{at} = 2.1 \times 10^{22}$ atoms/cm^3 and $\sigma_K = 1.3 \times 10^{-55}$ cm^{2K}/W^K/s. $E_g = 7.6$ eV gives $K = 5$, i.e. the five–photon ionisation. $\rho_{BD} = 1.7 \times 10^{21}$cm^{-3} is the plasma breakdown density.

We have simulated the concentration of plasma created by the single pulse with the energy 4.6μJ equal to that used in experiments. The contours in Fig. 3.8 a) represent the concentration of plasma left in the silica after the pulse has gone. This plot was compared to the images of the refractive index change obtained by the phase microscope, Fig. 3.8 b).

When the plasma concentration reaches the breakdown value $\rho/\rho_{DB} = 1$ the plasma be-

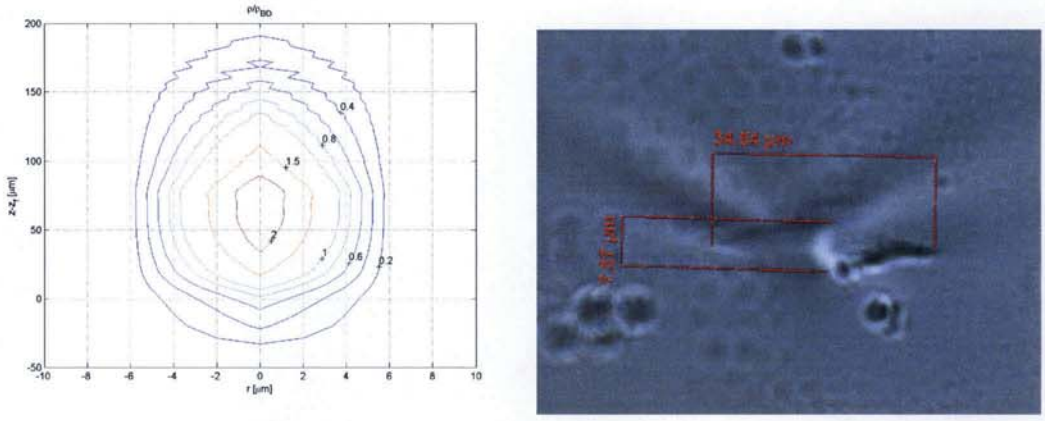

Figure 3.8: a) Simulated spatial distribution of the plasma generated by the pulse with energy 4.6μJ focused by the microscopic objective 40x, NA=0.65. Plasma density is normalised to the breakdown density ρ_{DB}. b) Corresponding refractive index change in silica.

comes highly absorptive, heats quickly and exerts high pressure onto the material that leads to the miscroexplosion and the formation of the shockwave. Therefore, the contour with the value 1 shows the region in which the microexplosion begins. The diameter of the contour with the value 1 is the same as the diameter of the index change 7.6μm observed in experiment. However, as the electrons are ionised in a few femtoseconds, i.e. during the pulse propagation through the focal region, it is not clear when the pressure exceeds critical, hence when the material is changed. The times from Fig. 3.6 show that the transfer of the electron energy to the ions, electron recombination and the thermal diffusion take much more time than the time pulse is present in the focal region, but the timescale of the microexplosion is not known. Therefore, due to the lack of the knowledge of the onset and duration of the modification of the material, the model can be considered valid up to the point at which the

plasma reaches the breakdown density. Although there has been the semi-empirical advance in this direction [97] the model of microexplosions remains a challenge.

While the available experimental set-up allowed for a study of the index changes induced by high energy pulses, it was not possible to measure index changes induced by the lower energy pulses nor to precisely control low pulse energies. An alternative way to study such index changes is to make use of the known properties of the devices inscribed by single femtosecond pulses. An example that shows how a fibre grating can be used for this purpose is given in Chapter 4.

3.6 Inscription in the Kerr Media

When the laser beam is focused onto the material refraction and reflection on the air–sample surface cause the distortion of the wavefront and a slight attenuation of the beam. The impact of refraction is particularly important when the sample surface is curved, e.g. inscription in optical fibres. Reflection must be prevented from the samples with very high refractive indices as discussed in Sec. 3.7.

Both the beam distortion and the reflection are eliminated when the immersion oil which has the same refractive index as the sample is applied between the objective and the sample. As the oil and the sample are index matched, the beam does not 'see' the interface between the two materials. This set-up has been used in microscopy to achieve the higher NA of the objective and therefore the higher resolution of the image. The same principle can be applied in set-ups for the laser inscription to minimise the focal spot and to reduce the abberations of the beam. The major drawback of the oil immersion objective is its short working distance that limits the inscription depth and makes the positioning and aligning of the set-up more difficult. However, these details do not bother the theoretician who can use only the advantages of the index-matching set-up.

The initial condition (3.3) is applied to both the tight and the loose focusing. The loose focusing is achieved by the simple lens with the focal length of $f = 4$cm and the microscope objective with immersion. As the microscope objectives are designed for a particular projection distance which is approximately equal to the tube length, the focal length of the

objective can be estimated as $f = \frac{tube\ length}{magnification}$. We simulate the pulse focused by the objective with the magnification 40x corrected for the standard tube length 160mm which has the focal length 4mm. Other parameters used in these simulations are the same as for the fused silica with the exception of the Kerr constant which was ten times bigger and the electron relaxation time for which the theoretical value from [115] was used.

3.6.1 Loose Focusing

Set-ups for femtosecond micromachining that use loosely focused pulses are far less common than the set-ups utilising the tight focusing. The main reason is the weaker confinement of the index change. However, this also means that instead of the microexplosion an interplay between the defocusing by plasma and the self focusing plays an important role. Inspection of the experimental data reported in [124] reveals that the onset of the breakdown of the material corresponds to the critical power of self focusing. However, if the self focusing is arrested by the defocusing and absorption on plasma, the breakdown is avoided and the relaxation oscillation of plasma can lead to interesting shapes of the index change. Such behaviour is particularly pronounced in the nonlinear media in which the self-focusing has the dominant effect on the pulse propagation. Here, all three regimes were examined with an aim to find an accurate spatial distribution of plasma generated by a single laser pulse. A prospect of generation of the plasma formations that can lead to the subwavelength refractive index changes is observed in the supercritical regime. The pulse-plasma dynamics which results in such a distribution of plasma is explained in detail.

In all the simulations the same input beam waist $w_0 = 2.5$ mm and the pulse width $\tau_p = 60$ fs were used. The lens had the focal distance $f = 4$ mm which gives $NA \approx nw_0/f$. Pulse energies used in the simulations were: 68 nJ in subcritical, 120 nJ in critical and 187 nJ in supercritical regime.

The impact of the pulse on material can be assessed from the amount of energy that it delivers to the material through the absorption by plasma. In Fig. 3.9 the calculated reduction of the pulse energy along the propagation axis for all three regimes is shown. The pulses with the higher energy reach the intensity threshold of MPA earlier, i.e. for smaller z. Such behaviour is generic for the femtosecond inscription and has been observed experimentally,

Sec. 3.7.

Typical asymptotic plasma density profiles for different initial pulse energies are shown

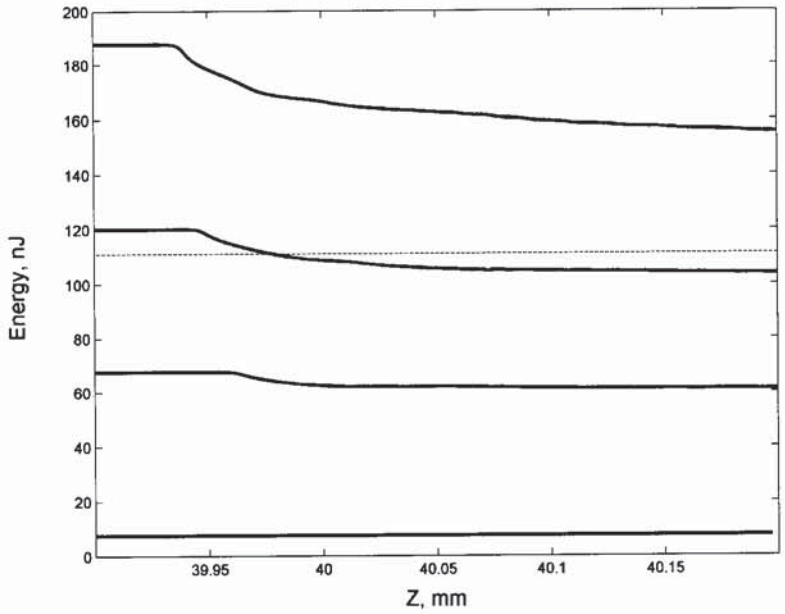

Figure 3.9: Simulated pulse energy as a function of the propagation distance for different input pulse energies. Horizontal dashed line corresponds to the critical power of self–focusing.

in Fig. 3.10. Subcritical evolution ($P_{in} < P_{cr}$) leads to a smooth plasma cloud without visible fine structure. This regime is attractive for the waveguide fabrication because it is characterized by the smooth subcritical evolution of the peak intensity. Larger energies lead to development of the pronounced periodic disks which results from the relaxation oscillations of the collapsing beam after the collapse is arrested by the multiphoton absorption. Disks of plasma are approximately 0.5μm in diameter and 1μm in height and appear with the period of 10μm. The pulse with the power just above the critical power of self focusing behaves in the same fashion as higher power pulses, but the maximal plasma concentration does not reach ρ_{BD} and the separation between the disks is less clear.

Nontrivial complex light and plasma dynamics and formation of subwavelength light patterns are illustrated by Figs. 3.11-3.12. The normalised intensity profile of the pulse and the concentration of the induced plasma are shown at different points along the propagation axis z near the focal point. Due to the initial condition $\rho(z=0)=0$ and the sharp threshold of the multiphoton ionisation $I = I_{MPA}$, the plasma is first formed at the peak of the pulse.

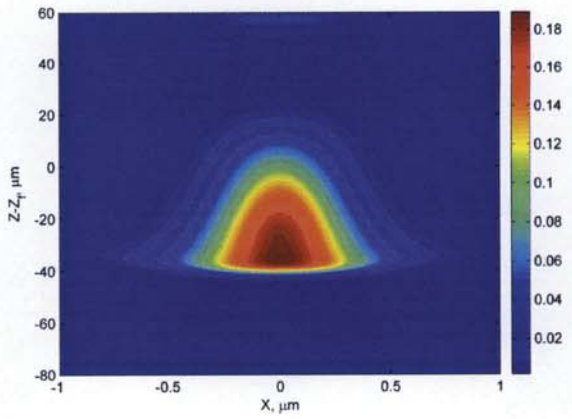

a) subcritical

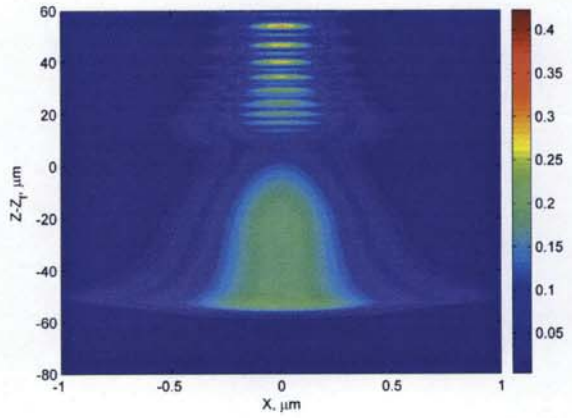

b) critical

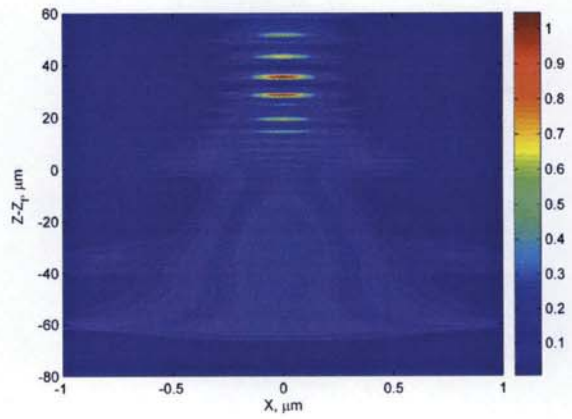

c) supercritical

Figure 3.10: Contours of the plasma density at infinite time after electric field is vanished for different input pulse energies corrsponding to those in Fig. 3.9: subcritical — 68 nJ, critical — 120 nJ, supercritical — 187 nJ .

Its concentration near the centre of the pulse grows by absorbing the energy from the trailing edge. Due to the lower refractive index, the plasma defocuses the pulse thereby causing the appearance of a ring trailing behind the central part, Fig. 3.11. Partial absorbtion of the pulse slows down the generation of plasma, self focusing overcomes defocusing, and the ring

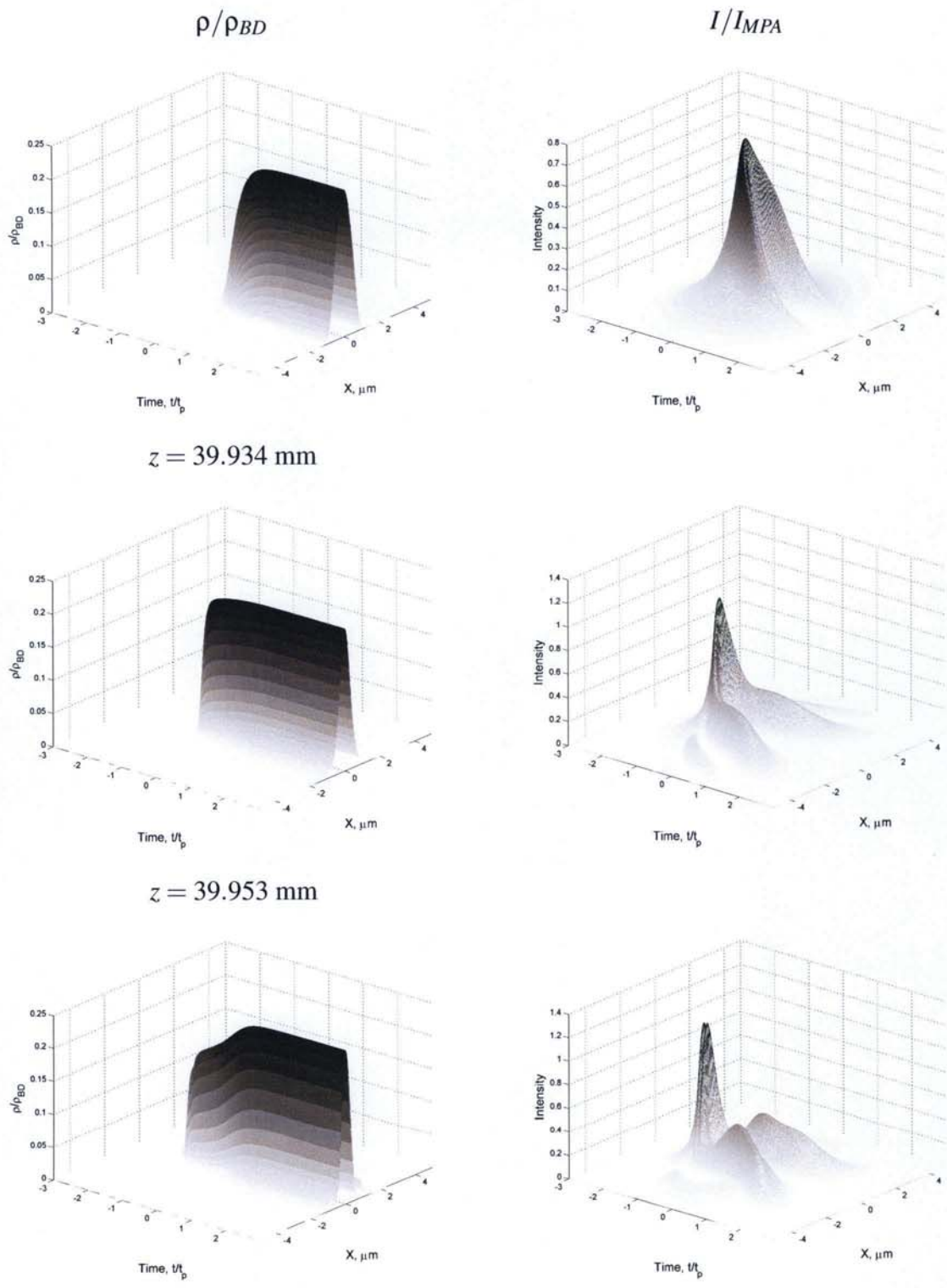

Figure 3.11: Dynamics of the plasma density (left column) and the pulse intensity (right column) at different positions along axis z.

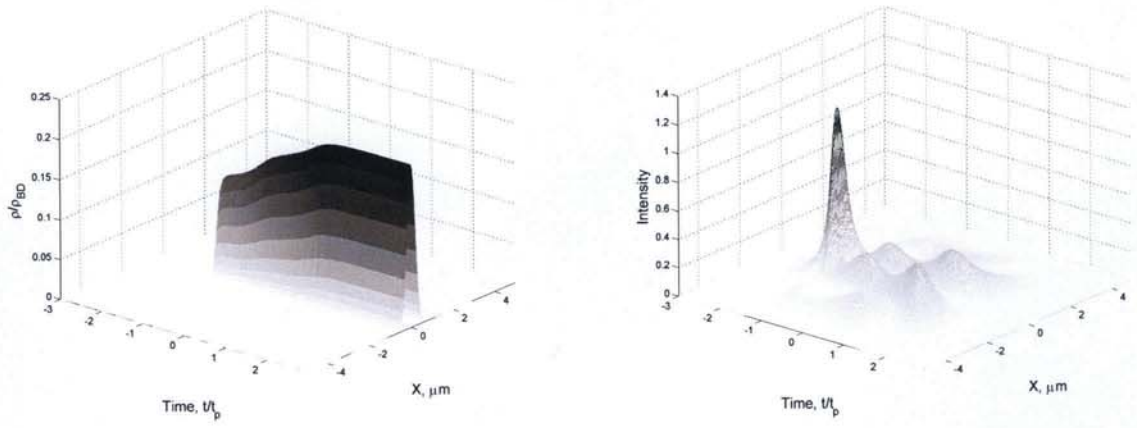

$z = 39.983$ mm

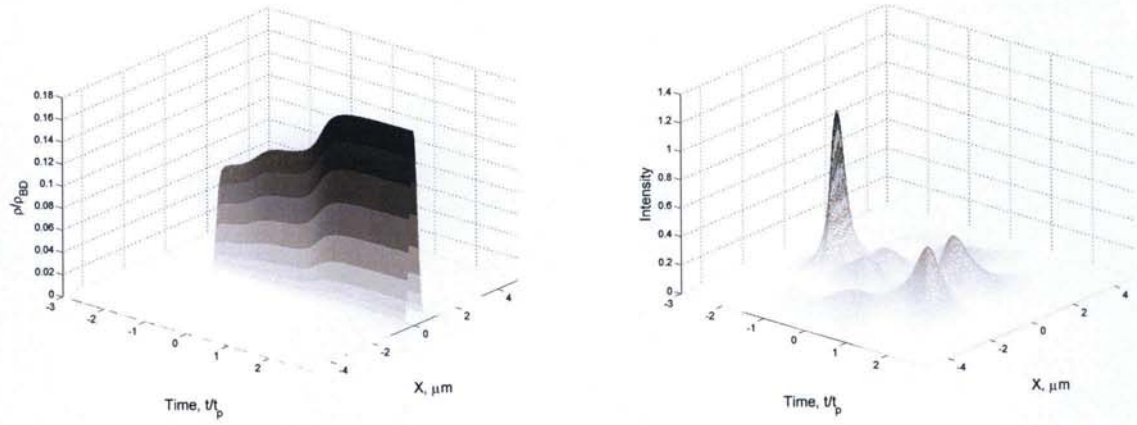

$z = 39.991$ mm

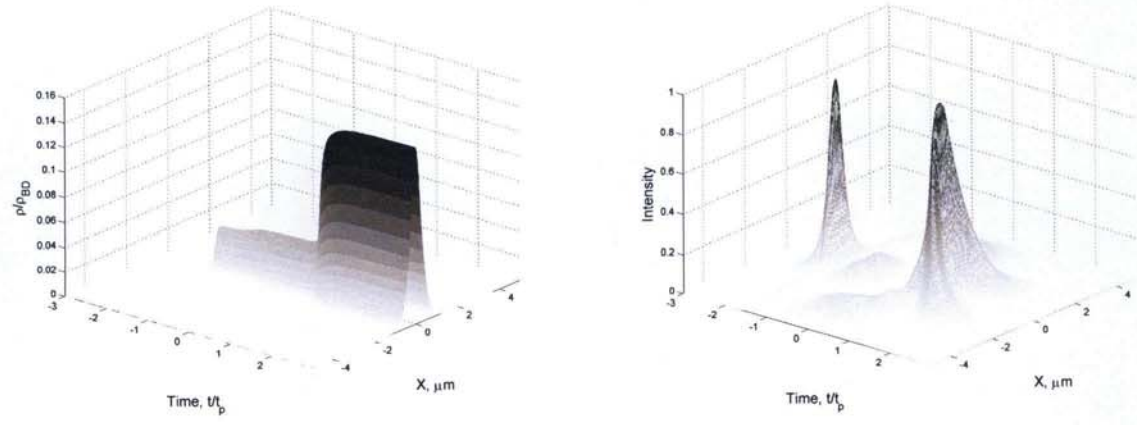

$z = 40.005$ mm

Figure 3.12: (Fig. 3.11 cont...)Dynamics of the plasma density and the pulse intensity at different positions along axis z.

shrinks to form a trailing pulse. Then the scenario repeats for the new pulse, resulting in a cascade of such pulses and periodic disks of plasma density, Fig. 3.10. Finally, a significant fraction of the original pulse energy is absorbed and the generation of plasma stopped.

3.6.2 Tight focusing

The pulse focused by the microscope objective reaches the critical breakdown intensity before sufficient plasma is created to arrest focusing. The critical plasma density is reached in all the regimes, superseding the collapse of the pulse by the breakdown of the material. The clouds of electron plasma left in the material after the pulse are shown in Fig. 3.13. A significant reduction in the spot size compared to the plasma formations in Figs. 3.8, and 3.10 is due to the increase in the numerical aperture of the lens. This demonstrates the main advantage of femtosecond inscription – the possibility to generate a well confined refractive index change.

3.7 Demonstration of Inscription in Different Materials

One of the advantages of the femtosecond machining is the ability to induce changes in the bulk of almost any material that is transparent at the wavelength of the laser, even diamond [125]. This has been demonstrated by the inscription in borosilicate (BK7), fused silica, quartz and polymers.

It was possible to create smooth index change by a single pulse and trains of pulses in all sampled glasses, whereas the threshold for polymer was much lower and the attempts resulted in non-smooth waveguides and the damage shown in Fig. 3.4 d). In this thesis the polymers were used purely for the demonstration of the structural damage induced by the femtosecond laser, which must not be understood as definitive result in the femtosecond machining of polymers. Indeed, the successful refractive index changes in PMMA used for the fibre coating were reported in [126], even the inscription in fibre without changing the coating [127].

The method described in Sec. 3.3 was used to determine the thresholds of refractive index change in fused silica and borosilicate glass. They were compared with the results of

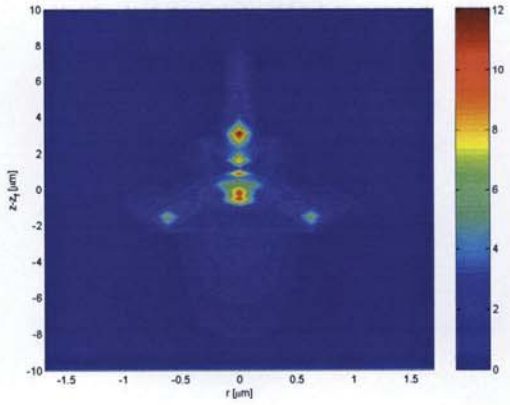

a) subcritical

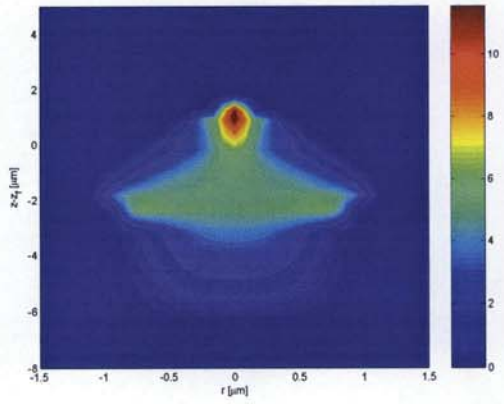

b) critical

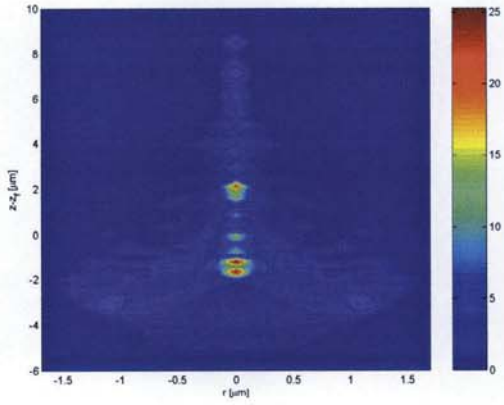

c) supercritical

Figure 3.13: Contours of the plasma density at infinite time after electric field is vanished for different pulse energies: subcritical — 68 nJ, critical — 120 nJ, supercritical — 187 nJ.

other groups. The threshold of the index change was defined as the laser power at which the change is detectable by the phase microscope. The precision of the measurements was increased by the refinement of the power resolution around the initially detected threshold power. However, it turned out that the experiments were the easier part of the job because

different groups used different pulse repetition rates and focusing conditions that were difficult to compare. The results are presented in Table 3.1 together with the relevant information on the inscription conditions. Rather than being conclusive, they should draw attention

material	Schaffer [128]	Glezer [129]	Streltsov [130]	Sudrie [98]	ours
fused silica	0.3	0.03	0.05	0.1	0.08
borosilicate	-	-	0.2	-	0.2
NA	0.65	0.45	0.26-0.28	0.5	0.65
τ_p [fs]	100	110	40	160	150
pulses/structure	1	not specified	1000	1000	1

Table 3.1: Energy thresholds [μJ] of the refractive index modification in the fused silica and borosilicate measured by different groups. In the case of high repetition rate inscription the number of pulses per structure N is estimated from the structure diameter D, the translation speed of the sample v and the pulse repetition rate f as $N = Df/v$.

to the need for a systematic study of the inscription by femtosecond pulses that would aim to clearly define the refractive index profiles achievable by different pulse parameters. The fact that the interaction is dependent on the material and its purity makes the challenge even bigger. Similar open questions are addressed in the last section of the chapter.

Ablation of III-V semiconductors

P- and n-type GaN (supplied by the Wide Band Gap Semiconductors Group at the University of Bath) were probed by the femtosecond laser. Since their refractive index was much higher than that of silica ($n_{GaN} = 2.35$) the objective had to be protected by redirecting the beam back-reflected from the sample. All the attempts resulted in the surface ablation, partly due to the small thickness of the semiconductor that is an obstacle for the in-bulk writing (see Sec. 3.5), partly due to the lower thresholds. The latter can be explained by the following reasons. First, the energy gap of GaN is 3.4eV which corresponds to 2-photon absorption at 800nm. Second, the initial concentration of free electrons is higher than in silica, hence there are more seeding electrons and the avalanche ionization builds up faster. The latter is supported by the fact that it was more difficult to inscribe small regular structures in n- than in p-type semiconductor. As many of the inscribed structures deteriorated with time and those inscribed with larger powers, hence more stable, were in n-GaN, they are given as

an example in Fig. 3.14.

The ablated region consisted of a smooth central disk surrounded by the material pushed out of the centre, Fig. 3.14. The radius of the ring increased with the exposure time, i.e. with the number of pulses. An interesting effect was observed: the ablated structure acted

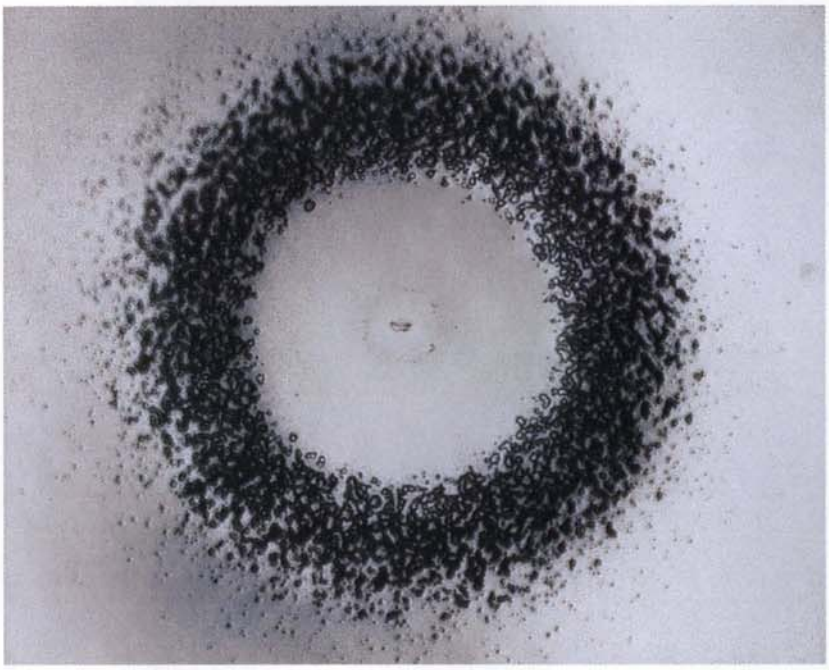

Figure 3.14: Ablation of n-GaN.

as a convex lens so that the in-bulk structures inscribed beneath it during the same process appeared slightly magnified. This can be the consequence of the positive index change that acts as a positive lens. Another explanation may be formation of the concentric periodically densified rings analogous to the zone plate. Indeed, the inspection of Fig. 3.14 reveals a few concentric circles of different shades within the main ring. Similar shapes observed during the ablation of GaAs were explained by thermodynamic phase transitions resulting in the formation of the Newton rings, [131, 132].

3.8 Near Surface In-Bulk Structures

Over the last several years there has been much interest in surface plasmons, mostly oriented towards biomedical applications [133]. As the penetration depth of a plasmon is of the order

of several microns to a few tenths of microns, it would be beneficial to be able to inscribe a waveguide or grating within that depth. When such a waveguide is coated by a metallic film the periodic disturbance in it, e.g. blazed or long period grating, can couple the light to the resonant plasmon, which can be used for the distributed sensing of the external refractive index or as interconnect in optical circuits.

A series of trials in which the waveguide like structures were inscribed $4.5-5\mu$m from the surface resulted in a set of waveguides at different depths. These were written in borosilicate glass using the 40x objective and pulse energies 0.24μJ, 0.46μJ and 0.8μJ. The translation speed of the sample was 0.5mm/s. The focal point was kept at the fixed depth and the distance of the waveguide from the surface was controlled by the laser power. Pulses with the energies above 1μJ created the damage on the surface, whereas those with the energies below 0.2μJ did not make an observable index change. This threshold corresponds to the critical power of self focusing in silica. The image in Fig. 3.15 was obtained by focusing on the surface of the sample.

The refractive index profile of the waveguide written by 0.46μJ at the depth 4.8μm is shown

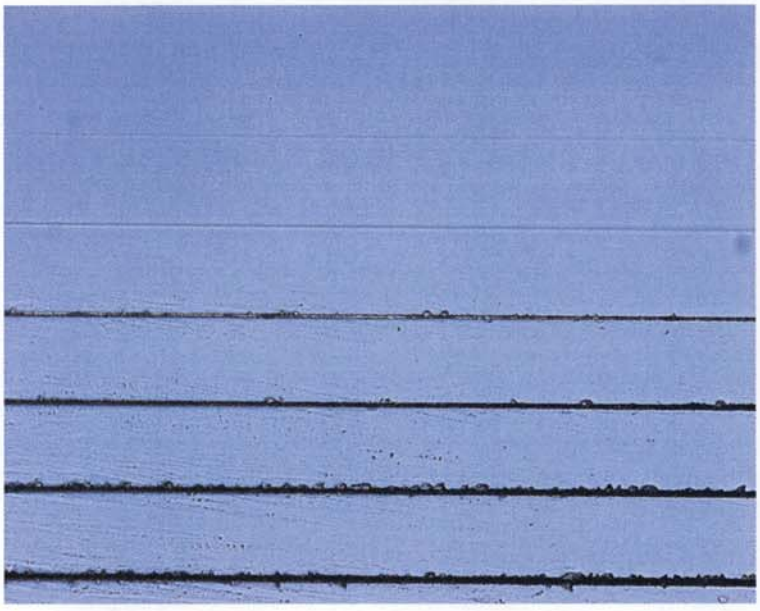

Figure 3.15: Structures inscribed by femtosecond laser pulses focused $4.5-5\mu$m below the surface of the borosilicate glass.

in Fig. 3.5a). Using the condition for the single mode fibre $V=\frac{2\pi}{\lambda}a\sqrt{2n\Delta n}<2.405$ where $\Delta n=4\times10^{-3}$ and $a=0.6\mu$m are obtained from Fig. 3.5 a) it can be easily seen that this

waveguide is single mode at any wavelength $\lambda > 170nm$.

3.9 Proof of the Durability of the Refractive Index Change

There is evidence that the refractive index change induced by the fs pulses in step-index fibres decays with time (discussions with T. Allsop and A. Martinez) or completely disappears from lithium niobate [134]. As the vast number of applications of femtosecond micromachining is based on using undoped silica, we have conducted a long term study to examine the durability of the index change.

The structures inscribed by the single laser pulses of different powers were characterised just after the inscription and 27 months later. The details of the experimental set-up and the first set of measurements were reported in Sec. 3.3. In Fig. 3.16 both the new and the old results are shown. While the length L of the structures (dimension along the pulse propagation

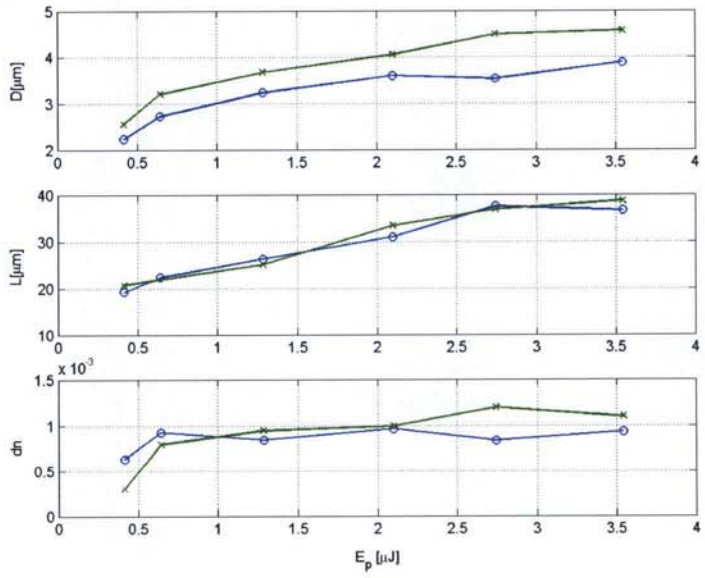

Figure 3.16: Comparison of the diameter, length and refractive index change of the structures immediately after the inscription in the fused silica (o) and 27 months later (x).

direction) did not change, the diameter D (in the plane perpendicular to the pulse propagation direction) slightly increased. This may indicate a slow relaxation of the transverse stresses induced by the shock wave. The same reason may have led to the reduction in the index

change obtained by the lower energy pulses. Higher energy pulses caused the damage in silica that barely changes in time. The measurements were taken by the phase microscope and QPm the accuracy of which depends upon the precision of focusing onto the sample (see Sec. 3.2). As the structures were of the considerable length, a stack of images at the constant separation along teach structure was taken and the sharpest was chosen for the focus. Due to the subjective decision upon the sharpness of the image, the refractive index measurements are not absolutely accurate. However, the described trends in changes are consistent and the conclusion that the inscribed structures withstand the time without major changes can be reliably made.

3.10 Conclusions

An experimental and theoretical study of the interaction of the femtosecond laser pulse with the fused silica has been conducted in order to establish the relation between the inscription parameters and the index change. The energy deposited in material as the thermal energy of electron plasma has been calculated for different inscription parameters. This is the missing link in the study of the femtosecond inscription that should serve as input to the model proposed in [105] which can predict the permanent index change from the distribution of the thermal energy. In the regime of self-focusing or when the pulse is tightly focused onto the material the pulse intensity can be high enough to cause the breakdown of the material. Our model can predict the onset of the breakdown but fails to predict the development of the microexplosion. The fine spatial resolution of the focusing pulse on very different spatial scales was achieved by the adaptive mesh technique, thus allowing the detection of the submicron formations of plasma induced in the medium with a large Kerr constant by the pulse in the supercritical power regime. It is suggested that this can lead to the longitudinal inscription of the index changes at the subwavelength scale.

The theoretical study was motivated by the experiments on the inscription by single femtosecond pulses in different materials conducted previously. The two main types of index change were observed: smooth and positive changed used for the inscription of waveguides and damage-like and negative used for inscription of fibre gratings. While the small index

changes were difficult to characterise, the index profile of the larger was measured and compared to the simulations of the plasma clouds that are left in the material after the pulse has gone. The radial distribution of the critical plasma was comparable to the dimension of the inscribed void, but the model is still unable to account for the changes in material after the breakdown. The durability of the index change in the fused silica was proven by comparing the measurements obtained immediately after the inscription and 27 months later.

Although the demanding task of finding the distribution of plasma has been accomplished, we are still striving to understand the mechanism of the refractive index change. Therefore, the work on the extension of the model to include the energy transfer from plasma to the lattice that leads to the refractive index change is in progress. The prospect remains for refinements such as including the self-steepening and the Raman effect. However, the mathematical model for the mechanism of damage is not yet clear. As this regime is important for the point-by-point inscription of the devices, it is important to understand it better or at least to characterise it more systematically. As the difficulties mentioned earlier can be encountered in the straightforward measurements, an alternative method is suggested that makes use of the well known properties of the fibre gratings.

The author has learnt from experience that the fabrication of the devices is often more compelling than the statistical approach needed for the investigation of the single shot structures and that the former tailors the aims of the latter. This is also obvious from the piecewise structure of this chapter. However, the comprehensive study that merges theory with experiment is not only needed but very interesting and sometimes intriguing. When just a 'simple' question: What is 1fs? is such a great challenge to the mind, how marvelous it is to know how to create it, to measure it and even to use it as a tool.

Chapter 4

Modelling of Long Period Gratings Inscribed by Femtosecond Laser

The considerable interest in the femtosecond micromachining as a new technique for inscription of the fibre gratings [14, 15] is based on the three main advantages given in the retroactive order:(*i*) possibility of inscription through the fibre coating which is not possible by any other technique [127], (*ii*) fabrication of the thermally stable gratings that can operate at the temperatures up to 1000°C [90, 135], (*iii*) the possibility to inscribe grating anywhere in the fibre cross section. The first is a consequence of the sharp threshold of multiphoton absorbtion that is exceeded only very close to the focus of the tightly focused pulse. Care must be taken not to exceed the threshold of index change or ablation of the polymer coating which is lower than for silica. The gratings are thermally stable due to the irreversible structural changes in silica induced by the intense femtosecond pulses which corresponds to the type II gratings written by UV. The advantage (*iii*) is the result of a very good confinement of the index change and the possibility to change non-photosensitive cladding. By displacing the grating from the centre of the core [136] or by inscription in cladding [137] an unusually high birefringence was achieved.

Although the physical origin of the effect is the same, in the experimental practise grating and fibre birefringence are differently quantified. Fibre birefringence is the difference in the effective refractive indices of the perpendicularly polarised core modes. Grating birefringence is defined as the difference between the resonant wavelengths for two perpendicular

polarisations. For FBGs these two values are proportional because only the core mode is involved ($\lambda_{res} = 2n_{co}^{eff}\Lambda$, therefore $\Delta\lambda_{res} = 2\Delta n_{co}^{eff}\Lambda$), which is not the case for LPGs in which both the core and the cladding modes contribute to the birefringence ($\lambda_{res} = (n_{co}^{eff} - n_{cl}^{eff})\Lambda$, therefore $\Delta\lambda = (\Delta n_{co}^{eff} - \Delta n_{cl}^{eff})\Lambda$).

4.1 Experimental Evidence

Figure 4.1 shows the side view and the cross section of a typical FBG written by the femtosecond laser [96] and Fig. 4.2 the side view of an LPG [136]. The index profile of the LPG is similar to that in 4.2.

The birefringence of the FBG reported in [15] was in the range $20-36$ pm that corre-

Figure 4.1: a) Side view and the cross section of the FBG [96].

sponded to the fibre birefringence within $2\cdot10^{-5}-3\cdot10^{-5}$. LPGs reported in [136] had the birefringence of 10 nm that corresponded to the similar difference in effective refractive indices and which surpasses the birefringence usually observed in gratings fabricated by other techniques [84, 138]. Fig. 4.2 shows this LPG and its spectrum measured for two perpendicular polarisations of the input light.

The birefringence of the grating increased with the energy of the pulse or with the decrease in the speed of the translation of the sample. When the grating was thermally annealed, the birefringence decreased and almost disappeared at 800°C. The blue shift in resonant wavelengths was observed for the temperatures below 800°C and the red shift for the higher

Figure 4.2: Side view (up) and the spectrum of the LPG (down) inscribed point-by-point by the femtosecond laser pulses [136].

temperatures, [71].

4.2 Modelling

Since the problem of modelling of the devices inscribed by the femtosecond laser emerged relatively recently, the models are rarely found in literature [139], as well as the systematic experimental data such as those in [90]. The lack of understanding of the mechanism of the refractive index change is a hurdle usually bypassed by empirical results and by simulations similar to those in Sec. 3.6.2. As discussed in the Introduction, modelling of these devices can be used to get insight into the process of inscription. Here, we first explain the physical background and then demonstrate three levels of modelling of the birefringent gratings inscribed by the femtosecond laser in the SMF-28e. At the end we show how the better of these models can be used to study the dependency of the inscribed structure on the energy of the femtosecond pulse.

4.2.1 Physical Model

A tightly focused intense pulse is likely to produce heated electron plasma that exerts pressures of tens of GPa on the surrounding material [97]. As a consequence, the shock wave is generated and the material is pushed outside the focal region. The final refractive index change comprises the rarefied material in the centre that is surrounded by the densified material. According to the results of the thermal annealing [71,90], both I- and II- type-like index changes are present, whereby the permanent structural change in the central part corresponds to the type II and the densified region around it to the type I. As the reports on the formation of the colour centres in silica due to the exposure to the IR femtosecond laser pulses are not consistent [130, 140, 141], we will use the model according to which the densification and stresses are responsible for the index change.

It is assumed that the gratings can be described by the coupled mode theory the details of which can be found in the Introduction. As opposed to the previously studied LPGs in PCFs in which the broken symmetry was a second order contribution to the index change, the intrinsic property of the LPGs studied in this chapter is that they are asymmetric. Therefore, the modes of the fibre with the grating cannot be obtained as a superposition of the modes of the unperturbed fibre and the adequate basis is the space of eigenmodes of the fibre with the average index perturbation.

The three models of different complexity are: the fibre with a void in the core, the fibre with a void surrounded by the constant positive index change and the grating with the profile similar to that in Fig. 3.5b).

4.2.2 Numerical Method

The index profiles of the fs-inscribed gratings described above contain features of very different dimensions, e.g. cladding with the diameter of 125μm and void with the diameter 0.5μm, and can display quite complex geometry as the index change can spread into cladding. For these reasons, the finite element method was chosen as a tool for the modal analysis of the grating. All numerical models were implemented using the commercially available software Comsol 3.1 [63].

An excellent accuracy of the method for the step-index waveguide was confirmed in Sec. 2.2.2. As the birefringence is one of the distinguishing characteristics of the LPGs studied here, the numerical precision was additionally tested for the case of SMF-28e. Fig. 4.3 shows the numerical birefringence of the unperturbed fibre as a function of the maximum size of the mesh element (triangular mesh). The script for the mode evaluation was further used in the code for fitting the numerically obtained resonant wavelengths to the measured grating spectra. Therefore, the maximum mesh element size was set to 0.5μm to obtain both the satisfactory precision and a reasonably short calculation time. For such a mesh the numerical birefringence was $1.75 \cdot 10^{-7}$, which is much smaller than the observed grating birefringence of the order of 10^{-5}.

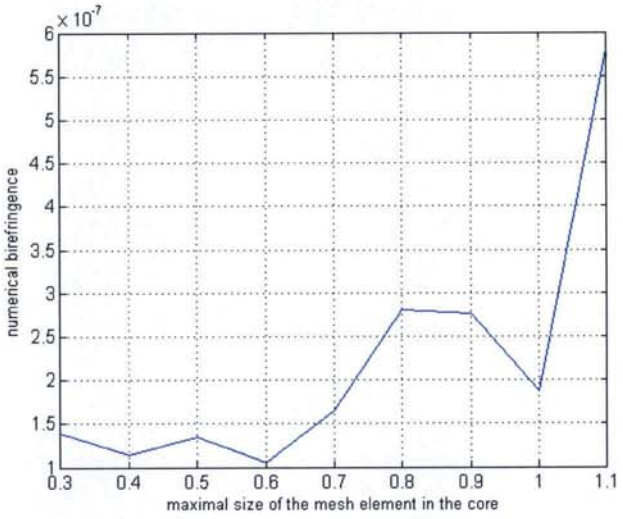

Figure 4.3: Numerical birefringence of SMF-28e vs. maximum size of the mesh element.

4.2.3 Void in the Fibre Core

First, the simple geometry shown in Fig. 4.4 is considered. The fixed parameters were those of the standard SMF-28e (www.corning.com) and the refractive index of the void $n_{void} = 1$. The model is used to investigate the dependency of the birefringence on the radius of the void and its displacement from the centre of the core d.

If the void is much smaller than the core or it is in the outer part of the core where the field of the fundamental mode is small, the effect it causes can be considered a perturbation. In our case the diameter of the void is smaller than the wavelength and we also chose the void to

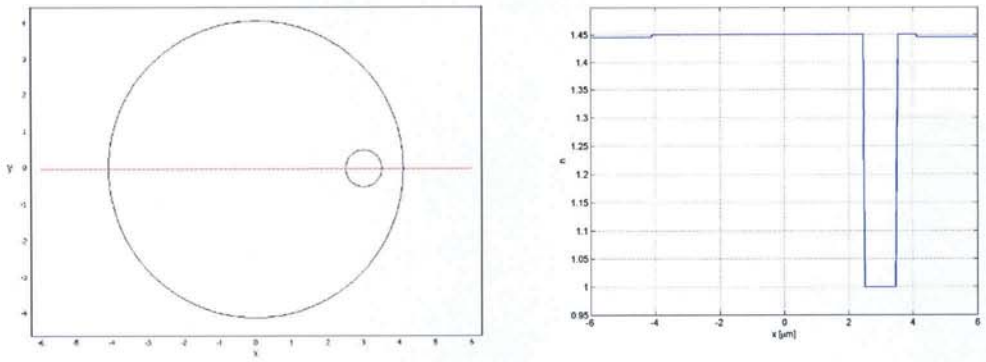

a) b)

Figure 4.4: a) Fs-inscribed void in the core of SMF-28e. Dimensions are in μm. b) Refractive index profile of this structure along x-axis (red line in a)).

be 3μm from the centre of the core, so that the application of perturbation theory is justified. According to the boundary conditions, the magnetic field is almost the same as the magnetic field of the unperturbed fibre, whereas the change of the electric field is significant. The last represents a difficulty for the analytical approach because it requires an approximate solution for the electric field in the void. Here the approach from [30] is adopted and the quasi-static approximation to the electric field in the void is applied. The birefringence for the arbitrary refractive index of the perturbation is given by the equation

$$\Delta n_{eff} = \frac{n_v^2 - n_{co}^2}{J_1^2(U)} \frac{R_v^2 \pi}{4} \sqrt{\frac{\varepsilon_0}{\mu_0}} \left(\frac{8 a_1 a_2 n_v^2}{n_v^2 + n_{co}^2} J_0(U_0) J_2(U_0) + \frac{U^2}{R_v^2 k_0^2 n_{eff}^2} J_1^2(U_0) \right) \tag{4.1}$$

in which $a_1 = 0.5(F_2 - 1)$, $a_2 = 0.5(F_2 + 1)$, $F_1 = (UW/V)^2(b_1 + (1-2\Delta)b_2)$, $F_2 = (V/UW)^2/(b_1 + b_2)$, $b_1 = 0.5U(J_0(U)/J_1(U) - J_2(U)/J_1(U))$, $b_2 = -0.5W(K_0(W)/K_1(W) + K_2(W)/K_1(W))$, V,U,W,Δ are standard fibre constants, see e.g. [30], J and K are the Bessel function of the first kind and the modified Bessel function of the second kind, respectively, R_v and $n_v = 1$ are radius and index change of the void. It should be made clear that the used perturbation approach relied on numerics for the calculation of the effective refractive index and Bessel functions; nevertheless the term 'numerical solution' refers only to the pure numerical solution. The dependence of birefringence on the void radius was calculated by both methods and the results are shown in Fig. 4.5. Expectedly, the error of the perturbation theory decreases with the weakening of the disturbance, but for all the simulated values of R_v the obtained birefringence differs significantly from the numerical result. For $R_v < 0.3\mu$m the numerical

error of $1.75 \cdot 10^{-7}$ becomes detrimental. Therefore, it is suggested to apply the perturbation theory when the void is small and the numerical method otherwise.

The effective indices of the core modes were calculated numerically. They decreased

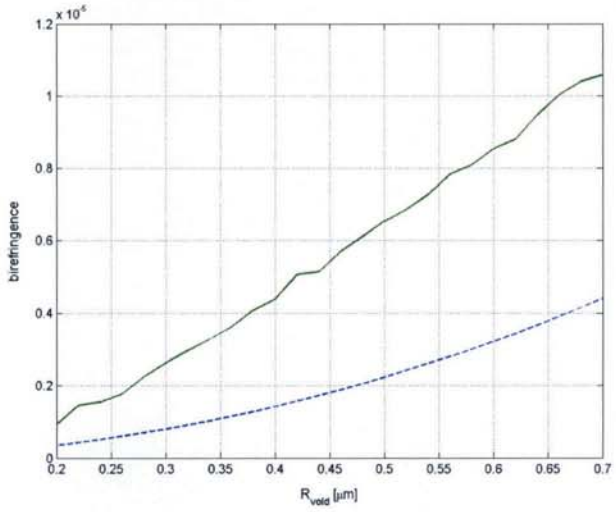

Figure 4.5: Numerically (solid line) and analytically (dashed line) obtained birefringence of the fibre with the spherical void positioned 3μm from the centre of the core as a function of the void radius.

with the void size. The effective index was higher when the polarisation was perpendicular to the displacement of the void. This can be explained by the fact that the field effectively penetrates less into the air which has lower refractive index than the index of silica and can qualitatively explain the blue shift of the spectrum of LPGs when the pulse energy was increased reported in [136]. For the voids observed in experiments, with the diameters of up to 1μm, this model gave the birefringence of the order of 10^{-6} which was not enough to account for the measured separation between the grating resonances at different polarisations. The straightforward improvement of the model is to change the spherical void by an ellipsoidal one. Figure 4.6 is a plot of the birefringence as a function of the eccentricity of the ellipse for the two extreme cases: (*i*) when the major axis is perpendicular to the direction of the displacement of the void from the core (dashed line) and (*ii*) when it is parallel to it (solid line). As the smaller part of the field propagates through the elliptical void when the field vector is parallel to the major axis, the effective index of the mode polarised in that direction is higher than the refractive index of the mode perpendicularly polarised. Therefore, the displacement and the eccentricity of the ellipse in the case showed by the dashed line have the

same effect and in the case showed by the solid line the opposite effects. In the latter case the difference in indices $n_y^{eff} - n_x^{eff}$ crosses zero, but as the birefringence in Fig. 4.6 is defined as the difference between the higher and the lower effective index, it is always positive.

The birefringence is notably bigger than in the case of the spherical void and for high eccentricities of the ellipse it is close to the birefringence obtained in measurements. As the cladding modes are not significantly affected by the perturbation, the birefringence of both FBG and LPG comes from the difference in the effective refractive indices of the core modes.

In conclusion, we have examined a simple model of the refractive index change composed

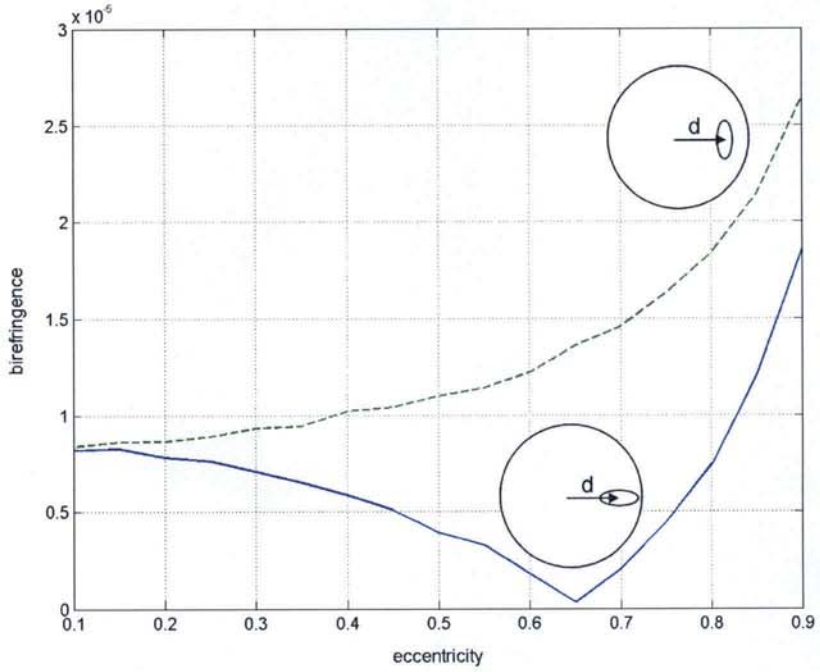

Figure 4.6: Numerically obtained birefringence of the fibre with an ellipsoidal void vs. eccentricity of the void for two orientations of the ellipse in the fibre cross section. The major axis of the ellipse is 0.6μm.

of a singular void in the core and showed that only the void in the shape of the highly eccentric ellipse with the diameter over 1μm can cause the birefringence close to that observed in experiment. The analytical solution obtained by the perturbation theory is accurate only for the very small void diameters but gives correct order of magnitude for bigger voids and can be used as the zero estimate of the birefringence of grating in the step-index fibre.

4.2.4 Void Surrounded by the Constant Refractive Index Change

In this section the model is improved by adding the densified region around the void. The void is assumed to have a spherical shape with radius R_v and that all the material is pushed out of it, so that it is close to vacuum with the refractive index $n_v = 1$. Such voids were observed on the electron microscope scan of the sample that was previously chemically etched [97]. The densified region is modelled as a concentric sphere of the radius Rp which contains all the material pushed out of the void, Figs. 4.7, 4.8.

Under the assumption that the densification $\Delta\rho/\rho$ is constant in the whole volume around the void, the conservation of mass gives the expression for the perturbation radius: $R_p = R_v\sqrt[3]{1+\Delta\rho/\rho}$. The dependence of the refractive index on density is given by the Lorenz-Lorentz equation [31] and the relation between the change in refractive index and the densification by the first term of its Taylor expansion

$$\frac{\Delta n}{n} = \frac{(n^2+2)(n^2-1)}{6n}\frac{\Delta\rho}{\rho}. \tag{4.2}$$

The contribution to the refractive index change from the stresses caused by densification was neglected. Figures 4.7, 4.8 shows the two characteristic cases in respect to the volume of the index change: a) the whole change is within the core and b) some of the material is pushed out to the cladding.

The model has two unknown parameters and our choice of R_v and dn was motivated by

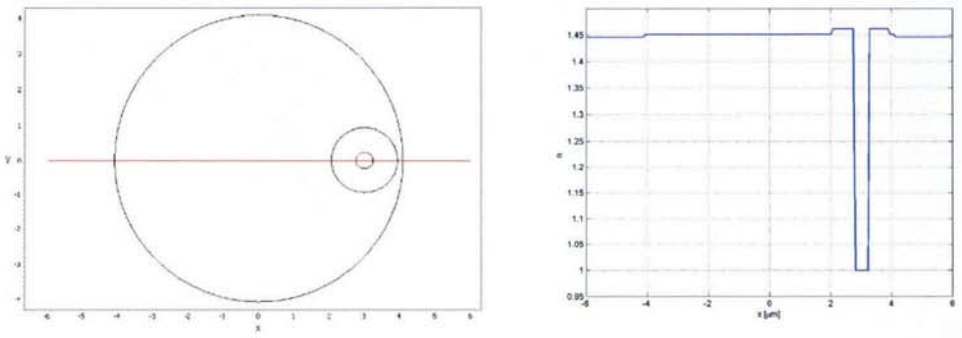

a) b)

Figure 4.7: a) Axes are in μm. b) Refractive index profile of this structure.

the fact that index change around the void can be measured by QPm and that the dependency of the void diameter on the pulse energy had already been modelled to match the experimen-

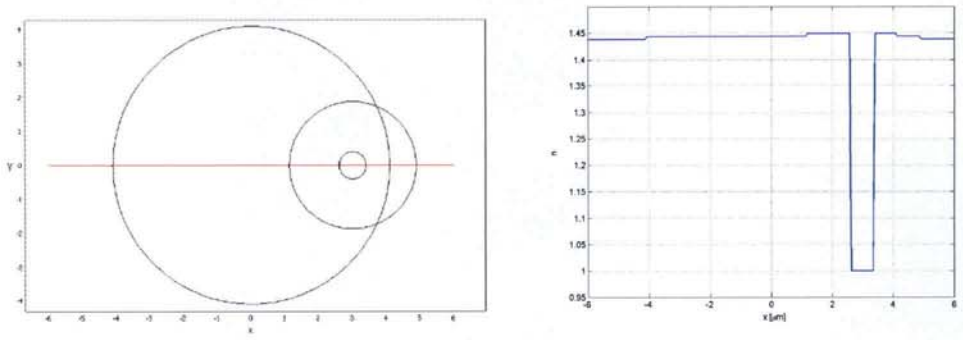

a) b)

Figure 4.8: a) Fs-inscribed structure in the core and cladding of SMF-28e composed of a void and a homogeneous index change around it. Axes are in μm. b) Refractive index profile of this structure.

tal data, [97]. The result of the last was the relation $R_v[\text{nm}] = l\sqrt[3]{E_p[\text{nJ}]}$, where $l \approx 32$ was the fitting parameter.

Birefringence

The birefringence of the perturbed fibre was calculated for different values of R_v and dn and the result is shown in Fig. 4.9. It is determined mainly by the size of the void. The fact that the variation in the index change does not introduce significant variation in birefringence can be explained by the fact that the increase in the refractive index change causes the increase in birefringence but also the decrease in the radius of the densified region which has the opposite effect on birefringence.

In the FBG all birefringence comes from the perturbation of the core mode as only the forward and backward propagating core modes are involved. Fig. 4.10 shows the core modes for two cases of the perturbation: a) $R_v = 0.554$, $dn = 8 \cdot 10^{-3}$ and b) $R_v = 0.6$, $dn = 2 \cdot 10^{-3}$. The distribution of the mode power is distorted compared to the core mode of the unperturbed SMF since the light tends to propagate through the region with the higher refractive index. The linear polarisation is not affected much and we call these modes quasi LP.

As an LPG couples a core mode to a resonant cladding mode, the birefringence of both modes has an effect on the birefringence of the grating. The impact of the perturbation on the cladding modes depends on the extrusion of the mode profile to the core, so that the cladding

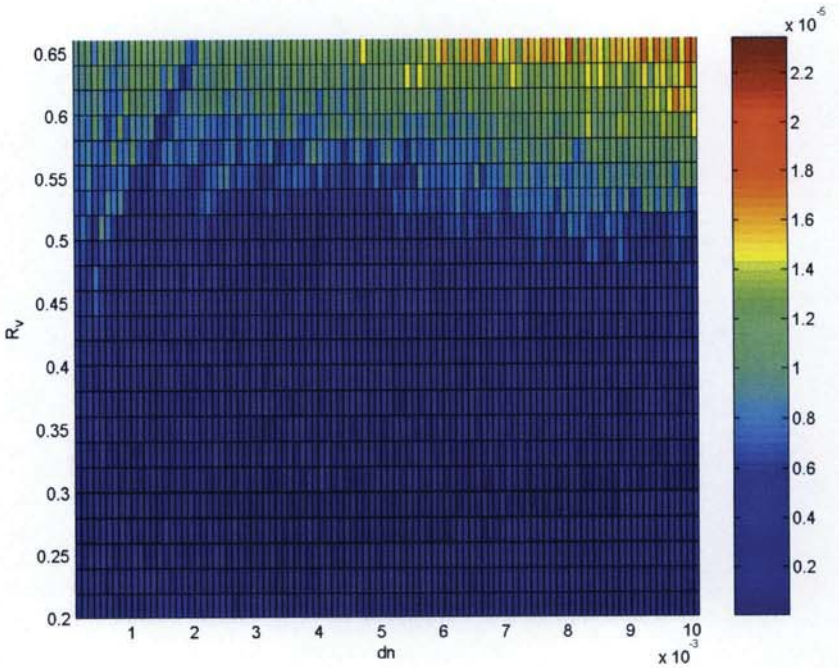

Figure 4.9: Birefringence of the fibre with a void of the radius R_v surrounded by the constant index change dn.

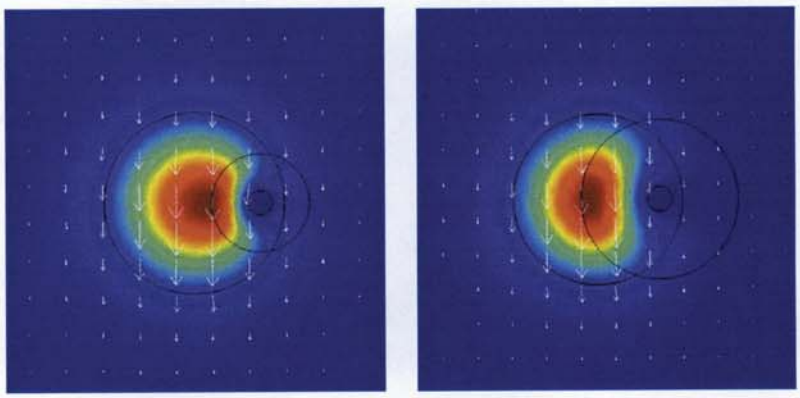

a) b)

Figure 4.10: Core modes of the birefringent fs-inscribed grating in SMF-28e modelled as a void of the radius R_v surrounded by a region of densified material with the index change dn. a) $R_v = 0.55\mu$m, $dn = 8 \cdot 10^{-3}$.b) $R_v = 0.6\mu$m, $dn = 2 \cdot 10^{-3}$. The maximal power is shown in red.

modes with the field concentrated far from the core are barely affected and vice versa. An example of the quasi LP mode is given in Fig. 4.11a). The asymmetry and the spread of the grating into the cladding enabled coupling to more cladding modes than is possible in the symmetric grating, e.g. the mode in Fig. 4.11b).

As the core – cladding mode coupling occurs in the densified region around the void, asym-

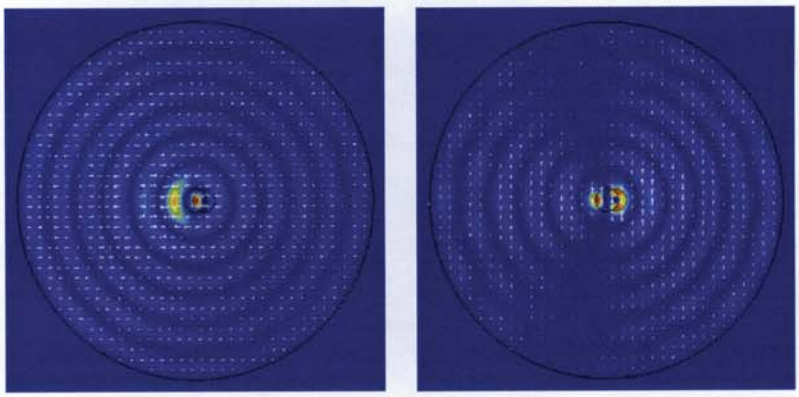

a) b)

Figure 4.11: Cladding modes of the birefringent fs-inscribed grating in SMF-28e modelled as a void of the radius $R_v = 0.6\mu$m surrounded by a region of densified material with the index change $dn = 2 \cdot 10^{-3}$. The maximal power is shown in red.

metric cladding modes whose power is predominantly in this region are the most likely to be resonant. The birefringence of these modes is of the same order as the birefringence of the core mode. For example, the mode from Fig. 4.11b) and the same y-polarised mode have birefringence $1.64 \cdot 10^{-6}$ and the corresponding core modes $5.72 \cdot 10^{-6}$.

4.2.5 Model of the Index Change Observed in Experiments

The model from the previous section can be improved by taking into account the nonuniform distribution of the material pushed out from the void. From the experimental results in Fig. 3.5b) it can be seen that the index decreases with the distance from the void. In the model we approximate the index change in the void by a constant and outside of the void by a linearly decreasing profile, as in Fig. 4.12. Improvement is at the expense of introducing a new parameter into the model, because now there are three parameters: the radius of the void R_v, the index change in the void dn_{void} and the maximal index change outside the void dn_p^{max}. The term 'void' is not adequate any more but it is kept to stay consistent with the previous sections. The radius of the perturbation is obtained in the same way as in the previous section, but with a small mathematical twist. Namely, the dependance of the refractive index and therefore the density in the region around the void on the distance from the void,

combined with the law of the conservation of mass resulted in the cubic equation for R_p. Analytical solution as a function of three parameters was obtained by Mathematica 4.0.

The mode profiles obtained from the new model and the effect of the change in R_v on the

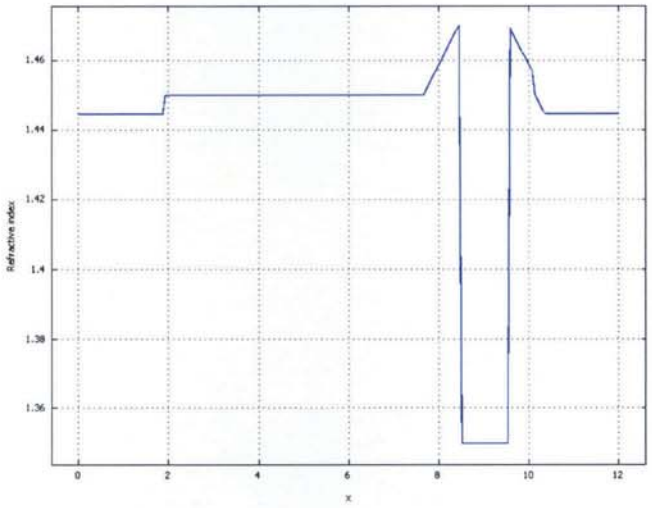

Figure 4.12: Model of the index profile that corresponds to the phase profile from Fig. 3.5b)

birefringence did not differ much from the results obtained for the constant index change. Thus the attention was paid on the effect of the decrease in the refractive index around the void and, more importantly, on the incomplete depletion of the void region. Indeed, Figs. 4.13 and 4.14 show that the index change in the void has much bigger impact on the birefringence than the index change around the void. For larger changes in the refractive index of the void, i.e. smaller refractive indices of the void, Fig. 4.13, and for larger void diameters, Fig. 4.14, an increase in the birefringence with the increase in the maximal refractive index change around the void is notable but the more striking effect is an oscillation with the maximum of the positive index change present for any parameters of the void. The reason can be found in the hypothesis of the conservation of mass and the explanation is the same as in the previous section.

The values of the birefringence of the core modes are in the same range as those in the model with the constant index change. Therefore, the improvement introduced in this model is not relevant for the study of birefringence. However, the more detailed index profiling can be a good basis for the models incorporating actual distribution of the stresses around the void.

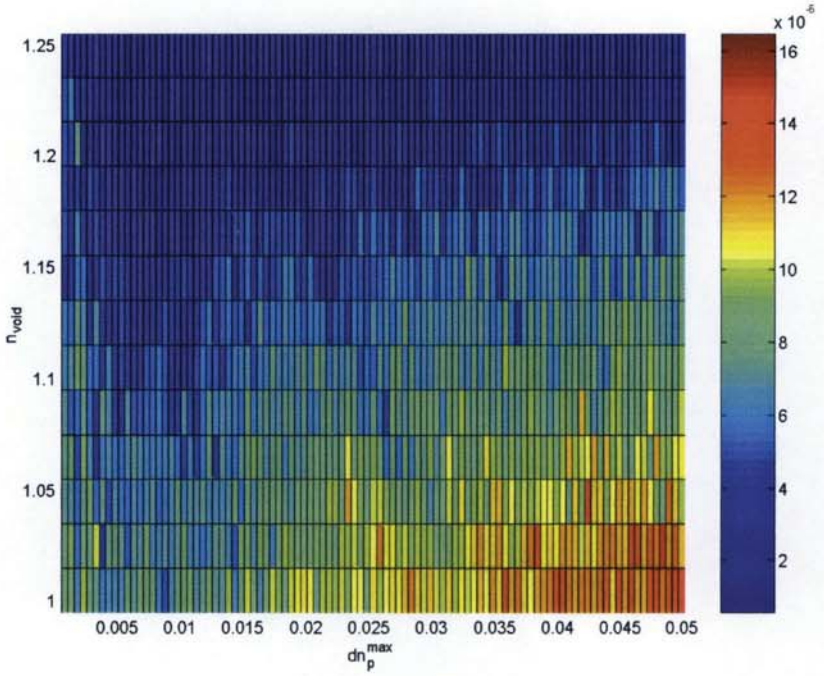

Figure 4.13: Birefringence of the grating with the fixed void radius $R_v = 0.55\mu$m as a function of the refractive index of the void n_v and the maximal index change around it dn_p^{max}.

4.2.6 Limitations of the Model

The first two models assume that the void does not contain any material and take its refractive index to be 1 which violates the proposition made at the beginning that the eigenmodes are calculated for the fibre with the index change averaged along the grating. This problem is easily fixed by introducing the index of the void as parameter in the same manner as in the last model. The index change is calculated based on the conservation of the mass and the Lorenz-Lorentz equation where the index change was ascribed to the densification only. The major contribution neglected is the contribution of the stresses that occur due to the high pressure of the plasma and the resolidification of the material. The comprehensive study of the thermal annealing of the grating [71] should help to get a better understanding of the distribution of stresses and therefore the index change. The model can be relatively easily extended to include the impact of stresses by the use of the structural module of Comsole. These refinements imply the increase in the number of parameters which complicates fitting

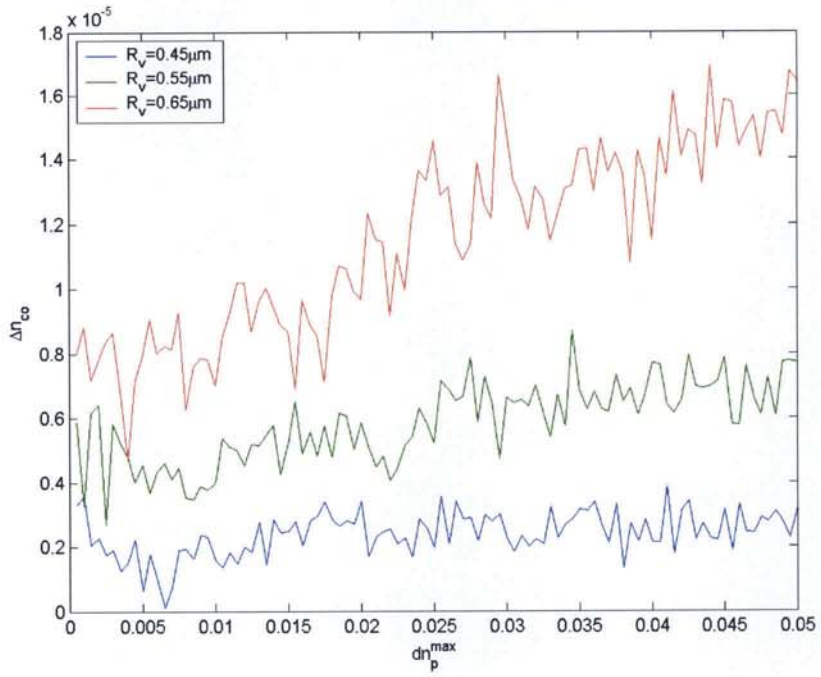

Figure 4.14: Birefringence of the grating with the change in the refractive index of the void dn_{void}=0.3, as a function of the maximal index change around the void dn_p^{max} and the void radius R_v as parameter.

to the experimental data and distinguishing the influence of different parameters of the index profile on the grating spectrum as well as the influence of the parameters of the inscription set-up on the index profile of the grating.

The refinement introduced in the first model which considers the ellipticity of the index change can be implemented in the other two models. However, this renders a cumbersome equation for the perturbation radius that significantly complicates the model. Alternatively the rough estimate of the dimensions of the index change can be obtained from the parameters of the beam: the beam waist and the Rayleigh distance.

An important intrinsic limitation of the model is its inability to treat structures inscribed by multiple single shots. Indeed, each half a period of an LPG is inscribed as a waveguide by launching the train of the single pulses into the fibre while translating the fibre in the direction perpendicular to the direction of the pulse propagation, whereby the translation speed of the sample and the pulse repetition rate are adjusted so that the continuous trace is obtained. The resultant index change is not the index change caused by the single shot any more but the result of overlapping such changes. If the pulse repetition rate is below 1MHz, every next

pulse will interact with the changed material. For the higher repetition rates, the thermal diffusion of the excited electrons will not be finished when the next pulse arrives which results in an accumulative process. This is the most serious drawback of the model and, currently, the only solution is to obtain the input index profile from the experimental data.

4.3 Applications of the Model to Grating Design and the Study of Femtosecond Inscription

Assuming that the experiment has been done to inscribe gratings under systematically changed conditions, e.g. changing energy of the pulse while keeping other parameters constant, and measuring their spectral characteristics, it would be possible to use the models developed here to retrieve the index profile of the grating. This method is not intrusive as the inscribed structures are not exposed to changes during the characterisation, such as those caused by chemical etching. On the other hand it is limited to the investigation of the grating-like index changes.

The optimal set of parameters of the index profile is obtained as the one that gives the best fit to the measured resonant wavelengths. The solution for the FBG is much easier than for the LPG since in the last case the resonant cladding mode is not known a priori and has to be determined as the one that gives the best solution. Indeed, the major drawback of the procedure is that there may be several very good fits for different combinations of the parameters. Additional information needed to determine the right solution can be read from the spectrum, for instance the spectral width or the strength of the grating. In the case of FBG, in which all the birefringence comes from the core mode, the diagrams such as those in Figs. 4.9 and 4.13 can be used to reduce the pool of possible combinations of parameters and therefore significantly speed up the computation.

We demonstrate this method on an example of the FBG reported in [15]. The model from Sec. 4.2.4 was used to retrieve the values of the void radius and the constant index change around the void by finding the best fit to the given resonant wavelength of the birefringent grating from [15]. The optimal fit gave the birefringence of $\Delta n_{co}^{eff} = 2 \cdot 10^{-5}$ for $Rv = 0.74$ and $dn = 0.023$ which was for 10^{-5} smaller than the birefringence reported in

the experiment, $\Delta n_{co}^{eff} = 3.2 \cdot 10^{-5}$. This error corresponds to the sum of the errors in the calculated resonant wavelengths which was around 10 pm, but also to the resolution of the optical spectrum analyser with which the resonant wavelengths were measured. The FBGs had relatively wide spectra of 100 nm at the half maximum without clearly defined minima which was another possible source of error. On the numerical side, in order to keep the number of fitting parameters small, we used the simplified model with the constant index change, Sec. 4.2.4. The void radius was slightly bigger than expected from the measurements of similar gratings [96] and the index change was considerably higher. It was concluded that the suggested model can be used to trace back the parameters of the refractive index change, but that the additional contributions to the grating birefringence such as elliptical shape in the cross section, nonuniform index change in the void, stresses, etc. should be included in order to obtain accurate index profile.

If the problem is posed differently so that the main objective is to obtain a particular grating, already existing models of the index change versus inscription parameters can be used, e.g. the dependency of the void radius on the pulse energy $R_v[\text{nm}] = const\sqrt[3]{E_p[\text{nJ}]}$, [97]. As the empirical models are approximate and based on particular experimental set-ups, they cannot be used for the general design of grating spectra but they can give valuable information on the trends in the grating behaviour. As discussed in Chapter 3, the comprehensive theoretical model does not exist yet. The model suggested above combined with the series of the experimental data enables mapping of the inscription parameters into the parameters of the induced refractive index change via the grating spectrum. Although it does not explain physical mechanisms of index change it is sufficient for the engineering applications such as the grating design.

4.4 Conclusions

Based upon the state-of-the-art theoretical and experimental picture of the femtosecond inscription a generic model of the index profile of the fibre gratings fabricated point-by-point the femtosecond laser pulses has been established. The model is automated to retrieve the parameters of the assumed index profile from the grating spectrum, whereby the birefrin-

gence of the grating can be used to increase the efficiency. However, despite of our efforts we could not find a sufficient number of measurements of the index profile of the grating to fully justify the model. This work is under way and is related to the joint theoretical and experimental efforts described in the previous chapter. It is also the complement of this studies as it allow for the investigation of the influence of the inscription parameters on the induced refractive index change, which is not easy by the direct measurements due to the restricted accessibility of the single shot inscribed in-bulk structures. The major problem that may be encountered in the index profiling of the gratings, in particular of the LPGs, is the existence of the several satisfactory solutions in which case an additional comparison with the spectrum or the other grating properties is needed. The model does not consider cumulative refractive index change produced by the irradiation by the several laser pulses. Apart from this, the model is generic as it allows for various modifications, such as addition of stresses or the changes in the shape of the index change, which means that in combination with the experiments typical of fibre gratings, for instance the thermal annealing or the straining of the fibre prior to the inscription, it should give better understanding of the nature of the index change.

Chapter 5

Conclusion

The study of the LPGs in PCFs was application driven where the major application was the thermally stable sensor of strain, refractive index and bending which also can withstand the time and annealing. Such behaviour of the grating was explained and a method for calculation of the induced refractive index change based on the grating spectra was offered. The simplifications assumed in the model and both the numerical and the experimental errors slightly deteriorated the results.

The processes involved in the femtosecond inscription were investigated and a relation between the permanent refractive index change and the distribution of the electron plasma that was created due to the multiphoton ionisation by the femtosecond pulse was established. The experimental results showed that the lifetime of the structures written by high energy femtosecond pulses should be measured in years. They were also used to find the dependency of the inscription threshold and the profile of the index change on the pulse energy. By using the sophisticated code for the adaptive mesh refinement the formation of the subwavelength plasma islands that may lead to the subwavelength index changes in the medium with high Kerr nonlinearity was predicted. This was applied to modelling of the birefringent fibre gratings inscribed by the femtosecond laser.

x x x x x x

How far have we gone from the fact?

Further than the modeller wanted and not far enough for the physicist.

In conclusion, it is the time to move on, to become a physicist.

References

[1] K.O. Hill, Y. Fujii, D.C. Johnson, and B.S. Kawasaki. Photosensitivity in optical fibre waveguides: Application to reflection filter fabrication. *Applied Physics Letters*, 32(10):647 – 9, 1978.

[2] I. Bennion, J.A.R. Williams, L. Zhang, K. Sugden, and N.J. Doran. UV-written in-fibre Bragg gratings. *Optical and Quantum Electronics*, 28(2):93 – 135, 1996.

[3] Ashish M. Vengsarkar, Paul J. Lemaire, Justin B. Judkins, Vikram Bhatia, Turan Erdogan, and John E. Sipe. Long-period fiber gratings as band-rejection filters. *Journal of Lightwave Technology*, 14(1):58 – 65, 1996.

[4] C. Narayanan, H.M. Presby, and A.M. Vengsarkar. Band-rejection fibre filter using periodic core deformation. *Electronics Letters*, 33(4):280 – 1, 1997.

[5] R. Kashyap. *Fiber Bragg Gratings*. Academic Press, 1999.

[6] G. Kakarantzas, T.A. Birks, and P.St.J. Russell. Structural long-period gratings in photonic crystal fibers. *Optics Letters*, 27(12):1013 – 15, 2002.

[7] Yinian Zhu, Ping Shum, Joo-Hin Chong, Chao Lu, and M.K. Rao. Deep-notch, ultracompact long-period grating in a large-mode-area photonic crystal fiber. *Optics Letters*, 28(24):2467 – 2469, 2003.

[8] Jong H. Lim, Hyun S. Jang, Kyung S. Lee, Jin C. Kim, and Byeong H. Lee. Mach-zehnder interferometer formed in a photonic crystal fiber based on a pair of long-period fiber gratings. *Optics Letters*, 29(4):346 – 348, 2004.

[9] B.J. Eggleton, P.S. Westbrook, R.S. Windeler, S. Spalter, and T.A. Strasser. Grating resonances in air-silica microstructured optical fibers. *Optics Letters*, 24(21):1460, 1999.

[10] H. Dobb, K. Kalli, and D.J. Webb. Temperature-insensitive long period grating sensors in photonic crystal fibre. *Electronics Letters*, 40(11):657 – 658, 2004.

[11] G. Rego, J.C.C. Carvalho, P.V.S. Marques, A. Fernandez Fernandez, F. Durr, and H.G. Limberger. Stress profiling of arc-induced long-period gratings written in pure-silica-core fibers. *Proceedings of SPIE - The International Society for Optical Engineering*, 5855 PART II:884 – 887, 2005.

[12] G. Humbert, A. Malki, S. Fevrier, P. Roy, and D. Pagnoux. Electric arc-induced long-period gratings in Ge-free air-silica microstructure fibres. *Electronics Letters*, 39(4):349 – 50, 2003.

[13] K. Morishita and Y. Miyake. Fabrication and resonance wavelengths of long-period gratings written in a pure-silica photonic crystal fiber by the glass structure change. *Journal of Lightwave Technology*, 22(2):625 – 30, 2004.

[14] Stephen J. Mihailov, Christopher W. Smelser, Dan Grobnic, Robert B. Walker, Ping Lu, Huimin Ding, and James Unruh. Bragg gratings written in AlSiO2 and Ge-Doped core fibers with 800nm femtosecond radiation and a phase mask. *Journal of Lightwave Technology*, 22(1):94 – 100, 2004.

[15] A. Martinez, M. Dubov, I. Khrushchev, and I. Bennion. Direct writing of fibre Bragg gratings by femtosecond laser. *Electronics Letters*, 40(19):1170 – 2, 2004.

[16] Sarfraz Khaliq, Stephen W. James, and Ralph P. Tatam. Fiber-optic liquid-level sensor using a long-period grating. *Optics Letters*, 26(16):1224 – 1226, 2001.

[17] Vikram Bhatia, David Campbell, Richard O. Claus, and Ashish M. Vengsarkar. Simultaneous strain and temperature measurement with long-period gratings. *Optics Letters*, 22(9):648, 1997.

[18] G. Rego, P.V.S. Marques, H.M. Salgado, and J.L. Santos. Simultaneous measurement of temperature and strain based on arc-induced long-period fibre gratings. *Electronics Letters*, 41(2):60 – 62, 2005.

[19] C.C. Ye, S.W. James, and R.P. Tatam. Simultaneous temperature and bend sensing with long-period fiber gratings. *Optics Letters*, 25(14):1007 – 1009, 2000.

[20] V. Bhatia, D.K. Campbell, D. Sherr, T.G. D'Alberto, N.A. Zabaronick, G.A. Ten Eyck, K.A. Murphy, and R.O. Claus. Temperature-insensitive and strain-insensitive long-period grating sensors for smart structures. *Optical Engineering*, 36(7):1872 – 6, 1997.

[21] L. Qin, Z.X. Wei, Q.Y. Wang, H.P. Li, W. Zheng, Y.S. Zhang, and D.S. Gao. Compact temperature-compensating package for long-period fiber gratings. *Optical Materials*, 14(3):239 – 42, 2000.

[22] B.A.L. Gwandu, X. Shu, T.D.P. Allsop, W. Zhang, L. Zhang, D.J. Webb, and I. Bennion. Simultaneous refractive index and temperature measurement using cascaded long-period grating in double-cladding fibre. *Electronics Letters*, 38(14):695 – 6, 2002.

[23] H. Dobb, K. Kalli, and D.J. Webb. Measured sensitivity of arc-induced long-period grating sensors in photonic crystal fibre. *Optics Communications*, 260(1):184 – 191, 2006.

[24] Xianfeng Chen, Kaiming Zhou, Lin Zhang, and I. Bennion. Optical chemsensor based on etched tilted Bragg grating structures in multimode fiber. *IEEE Photonics Technology Letters*, 17(4):864 – 6, 2005.

[25] Joy P. Dunkers, Joseph L. Lenhart, Sylvia R. Kueh, John H. van Zanten, Suresh G. Advani, and Richard S. Parnas. Fiber optic flow and cure sensing for liquid composite molding. *Optics and Lasers in Engineering*, 35(2):91 – 104, 2001.

[26] Matthew P. Delisa, Zheng Zhang, Mira Shiloach, Saeed Pilevar, Christopher C. Davis, James S. Sirkis, and William E. Bentley. Evanescent wave long-period fiber Bragg grating as an immobilized antibody biosensor. *Analytical Chemistry*, 72(13):2895 – 2900, 2000.

[27] N.D. Rees, S.W. James, R.P. Tatam, and G.J. Ashwell. Optical fiber long-period gratings with Langmuir-Blodgett thin-film overlays. *Optics Letters*, 27(9):686 – 8, 2002.

[28] S.W. James and R.P. Tatam. Optical fibre long-period grating sensors: characteristics and application. *Measurement Science and Technology*, 14(5):49 – 61, 2003.

[29] A. Diez, T.A. Birks, W.H. Reeves, B.J. Mangan, and P.St.J. Russell. Excitation of cladding modes in photonic crystal fibers by flexural acoustic waves. *Optics Letters*, 25(20):1499 – 1501, 2000.

[30] A.W. Snyder and J.D. Love. *Optical Waveguide Theory*. Kluwer Academic Publishers, 2000.

[31] M. Born and E. Wolf. *Principles of Optics*. Cambridge University Press, 7th edition, 2000.

[32] Turan Erdogan. Cladding-mode resonance in short- and long-period fiber grating filters. *Journal of the Optical Society of America A: Optics and Image Science, and Vision*, 14(8):1760 – 1773, 1997.

[33] A. Yariv. *Optical Electronics in Modern Communications*. Oxford University Press, 5th edition, 1997.

[34] H. Friedel, R. Grauer, and C. Marliani. Adaptive mesh refinement for singular current sheets in incompressible magnetohydrodynamic flows. *Journal of Computational Physics*, 134(1):190 – 8, 1997.

[35] E. Yablonovitch. Inhibited spontaneous emission in solid-state physics and electronics. *Physical Review Letters*, 58(20):2059 – 62, 1987.

[36] P. Russell. Applied physics: Photonic crystal fibers. *Science*, 299(5605):358 – 362, 2003.

[37] Jonathan Knight, Tim Birks, Brian Mangan, and Philip St. James Russell. Photonic crystal fibers new solutions in fiber optics. *Optics and Photonics News*, 13(3):26 – 30, 2002.

[38] T.A. Birks, J.C. Knight, and P. St. J. Russell. Endlessly single-mode photonic crystal fiber. *Optics Letters*, 22(13):961 – 963, 1997.

[39] Crystal fibre. *http://www.crystal-fibre.com*.

[40] J.C. Knight, T.A. Birks, P.St.J. Russell, and D.M. Atkin. All-silica single-mode optical fiber with photonic crystal cladding. *Optics Letters*, 21(19):1547 – 1549, 1996.

[41] Georges Humbert and Abdelrafik Malki. Characterizations at very high temperature of electric arc-induced long-period fiber gratings. *Optics Communications*, 208(4-6):329 – 335, 2002.

[42] Georges Humbert and Abdelrafik Malki. Electric-arc-induced gratings in non-hydrogenated fibres: Fabrication and high-temperature characterizations. *Journal of Optics A: Pure and Applied Optics*, 4(2):194 – 198, 2002.

[43] G. Rego, R. Falate, J.L. Santos, H.M. Salgado, J.L. Fabris, S.L. Semjonov, and E.M. Dianov. Arc-induced long-period gratings in aluminosilicate glass fibers. *Optics Letters*, 30(16):2065 – 7, 2005.

[44] G. Rego, P.V.S. Marques, J.L. Santos, and H.M. Salgado. Arc-induced long-period gratings. *Fiber and Integrated Optics*, 24(3-4):245 – 59, 2005.

[45] Fitel. *http://www.fitel.com.*

[46] G. Rego, O. Okhotnikov, E. Dianov, and V. Sulimov. High-temperature stability of long-period fiber gratings produced using an electric arc. *Journal of Lightwave Technology*, 19(10):1574 – 1579, 2001.

[47] J. S. Petrovic, D. J. Webb, H. Dobb, V. Mezentsev, K. Kalli, and I. Bennion. Nondestructive index profiling of the long period gratings in photonic crystal fibres. *accepted for publication in Optical and Quantum Electronics.*

[48] Yinian Zhu, Ping Shum, Joo-Hin Chong, M.K. Rao, and Chao Lu. Deep-notch and ultra-compact long-period grating in large-mode-area photonic crystal fiber. *Conference on Lasers and Electro-Optics (CLEO)*, vol.1:4 pp. vol.1, 2004.

[49] M.D. Nielsen, G. Vienne, J.R. Folkenberg, and A. Bjarklev. Investigation of microdeformation-induced attenuation spectra in a photonic crystal fiber. *Optics Letters*, 28(4):236 – 8, 2003.

[50] Xuewen Shu, Lin Zhang, and Ian Bennion. Fabrication and characterisation of ultra-long-period fibre gratings. *Optics Communications*, 203(3-6):277 – 281, 2002.

[51] Wang Zhi, Ju Jian, W. Jin, and K.S. Chiang. Scaling property and multi-resonance of PCF-based long period gratings. *Optics Express*, 12(25), 2004.

[52] Crystal Fibre A/S. Information obtained at the CLEO 2005 exhibit.

[53] A. Ferrando, E. Silvestre, J.J. Miret, P. Andres, and M.V. Andres. Full-vector analysis of a realistic photonic crystal fiber. *Optics Letters*, 24(5):276 – 278, 1999.

[54] Wang Zhi, Ren Guobin, Lou Shuqin, and Jian Shuisheng. Supercell lattice method for photonic crystal fibers. *Optics Express*, 11(9), 2003.

[55] T.P. White, B.T. Kuhlmey, R.C. McPhedran, D. Maystre, G. Renversez, C.M. de Sterke, and L.C. Botten. Multipole method for microstructured optical fibers. I. Formulation. *Journal of the Optical Society of America B (Optical Physics)*, 19(10):2322 – 30, 2002.

[56] Boris T. Kuhlmey, Thomas P. White, Gilles Renversez, Daniel Maystre, Lindsay C. Botten, C. Martijn De Sterke, and Ross C. McPhedran. Multipole method for microstructured optical fibers. II. Implementation and results. *Journal of the Optical Society of America B: Optical Physics*, 19(10):2331 – 2340, 2002.

[57] N.A. Issa and L. Poladian. Vector wave expansion method for leaky modes of microstructured optical fibers. *Journal of Lightwave Technology*, 21(4):1005 – 12, 2003.

[58] F. Fogli, L. Saccomandi, P. Bassi, G. Bellanca, and S. Trillo. Full vectorial BPM modeling of index-guiding photonic crystal fibers and couplers. *Optics Express*, 10(1), 2002.

[59] K. Saitoh and M. Koshiba. Full-vectorial imaginary-distance beam propagation method based on a finite element scheme: Application to photonic crystal fibers. *IEEE Journal of Quantum Electronics*, 38(7):927 – 933, 2002.

[60] Chin-Ping Yu and Hung-Chun Chang. Applications of the finite difference mode solution method to photonic crystal structures. *Optical and Quantum Electronics*, 36(1-3):145 – 163, 2004.

[61] F. Brechet, J. Marcou, D. Pagnoux, and P. Roy. Complete analysis of the characteristics of propagation into photonic crystal fibers by the finite element method. *Optical Fiber Technology: Materials, Devices and Systems*, 6(2):181 – 91, 2000.

[62] A. Cucinotta, S. Selleri, L. Vincetti, and M. Zoboli. Holey fiber analysis through the finite-element method. *IEEE Photonics Technology Letters*, 14(11):1530 – 1532, 2002.

[63] Comsol. *http://www.comsol.com.*

[64] P.R. McIsaac. Symmetry-induced modal characteristics of uniform waveguides. I summary of results. *IEEE Transactions on Microwave Theory and Techniques*, MTT-23(5):421 – 9, 1975.

[65] P.R. McIsaac. Symmetry-induced modal characteristics of uniform waveguides. II theory. *IEEE Transactions on Microwave Theory and Techniques*, MTT-23(5):429 – 33, 1975.

[66] Zhaoming Zhu and T.G. Brown. Full-vectorial finite-difference analysis of microstructured optical fibers. *Optics Express*, 10(17), 2002.

[67] W.P. Huang and C.L. Xu. Simulation of three-dimensional optical waveguides by a full-vector beam propagation method. *IEEE Journal of Quantum Electronics*, 29(10):2639 – 49, 1993.

[68] The University of Sydney ARC Centre of Excellence-Ultrahigh-bandwidth Devices for Optical Systems, School of Physics. *http://www.physics.usyd.edu.au/cudos/mofsoftware/.*

[69] J. D. Joannopoulos, R. D. Meade, and J. N. Winn. *Photonic Crystals: Molding the Flow of Light.* Princeton University Press, 1995.

[70] H.P. Uranus and H.J.W.M. Hoekstra. Modelling of microstructured waveguides using a finite-element-based vectorial mode solver with transparent boundary conditions. *Optics Express*, 12(12):2795 – 2809, 2004.

[71] T.D.P. Allsop, M. Dubov, H. Dobb, A. Main, A. Martinez, K. Kalli, D.J. Webb, and I. Bennion. A comparison of the spectral properties of high temperature annealed long period gratings inscribed by fs laser, uv and fusion-arc. *Photonics Europe 2006 (SPIE)*, pages 6193–14, 2006.

[72] Turan Erdogan. Fiber grating spectra. *Journal of Lightwave Technology*, 15(8):1277 – 1294, 1997.

[73] Xuewen Shu, Lin Zhang, and Ian Bennion. Sensitivity characteristics of long-period fiber gratings. *Journal of Lightwave Technology*, 20(2):255 – 266, 2002.

[74] H.J. Patrick, A.D. Kersey, and F. Bucholtz. Analysis of the response of long period fiber gratings to external index of refraction. *Journal of Lightwave Technology*, 16(9):1606 – 12, 1998.

[75] Byeong Ha Lee, Yu Liu, Sang Bae Lee, Sang Sam Choi, and Joo Nyung Jang. Displacements of the resonant peaks of a long-period fiber grating induced by a change of ambient refractive index. *Optics Letters*, 22(23):1769 –1771, 1997.

[76] Robert Guenther. *Modern Optics*. 1990.

[77] G.B. Hocker. Fiber-optic sensing of pressure and temperature. *Applied Optics*, 18(9):1445 – 8, 1979.

[78] Solid works. *http://www.solidworks.com.*

[79] Govind P. Agrawal. *Nonlinear Fibre Optics*. Academic Press, 3rd edition, 2001.

[80] T. Allsop, M. Dubov, A. Martinez, F. Floreani, I. Khrushchev, D.J. Webb, and I. Bennion. Directional bend sensor based on an asymmetric modification of the fiber cladding by femtosecond laser. *2005 Conference on Lasers and Electro-Optics, CLEO*, 3:2179 – 2181, 2005.

[81] A. Peyrilloux, T. Chartier, A. Hideur, L. Berthelot, G. Melin, S. Lempereur, D. Pagnoux, and P. Roy. Theoretical and experimental study of the birefringence of a photonic crystal fiber. *Journal of Lightwave Technology*, 21(2):536 – 539, 2003.

[82] In-Kag Hwang, Yong-Jae Lee, and Yong-Hee Lee. Birefringence induced by irregular structure in photonic crystal fiber. *Optics Express*, 11(22), 2003.

[83] K.L. Reichenbach and C. Xu. The effects of randomly occurring nonuniformities on propagation in photonic crystal fibers. *Optics Express*, 13(8), 2005.

[84] Brent L. Bachim and Thomas K. Gaylord. Polarization-dependent loss and birefringence in long-period fiber gratings. *Applied Optics*, 42(34):6816 – 6823, 2003.

[85] R. Osellame, S. Taccheo, M. Marangoni, R. Ramponi, P. Laporta, D. Polli, S. De Silvestri, and G. Cerullo. Compression of amplified chirped opical pulses. *Optics Communications*, 56:219, 1985.

[86] Govind P. Agrawal. *Applications of Nonlinear Fibre Optics*. 2001.

[87] Wataru Watanabe, Taishi Asano, Kazuhiro Yamada, Kazuyoshi Itoh, and Junji Nishii. Wavelength division with three-dimensional couplers fabricated by filamentation of femtosecond laser pulses. *Optics Letters*, 28(24):2491 – 2493, 2003.

[88] E. N. Glezer, M. Milosavljevic, L. Huang, R. J. Finlay, T. Her, J. Paul Callan, and E. Mazur. Three-dimensional optical storage inside transparent materials. *Opt. Lett.*, 21:2023–2025, 1996.

[89] R. Osellame, S. Taccheo, M. Marangoni, R. Ramponi, P. Laporta, D. Polli, S. De Silvestri, and G. Cerullo. Femtosecond writing of active optical waveguides with astigmatically shaped beams. *Journal of the Optical Society of America B (Optical Physics)*, 20(7):1559 – 67, 2003.

[90] Christopher W. Smelser, Stephen J. Mihailov, and Dan Grobnic. Formation of type I-IR and type II-IR gratings with an ultrafast IR laser and a phase mask. *Optics Express*, 13(14):5377 – 5386, 2005.

[91] A. Dubietis, G. Tamosauskas, I. Diomin, and A. Varanavicius. Self-guided propagation of femtosecond light pulses in water. *Optics Letters*, 28(14):1269 – 71, 2003.

[92] M. Kolesik, E.M. Wright, and J.V. Moloney. Dynamic nonlinear X waves for femtosecond pulse propagation in water. *Physical Review Letters*, 92(25 I):253901 – 1, 2004.

[93] X.R. Zhang, X. Xu, and A.M. Rubenchik. Simulation of microscale densification during femtosecond laser processing of dielectric materials. *Applied Physics A (Materials Science Processing)*, A79(4-6):945 – 8, Sept.-Oct. 2004.

[94] A. Barty, K.A. Nugent, D. Paganin, and A. Roberts. Quantitative optical phase microscopy. *Optics Letters*, 23(11):817 – 19, 1998.

[95] A. Roberts, E. Ampem-Lassen, A. Barty, K.A. Nugent, G.W. Baxter, N.M. Dragomir, and S.T. Huntington. Refractive-index profiling of optical fibers with axial symmetry by use of quantitative phase microscopy. *Optics Letters*, 27(23):2061 – 3, 2002.

[96] A. Martinez, M. Dubov, I. Khrushchev, and I. Bennion. Structure of fibre gratings directly written by infrared femtosecond laser. *2006 Conference on Lasers and Electro-Optics, CLEO*, page JTuD13, 2006.

[97] S. Juodkazis, K. Nishimura, S. Tanaka, H. Misawa, E.G. Gamaly, B. Luther-Davies, L. Hallo, P. Nicolai, and V.T. Tikhonchuk. Laser-induced microexplosion confined in the bulk of a sapphire cystal: Evidence of multimegabar pressures. *Physical Review Letters*, 96(16):166101, 2006.

[98] L. Sudrie, M. Franco, B. Prade, and A. Mysyrowicz. Study of damage in fused silica induced by ultra-short IR laser pulses. *Optics Communications*, 191(3-6):333 – 339, 2001.

[99] J.H. Marburger. Self-focusing: theory. *Progress in Quantum Electronics*, 4:35 – 110, 1975.

[100] W.L. Smith, J.H. Bechtel, and N. Bloembergen. Picosecond laser-induced breakdown at 5321 and 3547 a: Observation of frequency-dependent behaviour. *Physical Review B (Solid State)*, 15(8):4039 – 55, 1977.

[101] Nicholaas Bloembergen. Laser-induced electronic breakdown in solids. *IEEE Journal of Quantum Electronics*, QE-10(3):375 – 386, 1974.

[102] D. Arnold and E. Cartier. Theory of laser-induced free-electron heating and impact ionization in wide-band-gap solids. *Physical Review B (Condensed Matter)*, 46(23):15102 – 15, 1992.

[103] T.W. Hänsch. Passion for precision. *Nobel Lecture*, 2005.

[104] Detao Du, X. Liu, Jeff A. Squier, and Gerard A. Mourou. Laser-induced breakdown as a function of pulse duration: from 7 ns to 150 fs. *Proceedings of SPIE - The International Society for Optical Engineering*, 2428:422 – 434, 1995.

[105] Q. Feng, J.V. Moloney, A.C. Newell, E.M. Wright, K. Cook, P.K. Kennedy, D.X. Hammer, B.A. Rockwell, and C.R. Thompson. Theory and simulation on the threshold of water breakdown induced by focused ultrashort laser pulses. *IEEE Journal of Quantum Electronics*, 33(2), 1997.

[106] K.D. Moll, A.L. Gaeta, and G. Fibich. Self-similar optical wave collapse: observation of the Townes profile. *Physical Review Letters*, 90(20):203902 – 1, 2003.

[107] Alexander L. Gaeta, Gadi Fibich, and K.D. Moll. Self-similar optical wave collapse: Observation of the Townes profile. *Physical Review Letters*, 90(20):203902 – 1, 2003.

[108] M.D. Feit and Jr. Fleck, J.A. Effect of refraction on spot-size dependence of laser-induced breakdown. *Applied Physics Letters*, 24(4):169 – 72, 1974.

[109] J. V. Moloney and A. C. Newell. *Nonlinear Optics*. Westview Press, 2004.

[110] Dwight R. Nicholson. *Introduction to Plasma Theory*. John Wiley & Sons, 1983.

[111] R.W. Boyd. *Nonlinear Optics*. Elsevier Science, 2nd edition, 2003.

[112] T. Brabec and F. Krausz. Nonlinear optical pulse propagation in the single-cycle regime. *Physical Review Letters*, 78(17):3282 – 5, 1997.

[113] J.K. Ranka and A.L. Gaeta. Breakdown of the slowly varying envelope approximation in the self-focusing of ultrashort pulses. *Optics Letters*, 23(7), 1998.

[114] A.L. Gaeta. Catastrophic collapse of ultrashort pulses. *Physical Review Letters*, 84(16):3582 – 5, 2000.

[115] S. Tzortzakis, L. Sudrie, M. Franco, B. Prade, A. Mysyrowicz, A. Couairon, and L. Berge. Self-guided propagation of ultrashort IR laser pulses in fused silica. *Physical Review Letters*, 87(21):213902, 2001.

[116] M. Kolesik, J.V. Moloney, and M. Mlejnek. Unidirectional optical pulse propagation equation. *Physical Review Letters*, 89(28 I):283902 – 1, 2002.

[117] P. Chernev and V. Petrov. Self-focusing of light pulses in the presence of normal group-velocity dispersion. *Optics Letters*, 17(3), 1992.

[118] J.E. Rothenberg. Pulse splitting during self-focusing in normally dispersive media. *Optics Letters*, 17(8), 1992.

[119] G.G. Luther, J.V. Moloney, A.C. Newell, and E.M. Wright. Self-focusing threshold in normally dispersive media. *Optics Letters*, 19(12), 1994.

[120] G.G. Luther, A.C. Newell, and J.V. Moloney. The effects of normal dispersion on collapse events. *Physica D*, 74(1-2):59 – 73, 1994.

[121] M.J. Berger and P. Colella. Local adaptive mesh refinement for shock hydrodynamics. *Journal of Computational Physics*, 82(1):64 – 84, 1989.

[122] H. Pietsch, E.W. Laedke, and K.H. Spatschek. Nonlinear mode conversion with chaotic soliton generation at plasma resonance. *Physical Review E (Statistical Physics, Plasmas, Fluids, and Related Interdisciplinary Topics)*, 47(3), 1993.

[123] K. Germaschewski, R. Grauer, L. Berge, V.K. Mezentsev, and J. Juul Rasmussen. Splittings, coalescence, bunch and snake patterns in the 3D nonlinear Schrodinger equation with anisotropic dispersion. *Physica D*, 151(2-4):175 – 98, 2001.

[124] Hengchang Guo, Hongbing Jiang, Ying Fang, Chao Peng, Hong Yang, Yan Li, and Qihuang Gong. The pulse duration dependence of femtosecond laser induced refractive index modulation in fused silica. *Journal of Optics A: Pure and Applied Optics*, 6(8):787 – 790, 2004.

[125] J. B. Ashcom. *The role of focusing in the interaction of femtosecond laser pulses with transparent materials*. PhD thesis, Harvard University, 2003.

[126] P.J. Scully, D. Jones, and D.A. Jaroszynski. Femtosecond laser irradiation of polymethylmethacrylate for refractive index gratings. *Journal of Optics A: Pure and Applied Optics*, 5(4):92–96, 2003.

[127] A. Martinez, I.Y. Khrushchev, and I. Bennion. Direct inscription of Bragg gratings in coated fibers by an infrared femtosecond laser. *Optics Letters*, 31(11):1603 – 5, 2006.

[128] Chris B. Schaffer, Alan O. Jamison, and Eric Mazur. Morphology of femtosecond laser-induced structural changes in bulk transparent materials. *Applied Physics Letters*, 84(9):1441 – 1443, 2004.

[129] E.N. Glezer, M. Milosavljevic, L. Huang, R.J. Finlay, T.-H. Her, J.P. Callan, and E. Mazur. Three-dimensional optical storage inside transparent materials. *Optics Letters*, 21(24):2023 – 2025, 1996.

[130] Alexander M. Streltsov and Nicholas F. Borrelli. Study of femtosecond-laser-written waveguides in glasses. *Journal of the Optical Society of America B: Optical Physics*, 19(10):2496 – 2504, 2002.

[131] A. Cavalleri, K. Sokolowski-Tinten, J. Bialkowski, and D. von der Linde. Femtosecond laser ablation of gallium arsenide investigated with time-of-flight mass spectroscopy. *Applied Physics Letters*, 72(19), 1998.

[132] D. von der Linde and K. Sokolowski-Tinten. The physical mechanisms of short-pulse laser ablation. *Applied Surface Science*, 154-155:1 – 10, 2000.

[133] W.L. Barnes, A. Dereux, and T.W. Ebbesen. Surface plasmon subwavelength optics. *Nature*, 424:824 – 830, 2003.

[134] R.R. Thomson, S. Campbell, G. Brown, I.J. Blewett, A.K. Kar, and D.T. Reid. Femtosecond waveguide fabrication in bulk lithium niobate (linbo3). *2005 Conference on Lasers and Electro-Optics, CLEO*, 3:1918 – 1920, 2005.

[135] A. Martinez, I.Y. Khrushchev, and I. Bennion. Thermal properties of fibre Bragg gratings inscribed point-by-point by infrared femtosecond laser. *Electronics Letters*, 41(4):176 – 8, 2005/02/17.

[136] M. Dubov, T.D.P. Allsop, A. DMartinez, V. Mezentsev, and I. Bennion. Highly birefringent long period gratings fabricated with femtosecond laser. *Optical Fibre Communication Conference (OFC)*, 2006.

[137] D. Nykogosian. Lecture on LPGs inscribed by UV femtosecond laser at Aston University. 2005.

[138] S.T. Oh, W.T. Han, U.C. Paek, and Y. Chung. Reduction of birefringence and polarization-dependent loss of long-period fiber gratings fabricated with a krf excimer laser. *Optics Express*, 11(23):3087 – 3092, 2003.

[139] F. Hindle, E. Fertein, C. Przygodzki, F. Durr, L. Paccou, R. Bocquet, P. Niay, H.G. Limberger, and M. Douay. Inscription of long-period gratings in pure silica and Germano-silicate fiber cores by femtosecond laser irradiation. *IEEE Photonics Technology Letters*, 16(8):1861 – 3, 2004.

[140] O.M. Efimov, K. Gabel, S.V. Garnov, L.B. Glebov, S. Grantham, M. Richardson, and M.J. Soileau. Color-center generation in silicate glasses exposed to infrared femtosecond pulses. *Journal of the Optical Society of America B (Optical Physics)*, 15(1):193 – 9, 1998.

[141] Arnaud Zoubir, Martin Richardson, Lionel Canioni, Arnaud Brocas, and Laurent Sarger. Optical properties of infrared femtosecond laser-modified fused silica and application to waveguide fabrication. *Journal of the Optical Society of America B: Optical Physics*, 22(10):2138 – 2143, 2005.

Appendix A
List of Publications

1. J.S. Petrovic, V. Mezentsev, H. Dobb, D. J. Webb, K. Kalli, and I. Bennion, Multiple Period Resonances in Long Period Gratings in Photonic Crystal Fibres. *Optical and Quantum Electronics*, 38(1-3 SPEC ISS):209, 2006.

2. J. S. Petrovic, V. Mezentsev, H. Dobb, D. J. Webb, K. Kalli, and I. Bennion. Nondestructive Index Profiling of the Long Period Gratings in Photonic Crystal Fibres. To be published in *Optical and Quantum Electronics*

3. J. S. Petrovic, V. Mezentsev, H. Dobb, D. Webb, and I. Bennion. Multiple period resonances of long period gratings in photonic crystal fiber. *Conference on Lasers and Electro-Optics, CLEO*, 1:689, 2005.

4. J. S. Petrovic, V. Mezentsev, H. Dobb, D. Webb, K. Kalli, and I. Bennion. Multiple Period Resonances in the Long Period Grating in the Photonic Crystal Fibres with Bulk Cladding. *XIII International Workshop on Optical Waveguide Theory and Numerical Modelling*, Sa3-6 (2005)

5. H. Dobb, J. S. Petrovic, V. Mezentsev, D. J. Webb, and K. Kalli. Long-period gratings fabricated in photonic crystal fibre. *Proceedings of SPIE - The International Society for Optical Engineering*, (5855 PART I):334, 2005.

6. V. Mezentsev, J. Petrovic, J. Dreher, Jurgen, and R. Grauer. Adaptive modeling of the femtosecond inscription in silica. *Proceedings of SPIE - The International Society for Optical Engineering*, (6107):61070, 2006.

7. J. S. Petrovic, V. Mezentsev, H. Dobb, and D. Webb. Dynamics of the Long Period Grating in the Photonic Crystal Fibre with Bulk Cladding. *Proceedings of the XV International Workshop on Optical Waveguide Theory and Numerical Modelling*(1):59, 2005.

8. M. Dubov, V. Mezentsev, J. Petrovic, and I. Bennion. Femtosecond inscription in silica glass *(Invited). International Conference on High Power Laser Beams, Russia*, 2006.

9. V. Mezentsev, J. Petrovic, J. Dreher, and R. Grauer. Adaptive modelling of femtosecond laser microfabrication in dielectrics. *XII Conference on Laser Optics (SPIE)*, 2006.

10. J. S. Petrovic, V. Mezentsev, M. Dubov, and I. Bennion. Plasma Assisted Inscription of Photonics Components in Dielectrics *(Progress Report). 23rd Summer School and International Symposium on the Physics of Ionized Gases, Serbia*, to be published in American Insitute of Physics Conference Proceedings, 2006.

11. V. Mezentsev, M. Dubov, J. S. Petrovic and I. Bennion. Femtosecond Microfabrication of Subwavelength Photonic Devices. *ECOC*, 774 We3.P.195 accepted poster, 2006.

12. A. N. Grigorenko, A. K. Geim, H. F. Gleeson, Y. Zhang, A. A. Firsov, I. Y. Khrushchev, and J. Petrovic. Nanofabricated media with negative permeability at visible frequencies. *Nature*, 438 (7066):335, 2005.